LOW-ENERGY ELECTRON IRRADIATION OF 2D GRAPHENE AND

STABILITY INVESTIGATIONS OF 2D MoS$_2$

John Dideoluwa Femi Oyetoro

Dissertation Prepared for the Degree of

DOCTOR OF PHILOSOPHY

UNIVERSITY OF NORTH TEXAS

August 2021

APPROVED:

Jose Perez, Major Professor
Guido Verbeck, Committee Member
Duncan Weathers, Committee Member
Usha Philipose, Committee Member
Yuankun Lin, Committee Member
Jingbiao Cui, Chair of the Department of
    Physics
Pamela Padilla, Dean of the College of
    Science
Victor Prybutok, Dean of the Toulouse
    Graduate School

Femi Oyetoro, John Dideoluwa. *Low-Energy Electron Irradiation of 2D Graphene and Stability Investigations of 2D MoS₂*. Doctor of Philosophy (Physics), August 2021, 158 pp., 66 figures, chapter references.

In this work, we demonstrate the mechanism for etching exfoliated graphene on SiO_2 and other technological important substrates (Si, SiC and ITO), using low-energy electron sources. Our mechanism is based on helium ion sputtering and vacancy formation. Helium ions instead of incident electrons cause the defects that oxygen reacts with and etches graphene. We found that etching does not occur on low-resistivity Si and ITO. Etching occurs on higher resistivity Si and SiC, although much less than on SiO_2. In addition, we studied the degradation mechanism of MoS_2 under ambient conditions using as-grown and preheated mono- and thicker-layered MoS_2 films. Thicker-layered MoS_2 do not exhibit the growth of dendrites that is characteristic of monolayer degradation. Dendrites are observed to stop at the monolayer-bilayer boundary. Raman and photoluminescence spectra of the aged bilayer and thicker-layered films are comparable to those of as-grown films. We found that greater stability of bilayers and thicker layers supports a previously reported mechanism for monolayer degradation involving Förster resonance energy transfer. As a result, straightforward and scalable 2D materials integration, or air stable heterostructure device fabrication may be easily achieved. Our proposed mechanisms for etching graphene and ambient degradation of MoS_2 could catalyze research on realizing new devices that are more efficient, stable, and reliable for practical applications.

ACKNOWLEDGEMENTS

TABLE OF CONTENTS

LIST OF FIGURES

xiv

CHAPTER 1

INTRODUCTION

1.1. Two-Dimensional Materials

Materials are considered two-dimensional (2D) if the atoms are arranged in a plane of sheets. The thickness of the sheet must be in orders of magnitude smaller than its length. They can be easily stacked on one another. Atomically thin 2D materials are layered crystals with anisotropic bonding. They are strong in-plane or covalent bonding and weak out of-plane or van der Waals bonding. Graphene and transition metal dichalcogenides (TMDs) are both classified as 2D materials, that exhibit the above-mentioned properties. Monolayer graphene from graphite is 0.33 nm thin, hexagonal boron nitride (h-BN) is 0.33 nm thin and MoS_2 from molybdenite is 0.7 nm thin. In addition to thinness, 2D materials have a lot of unique properties such as the ability to form heterostructures from stacking, substrate independence, quantum confinement, etc. [1]. These are intrinsic properties, as opposed to scaling down three-dimensional (3D) bulk materials, to investigate these properties. The practical applications of 2D materials includes but not limited to, transistors, solar cells, light-emitting diodes, and photodetectors [2-8]. There are over 1500 2D materials that have been discovered [9]. Out of these, graphene was the first most studied. Novoselov and Geim extensively studied the electronic properties of graphene when they tried to isolate one atom thick layer from bulk graphite [10-13]. The discovery of monolayer graphene and TMDs in 2004 [14] ushered in the field of 2D Van der Waal Materials (VdWMs), which hold considerable promise for advancing technology by providing new properties that are not present in 3D materials. The carrier mobility and transport along the thin-body channel of 3D bulk semiconductors degrades substantially for thicknesses below 3 nm. Hence, a new channel material that is thin and yet maintains good carrier transport is highly required. With the end of Moore's law expected soon, there has been considerable interest in finding new technologies that can maintain or exceed its rate of progress. Due to the absence of band gap in graphene, of particular interest have been 2D TMDs that have the general formula

1

MX_2, where M is a transition metal such as Mo or W and X is chalcogen such as S or Te. These materials have found applications in electronic devices due to high carrier mobilities and reasonable band gaps, creating the possibility of large switching ratios in field effect transistors (FETs) [15, 16]. They are intended to replace or complement silicon technology by integration [17]. 2D materials have been often challenged with growth, integration, stability, etc. For example, interface is a common challenge in the case of metals contacts in FET devices where there is no out-of-plane bonding. Substrate-dependent phonon scattering has also been observed, which impedes carrier mobilities. Nucleation of ultrathin dielectrics on the surfaces has also posed difficulties due to absence of reactive sites [1]. The focus of this dissertation are the integration and stability problems, discussed in the following sections.

1.2. Etching Graphene Using Low-Energy Electron Irradiation

Integrating graphene is a major challenge in device fabrication. A variety of techniques have been investigated for the lithography of graphene and other 2D materials, with the most common being reactive ion plasma etching performed with a lithographic mask and resist. These resists often leave residues on the substrates which can affect its electronic properties such as doping. To circumvent this effect, researchers have investigated a direct-write method using a scanning electron microscopy (SEM) system with a gas injected into the chamber [18]. The gas is dissociated by the e-beam into a variety of reactive ions that etch the material. This method is advantageous because it is relatively inexpensive, and most research laboratories have an SEM system available typically with patterning capabilities. However, this alternative method of patterning graphene is only able to produce linewidths of about 20 nm, which is too large to produce useful bandgaps in future electronic applications such as graphene nanoribbons. Therefore, a study of the etching mechanism and/or decreasing the linewidth with an easily variable and diverse factor such as the substrate is of importance to implement graphene and other 2D materials as transistors and devices. Briefly, this etching technique has been used in the following instances. Using nitrogen gas and a low-energy focused electron beam (FEB) of < 10 keV, nanometer-size pores were etched onto graphene [19]. In this instance, the graphene was produced by sonicating

graphite in isopropanol. The solution with graphene flakes was dropped onto lacey carbon for subsequent TEM imaging. In effect, the graphene was suspended. It was hypothesized that the electron beam dissociated the N_2 gas adsorbed on and above the graphene surface which etched holes in the graphene. Those holes were about 50 nm in diameter whereas the electron beam was about 6 nm in diameter. In another work, sputtered thin carbon films were patterned with linewidths of about 20 nm using FEB with injected water vapor as the gas [20]. The delivery nozzle was placed 100 μm above the surface and the partial pressure was 2.4×10^{-5} Torr. It is interesting to note that in this study the substrate on which the carbon film was sputtered was not specified. Low-energy SEM based FEB using water vapor [21] and oxygen [22] as the gas has also been used to cut carbon nanotubes. An example that we believe involves limitations to the resolution of the etching due to sample charging is the following. In Ref. [18], Thiele et al. used FEB with oxygen as the gas was used to pattern graphene with a resolution better than 20 nm. The graphene consisted of mechanically exfoliated flakes on an SiO_2 substrate that was about 300 nm thick. The incident electron energy was 3 keV. The O_2 gas partial pressure was 2×10^{-3} Torr. At this energy, it was hypothesized that the O_2 molecules would be dissociated by the primary, backscattered, and secondary electrons, and produce reactive species such as excited oxygen molecules, ionized oxygen atoms and ozone. These reactive species would etch the graphene. In these studies, e-beam dosages of 1.5-29 C/cm^2 and a beam current of 0.1 nA were used, to give practical patterning speeds at acceptable e-beam scattering rates by the gas molecules. They concluded that secondary-electron intensities are responsible for etch profiles. We note that the dosages are relatively high and would produce a significant charge build up in the 300 nm thick SiO_2 substrate, and that would have a significant effect on the etching.

The ratio of secondary electrons to primary electrons for SiO_2 with an incident beam energy of 3 keV is above 1 [23], meaning that the SiO_2 substrate will overall charge positively as more electrons are being emitted than are being absorbed. The secondary electrons will produce a charged area on the order of the secondary beam diameter. This is so because they have a low energy and small escape depth. Therefore, the local area on the order of the

incident beam diameter will be positively charged to a few eV and attract negative oxygen ions that can etch graphene. The primary electrons will travel further into the substrate and disperse and backscatter because of collisions. As a result, deeper and more spread out regions of the substrate will charge negatively. Therefore, the positively ionized oxygen gas in the chamber due to the electron beam will be accelerated towards the dispersed negative areas meaning that the resolution of the etching will be negatively affected. We propose to optimize the precision of the etching by eliminating this charging effect by using thinner dielectrics. Materials with a thin dielectric layer on top of a conducting substrate allow the primary beam charge to mostly pass through the dielectric and pass to ground through the conducting substrate. This prevents the negative charge build-up of primary beam charge in the substrate and prevents positively charged oxygen ions from etching graphene further away from the beam.

In addition, Chen et al. [24] reported a technique in etching graphene using electrons from He plasma. They proposed a mechanism for low-energy electron irradiation induced etching of exfoliated multilayer graphene flakes on SiO_2/Si substrates. In their mechanism, electrons travel through the sample and reach the graphene/SiO_2 interface where they dissociate oxygen atoms from the SiO_2. The oxygen atoms etch the graphene from below by reaction with carbon bonds that have been rearranged or damaged by the incident electrons. The authors observed etching at incident electron energies of 50-200 eV and irradiation density of $14400\,mC/cm^2$ using a divergent electron cyclotron resonance (DECR) plasma system. They noted that incident electrons at these energies cannot reach the substrate since the electron mean free path is about 0.5-1.0 nm. Consequently, they considered that secondary electrons produced by the incident electrons are the ones that reach the substrate and cause oxygen dissociation. They stated that the whole process could be more complicated. Clearly, it can be seen that a well-defined and detailed mechanism is yet to be achieved on the electron irradiation etching of graphene exfoliated on SiO_2 at energies < 80 keV. Presently, a detailed mechanism has not been reached. Therefore, a clear mechanism is necessary for the effect and etching of graphene and other 2D materials using low-energy electron irra-

diation. We present mechanisms associated with irradiating graphene using electrons from helium plasma and SEM. We believe that our results will usher in a better understanding in integrating graphene into devices. Finally, we note that this dissertation is focused on the mechanisms involved in etching graphene than solving the linewidth issues [25, 26], which is proposed in the future work section of this dissertation.

1.3. Degradation and Stability of Transition Metal Dichalcogenides

TMDs in ambient air, with a focus on bilayers (BLs), twisted bilayers (TBLs), few-layers (FLs) and heterostructures have been extensively studied. They have many unique properties such as large spin orbit coupling and band gaps ranging from the infrared to the visible spectrum [27-30]. These properties give TMDs applications in optoelectronics, spintronics, valleytronics, flexible electronics, and sensors [31]. Knowledge of the air stability of these materials is crucial for simplifying device fabrication, streamlining packaging processes and extending device lifetimes. We have recently found that chemical vapor deposition (CVD)-grown BL and FL MoS_2 films are structurally and optically stable under ambient air conditions at about 40% relative humidity (RH) for periods of at least two years. This stability is remarkable given that monolayer (ML) MoS_2 and other ML TMDs are known to significantly degrade within a period of less than a year under the same ambient conditions [32-36]. ML TMDs' propensity for degradation limits their widespread implementation. The fundamental mechanism for the ambient stability of BL and FL MoS_2 films is not yet well understood. Furthermore, the ambient stability of other TMD materials has not been widely reported. Our main objectives in this dissertation is to determine and understand the ambient-air stability of: (1) BLs, TBLs and FLs of MoS_2 (2) BL and FL heterostructures. The TMD films were synthesized using CVD. These CVD-grown films are scalable with large domains and can be easily synthesized and transferred. We studied their structural, optical, and electronic properties with respect to various environmental conditions such as ambient air, humid air, and elevated temperature. Experimental techniques utilized includes atomic force microscopy (AFM), Raman spectroscopy, photoluminescence (PL) spectroscopy and, x-ray photoemission spectroscopy (XPS).

This investigation provides new information about the ambient stability of TMDs that will encourage further study into their fundamental properties and guide the development of devices with optimum ambient-air stability. Currently, the most common method for stabilizing reactive 2D materials is encapsulation in polymers [37] or between layers of an inert, insulating 2D material such as h-BN [38]. However, polymer encapsulation can adversely affect device properties [39] and h-BN encapsulation is not practical for large-scale fabrication processes. Thus, it is of great interest to investigate ambient-air stability and develop alternative degradation prevention methods. MoS_2 has been extensively used in micro- and nano-particulate form as a catalyst and lubricant. It is well known that such MoS_2 particles degrade under ambient conditions [40-42]. The proposed mechanism for their degradation involves oxidation at defect sites such as at the edges of the particles [43]. The oxides are then dissolved by water molecules in the air or adsorbed on the surface. Once the oxides are dissolved, the defects are susceptible to re-oxidation resulting in a continuous degradation process [43]. The structural and PL properties of CVD-grown ML TMDs have been studied under ambient air conditions at about 40% RH. After approximately one year, ML MoS_2 and WS_2 films were found to degrade along grain boundaries and edges [32]. Extensive cracking and decrease in PL intensity were reported. We have previously attributed the dendrite formation to oxide formation, which advances degradation [35]. The fractal dimension of the dendrite formation is consistent with a diffusion limited aggregation process [35]. In Ref. [32], it was observed that no degradation occurred when the samples were stored in a dry box. It appears that a humid environment is necessary for degradation to occur. These observations are consistent with the degradation mechanism proposed for MoS_2 particles in which adsorbed water molecules dissolve the oxides. However, in ML TMDs, it was found that degradation also required exposure to light at photon energies greater than the trion exciton binding energy [33]. Thus, a Förster resonance energy transfer (FRET) and/or photocatalysis mechanism was proposed [33]. Since both direct and indirect band gap semiconductors are known to exhibit photoinduced oxidation, it was proposed in Ref. [33] that BL and FL TMDs should also exhibit photoinduced degradation. We found, how-

6

ever, that BL and FL MoS$_2$ samples are extraordinarily stable. Under ambient air and room light conditions for periods of at least two years, virtually no degradation was observed. This dissertation provide results that may lead to new insights into ML degradation, including improved methods for slowing or stopping ML degradation, and stability of BL and FL TMDs [35, 44]. Finally, we propose TMD encapsulation for stable heterostructure devices.

1.4. Impact and Outline

The discoveries in this dissertation are the well-defined etching mechanism of graphene using low-energy electron irradiation, and the degradation and stability mechanisms of MoS$_2$. Firstly, we demonstrate that a direct-write using SEM doesn't etch graphene on SiO$_2$ substrate. Therefore, a specialized setup is required to take advantage of electron sources in an SEM. In addition, we discovered that etching graphene in Helium (He) plasma can be modulated based on the conductivity of the substrates. Conducting substrates provide non-isolating surface, making electrons from He plasma to pass through the graphene, without inducing etching. In contrast, dielectric or insulating substrates, tend to have charges from electrons building up on graphene surface. This provides an electric filed, that attracts the He ions. He ions then etches graphene on the surface though ion bombardment [24-26]. Secondly, we propose the degradation mechanism of MoS$_2$ as a diffusion limited aggregated process for the ML MoS$_2$. The stability process for BL and FLs MoS$_2$ was determined to be a FRET or photocatalysis mechanism. This dissertation is segmented in such a way that each chapter highlights a discussion on the research outcomes for each completed project:

- Chapter 1 provides explanation on the research problems that were explored.
- Chapter 2 provides background on two-dimensional materials (graphene and MoS$_2$), especially the electronic band structure and potential applications.
- Chapter 3 discusses the experimental techniques used for carrying out the research projects, and the tools utilized for measurements.
- Chapter 4 explores the low-energy irradiation of graphene on SiO$_2$ from a focused electron-beam, and to determine if a direct-write technique is feasible.

- Chapter 5 expands on a previous mechanism, by investigating the etching of graphene on different substrates, using low-energy electron irradiation from helium plasma electron sources.

- Chapter 6 investigates the mechanism of rapid ambient degradation of monolayer MoS$_2$ after heating in air.

- Chapter 7 investigates the mechanism of long-term stability of bilayer MoS$_2$ in ambient air.

- Chapter 8 discusses the dissertation summary and future work.

1.5. References

[1] Franklin, A. D. 2015. Nanomaterials in transistors: From high-performance to thin-film applications. Science, 349(6249), aab2750

[2] Chhowalla, M., Jena, D., Zhang, H. 2016. Two-dimensional semiconductors for transistors. Nature Reviews Materials, 1(11), 16052.

[3] Sangwan, V.K. and Hersam, M.C., 2018. Electronic transport in two-dimensional materials. Annual review of physical chemistry, 69, pp.299-325.

[4] Yoon Y, Ganapathi K, Salahuddin S. 2011. How good can monolayer MoS$_2$ transistors be? Nano Lett. 11:3768–73

[5] Jariwala D, Sangwan VK, Lauhon LJ, Marks TJ, Hersam MC. 2014. Emerging device applications for semiconducting two-dimensional transition metal dichalcogenides. ACS Nano 8:1102–20

[6] Fiori G, Bonaccorso F, Iannaccone G, Palacios T, Neumaier D, et al. 2014. Electronics based on twodimensional materials. Nat. Nanotechnol. 9:768–79

[7] Das S, Robinson JA, Dubey M, Terrones H, Terrones M. 2015. Beyond graphene: progress in novel two-dimensional materials and van der Waals solids. Annu. Rev. Mater. Res. 45:1–27

[8] Alam K, Lake RK. 2012. Monolayer MoS$_2$ transistors beyond the technology road map. IEEE Trans.59:3250–54

[9] Cheon, G., Duerloo, K.A.N., Sendek, A.D., Porter, C., Chen, Y. and Reed, E.J.,

2017. Data mining for new two-and one-dimensional weakly bonded solids and lattice-commensurate heterostructures. Nano letters, 17(3), pp.1915-1923.

[10] Neto, A.C., Guinea, F., Peres, N.M., Novoselov, K.S. and Geim, A.K., 2009. The electronic properties of graphene. Reviews of modern physics, 81(1), p.109.

[11] Novoselov, K. S., Mishchenko, A., Carvalho, A., Neto, A. C. (2016). 2D materials and van der Waals heterostructures. Science, 353(6298), aac9439.

[12] Novoselov, K. S., Jiang, D., Schedin, F., Booth, T. J., Khotkevich, V. V., Morozov, S. V., Geim, A. K. (2005). Two-dimensional atomic crystals. Proceedings of the National Academy of Sciences, 102(30), $10451MoS_2$ 0453.

[13] Geim, A. K. (2009). Graphene: status and prospects. Science, 324(5934), $1530MoS_2$ 534.

[14] Novoselov, K.S., Geim, A.K., Morozov, S.V., Jiang, D., Zhang, Y., Dubonos, S.V., Grigorieva, I.V. and Firsov, A.A., 2004. Electric field effect in atomically thin carbon films. science, 306(5696), 666-669.

[15] Bhimanapati GR, Lin Z, Meunier V, Jung Y, Cha J, et al. 2015. Recent advances in two-dimensional materials beyond graphene. ACS Nano 9:11509–39.

[16] Fiori G, Bonaccorso F, Iannaccone G, Palacios T, Neumaier D, et al. 2014. Electronics based on two-dimensional materials. Nat. Nanotechnol. 9:768–79

[17] Akinwande, D., Huyghebaert, C., Wang, C.H., Serna, M.I., Goossens, S., Li, L.J., Wong, H.S.P. and Koppens, F.H., 2019. Graphene and two-dimensional materials for silicon technology. Nature, 573(7775), pp.507-518.

[18] Thiele, C., Felten, A., Echtermeyer, T.J., Ferrari, A.C., Casiraghi, C., Löhneysen, H.V. and Krupke, R., 2013. Electron-beam-induced direct etching of graphene. Carbon, 64, pp.84-91.

[19] Fox, D., O'Neill, A., Zhou, D., Boese, M., Coleman, J.N. and Zhang, H.Z., 2011. Nitrogen assisted etching of graphene layers in a scanning electron microscope. Applied Physics Letters, 98(24), p.243117.

[20] Spinney, P.S., Howitt, D.G., Smith, R.L. and Collins, S.D., 2010. Nanopore for-

mation by low-energy focused electron beam machining. Nanotechnology, 21(37), p.375301.

[21] Yuzvinsky, T.D., Fennimore, A.M., Mickelson, W., Esquivias, C. and Zettl, A., 2005. Precision cutting of nanotubes with a low-energy electron beam. Applied Physics Letters, 86(5), p.053109.

[22] Liu, P., Arai, F. and Fukuda, T., 2006. Cutting of carbon nanotubes assisted with oxygen gas inside a scanning electron microscope. Applied physics letters, 89(11), p.113104.

[23] Yi, W., Jeong, T., Yu, S., Lee, J., Jin, S., Heo, J. and Kim, J.M., 2001. Study of the secondary-electron emission from thermally grown SiO_2 films on Si. Thin Solid Films, 397(1-2), pp.170-175.

[24] Chen, C., Wang, C. and Diao, D., 2016. Low energy electron irradiation induced carbon etching: Triggering carbon film reacting with oxygen from SiO_2 substrate. Applied Physics Letters, 109(5), p.053104.

[25] Femi-Oyetoro, J.D., Yao, K., Roccapriore, K., Ecton, P.A., Tang, R., Jones, J.D., Verbeck, G. and Perez, J.M., 2019. Effects of high-dosage focused electron-beam irradiation at energies 30 keV on graphene on SiO_2. Applied Surface Science, 469, pp.325-330.

[26] Femi-Oyetoro, J.D., Yao, K., Tang, R., Ecton, P., Roccapriore, K., Mhlanga, A., Verbeck, G., Weathers, D.L. and Perez, J.M., 2019. Mechanism for etching of exfoliated graphene on substrates by low-energy electron irradiation from helium plasma electron sources. Journal of Vacuum Science Technology A: Vacuum, Surfaces, and Films, 37(2), p.021401.

[27] Radisavljevic, B., Radenovic, A., Brivio, J., Giacometti, V. and Kis, A., 2011. Single-layer MoS_2 transistors. Nature Nanotechnology, 6(3), pp.147-150.

[28] Splendiani, A., Sun, L., Zhang, Y., Li, T., Kim, J., Chim, C.Y., Galli, G. and Wang, F., 2010. Emerging photoluminescence in monolayer MoS_2. Nano Letters, 10(4), pp.1271-1275.

[29] Mak, K.F., Lee, C., Hone, J., Shan, J. and Heinz, T.F., 2010. Atomically thin MoS_2: a new direct-gap semiconductor. Physical Review Letters, 105(13), p.136805.

[30] Manzeli, S., Ovchinnikov, D., Pasquier, D., Yazyev, O.V. and Kis, A., 2017. 2D transition metal dichalcogenides. Nature Reviews Materials, 2(8), p.17033.

[31] Wang, Q. H.; Kalantar-Zadeh, K.; Kis, A.; Coleman, J. N.; Strano, M. S. Electronics and Optoelectronics of Two-Dimensional Transition Metal Dichalcogenides. Nature Nanotechnology. 2012, pp 699–712. https://doi.org/10.1038/nnano.2012.193.

[32] Gao, J.; Li, B.; Tan, J.; Chow, P.; Lu, T.-M.; Koratkar, N. Aging of Transition Metal Dichalcogenide Monolayers. ACS Nano. 2016, pp 2628–2635.https://doi.org/10.1021/acsnano.5b07

[33] Kotsakidis, J. C.; Zhang, Q.; de Parga, A. L. V.; Currie, M.; Helmerson, K.; Kurt Gaskill, D.; Fuhrer, M. S. Oxidation of Monolayer WS2 in Ambient Is a Photoinduced Process. Nano Letters. 2019, pp 5205–5215. https://doi.org/10.1021/acs.nanolett.9b01599.

[34] Budania, P.; Baine, P.; Montgomery, J.; McGeough, C.; Cafolla, T.; Modreanu, M.; McNeill, D.; Mitchell, N.; Hughes, G.; Hurley, P. Long-Term Stability of Mechanically Exfoliated MoS_2 Flakes. MRS Communications. 2017, pp 813–818. https://doi.org/10.1557/mrc.2017.105.

[35] Yao, K.; Femi-Oyetoro, J. D.; Yao, S.; Jiang, Y.; El Bouanani, L.; Jones, D. C.; Ecton, P. A.; Philipose, U.; El Bouanani, M.; Rout, B.; Neogi, A.; Perez, J. M. Rapid Ambient Degradation of Monolayer MoS_2 after Heating in Air. 2D Materials. 2019, p 015024. https://doi.org/10.1088/2053-1583/ab5971.

[36] Şar, H.; Özden, A.; Demiroğlu, İ.; Sevik, C.; Perkgoz, N. K.; Ay, F. Long-Term Stability Control of CVD-Grown Monolayer MoS_2. Physica Status Solidi (RRL) – Rapid Research Letters. 2019, p 1800687. https://doi.org/10.1002/pssr.201800687.

[37] Chamlagain, B.; Li, Q.; Ghimire, N. J.; Chuang, H.-J.; Perera, M. M.; Tu, H.; Xu, Y.; Pan, M.; Xaio, D.; Yan, J.; Mandrus, D.; Zhou, Z. Mobility Improvement and Temperature Dependence in MoSe2 Field-Effect Transistors on Parylene-C Substrate. ACS Nano. 2014, pp 5079–5088. https://doi.org/10.1021/nn501150r.

[38] Birowska, M.; Urban, J.; Baranowski, M.; Maude, D. K.; Plochocka, P.; Szwacki,

N. G. The Impact of Hexagonal Boron Nitride Encapsulation on the Structural and Vibrational Properties of Few Layer Black Phosphorus. Nanotechnology. 2019, p 195201. https://doi.org/10.1088/1361-6528/ab0332.

[39] Liang, J., Xu, K., Toncini, B., Bersch, B., Jariwala, B., Lin, Y.C., Robinson, J. and Fullerton-Shirey, S.K., 2019. Impact of Post-Lithography Polymer Residue on the Electrical Characteristics of MoS_2 and WSe2 Field Effect Transistors. Advanced Materials Interfaces, 6(3), p.1801321.

[40] Fleischauer, P. D.; Lince, J. R. A Comparison of Oxidation and Oxygen Substitution in MoS_2 Solid Film Lubricants. Tribol. Int. 1999, 32, 627– 636, DOI: 10.1016/s0301-679x(99)00088-2.

[41] Curry, J. F.; Luftman, H. S.; Sidebottom, M. A.; Strandwitz, N. C.; Argibay, N.; Krick, B. A. Probing the First Few Layers of MoS_2 with HS-LEIS: Effect of Microstructure on Oxidation. Tribol. Lubr. Technol. 2017, 73, 42– 48.

[42] Topsøe, H. The Role of Co–Mo–S Type Structures in Hydrotreating Catalysts. Appl. Catal., A 2007, 322, 3– 8, DOI: 10.1016/j.apcata.2007.01.002.

[43] Afanasiev, P.; Lorentz, C. Oxidation of Nanodispersed MoS_2 in Ambient Air: The Products and the Mechanistic Steps. The Journal of Physical Chemistry C. 2019, pp 7486–7494. https://doi.org/10.1021/acs.jpcc.9b01682.

[44] Femi-Oyetoro, J., Yao, K., Hathaway, E., Jiang, Y., Ojo, I., Squires, B., Neogi, A., Cui, J., Philipose, U., Gadiyaram, N.K., Zhou, W., and Perez, J., 2020. Long-term Stability of Bilayer MoS_2 in Ambient Air. arXiv preprint arXiv:2010.06770.

CHAPTER 2

GRAPHENE AND MoS$_2$

2.1. Graphene

Graphene, an allotrope of carbon, is a quasi-two-dimensional (2D) crystal derived from graphite and arranged in a hexagonal lattice. It is a single atomic layer with a separation of 3.35 Å. Graphite is made of graphene planes, and each plane is stacked to the other through van der Waals interaction. This interaction is weak, making graphene to be easily isolated from bulk graphite [1, 2]. Ample physical and electronic properties have been attributed to graphene, revealed through interesting and rigorous research. The zero-band gap of graphene has made it possible for fabricating high electron mobility transistors [3-5]. Therefore, integrating graphene into electronic devices is of particular interest.

2.1.1. Graphene Lattice

Crystals can be constructed in real space, in form of a lattice called the real or direct lattice. Consequently, this same lattice can be illustrated in k-space known as the reciprocal lattice. The carbon atoms in graphene are arranged in a hexagonal (honeycomb) lattice. If we categorize the atoms into two different types: type A (orange) and type B (green) as shown in Figure 2.1 (a). The type A atoms are surrounded with three type B atoms and vice versa. This forms a complex lattice all together. The atoms A and B form two sub lattices. If we denote $\vec{\delta_1}$, $\vec{\delta_2}$ and $\vec{\delta_3}$ as the lengths of the vectors for the nearest neighbor distance a, then $\vec{a_1}$ and $\vec{a_2}$ are the lattice vectors as illustrated in Figure 2.1 (a). Therefore, we can write:

(2.1) $\vec{\delta_1} = \frac{a}{2}(1, \sqrt{3}); \vec{\delta_2} = \frac{a}{2}(1, -\sqrt{3}); \vec{\delta_3} = \frac{a}{2}(-1, 0); \vec{a_1} = \frac{a}{2}(3, \sqrt{3}); \vec{a_2} = \frac{a}{2}(3, -\sqrt{3})$

The lattice vectors are the basis of the graphene's primitive unit cell which is a parallelogram. The lengths of these vectors, a, are called the lattice constant of graphene. Taking into consideration just one of the two types of atom, a hexagon with one atom at the center can formed. This is the Bravais lattice as shown in Figure 2.1 (a). The corresponding
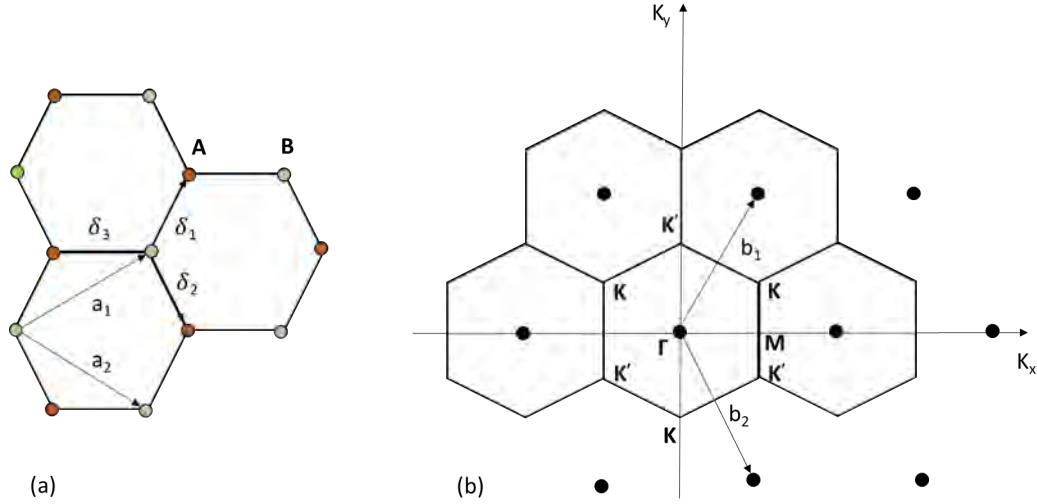
FIGURE 2.1. (a) Shows the honey-comb lattice of graphene in real space. (b) Shows the corresponding reciprocal lattice with Γ, K′, K and M high-symmetry points in the Brillouin zone after Fourier transform.

reciprocal lattice can be achieved by rotating the direct lattice by 90° with Γ, K′, K and M high-symmetry points in the Brillouin zone as shown in Figure 2.1 (b). This is the state or momentum space [6]. Since graphene is an allotrope of carbon, this means each carbon atom has 6 electrons. It is well known that electrons usually prefer to fill up states with lower energies first. The first electron shell is fully occupied with two electrons, but the second shell has 4 empty spaces.

This shell can be further divided into 2 subshells, $2s$ and $2p$ containing p_x, p_y and p_z. Subshell $2p$ is of slightly higher energy than $2s$. In this configuration, there are two possible chemical bonds namely, σ-covalent bond and π-covalent bond. In σ-bond, there is a co-axial overlapping of atomic orbitals of the two atoms. In π-bond, the two electron clouds are in parallel and are superimposed with each other in a head-on manner. Therefore, σ-bond is heavily overlapped as compared to π-bond, which is only slightly overlapped. σ-bond is known to be more stable and not easily reactive while π-bond is less stable and more reactive. Hence, the most interesting properties of graphene comes from the π-electrons. These are quasi-free and attributed to graphene's electrical conductivity.

2.1.2. Electronic Structure of Monolayer Graphene

In tight binding theory, electrons are assumed to be tightly bound to the atoms. Here, it is assumed that the electrons are only hoping between the two neighboring atoms. This assumption can be used to obtain the wave function and band structure of graphene. We denote t has the hopping parameter, which has a dimension of energy. Wallace [7] was the first to obtain electronic structure of graphene and graphite using tight-binding model. This would be later developed by McClure [8] and Slonczeewski and Wiess [9]. Considering the π-states, and the nearest neighbour hopping integral as $t \approx 2.7$ eV with the next nearest neighbour $t' \ll t$. The tight-binding Hamiltonian for electrons in graphene considering that electrons can hop to both nearest- and next-nearest-neighbor atoms has the form 2×2 matrix, given by [10, 11]:

$$\hat{H}(\vec{k}) = \begin{pmatrix} H_{11} & H_{12} \\ H_{12}^* & H_{11} \end{pmatrix} = \begin{pmatrix} 0 & tS(\vec{k}) \\ tS^*(\vec{k}) & 0 \end{pmatrix}$$

(2.2)

$\vec{k}$ is the wavevector.

(2.3)
$$S(\vec{k}) = \sum_{\vec{\delta}} e^{i\vec{k}\vec{\delta}} = 2exp(\frac{ik_x a}{2}) \cos(\frac{k_y a \sqrt{3}}{2}) + exp(-ik_x a)$$

From the eigenvalues of the Hamiltonian matrix, the resulting energy-momentum dispersion relation can be written as:

(2.4)
$$E(\vec{k}) = \pm t|S(\vec{k})| = \pm t\sqrt{3 + f(\vec{k})}$$

Where

(2.5)
$$f(\vec{k}) = 2\cos(\sqrt{3}k_y a) + 4\cos(\frac{\sqrt{3}}{2}k_y a)\cos(\frac{3}{2}k_x a)$$

15

Since $S(\vec{K}) = S(\vec{K}')$, the two bands shown on the band structure of graphene of Figure 2.2 (a) will cross at these points. Therefore, by changing the phases of the basis wavefunctions and expanding the Hamiltonian, we have:

$$\hat{H}_k(\vec{q}) \approx \frac{3at}{2} \begin{pmatrix} 0 & q_x - iq_y \\ q_x + iq_y & 0 \end{pmatrix}$$

(2.6)

(2.7)
$$\hat{H}_k(\vec{q}) = \hbar v_F \vec{q} \cdot \vec{\sigma}$$

Where σ is the vector of Pauli-matrices and v is the electron velocity at point on the cones, which replaces the speed of light. This a 2D massless Dirac Hamiltonian, which describes free relativistic electrons, where the speed of light has been replaced by:

(2.8)
$$v = \frac{3at}{2\hbar}$$

Putting into consideration the next nearest neighbour t', we can write:

(2.9)
$$E(\vec{k}) = \pm t |S(\vec{k})| + t' f(\vec{k}) = \pm t \sqrt{3 + f(\vec{k})} + t' f(\vec{k})$$

$E(\vec{k})$ can be written in terms of the wave-vector components k_x and k_y as:

(2.10)
$$E(k_x, k_y) = \pm t \sqrt{1 + 4\cos^2(\frac{ak_x}{2}) + 4\cos(\frac{ak_x}{2})\cos(\frac{\sqrt{3}ak_y}{2})}$$

Or

(2.11)
$$E(k_x, k_y) = \pm t \sqrt{1 + 4\cos(\frac{ak_x}{2})(\cos(\frac{ak_x}{2}) + \cos(\frac{\sqrt{3}ak_y}{2}))}$$

(a) (b)
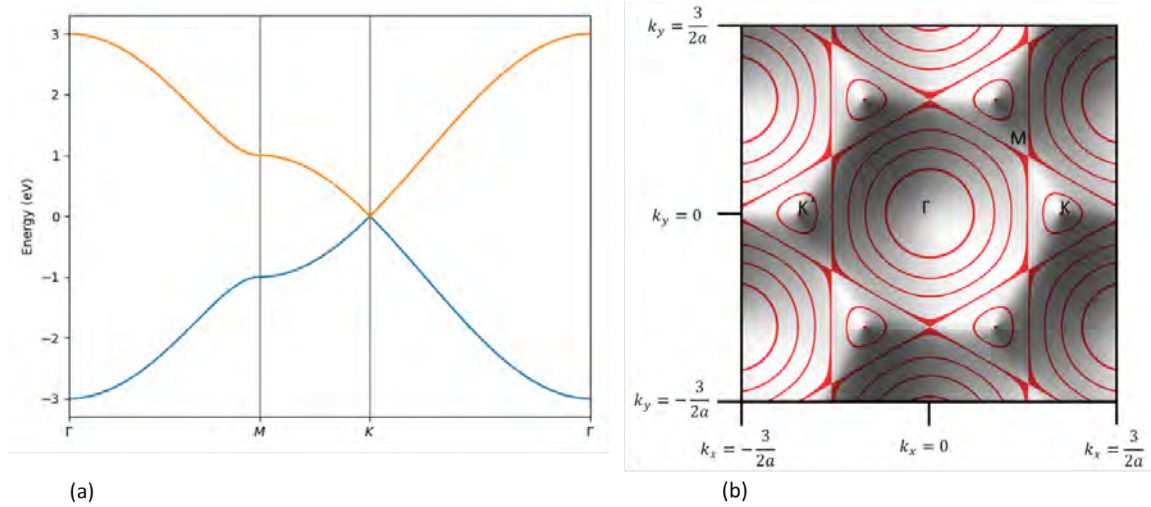
FIGURE 2.2. (a) Band structure of graphene with high-symmetry points, the blue curve indicates the valence band while the orange curve represents the conduction band. (b) Shows contour plot of the energy dispersion $E(k_x, k_y)$ of graphene.

Where $t \approx 2.8$ eV and $a \approx 2.46$ Å

The 3D energy dispersion can be easily obtained from the above-mentioned tight-binding approximation method as shown in Figure 2.3. The lower region is the valence (π) band and the upper region is the conduction (π*) band. The Fermi level is the point at which the conduction and the valence bands meet, which is known as the Dirac point. There are six Dirac cones, each of this cone has a linear E-k dispersion relationship. The six Dirac points are dependent. The K points lies where the valence and conduction band meet. M lies between two neighboring Dirac points, and Γ are the saddle points, also known as the van Hove singularity points.
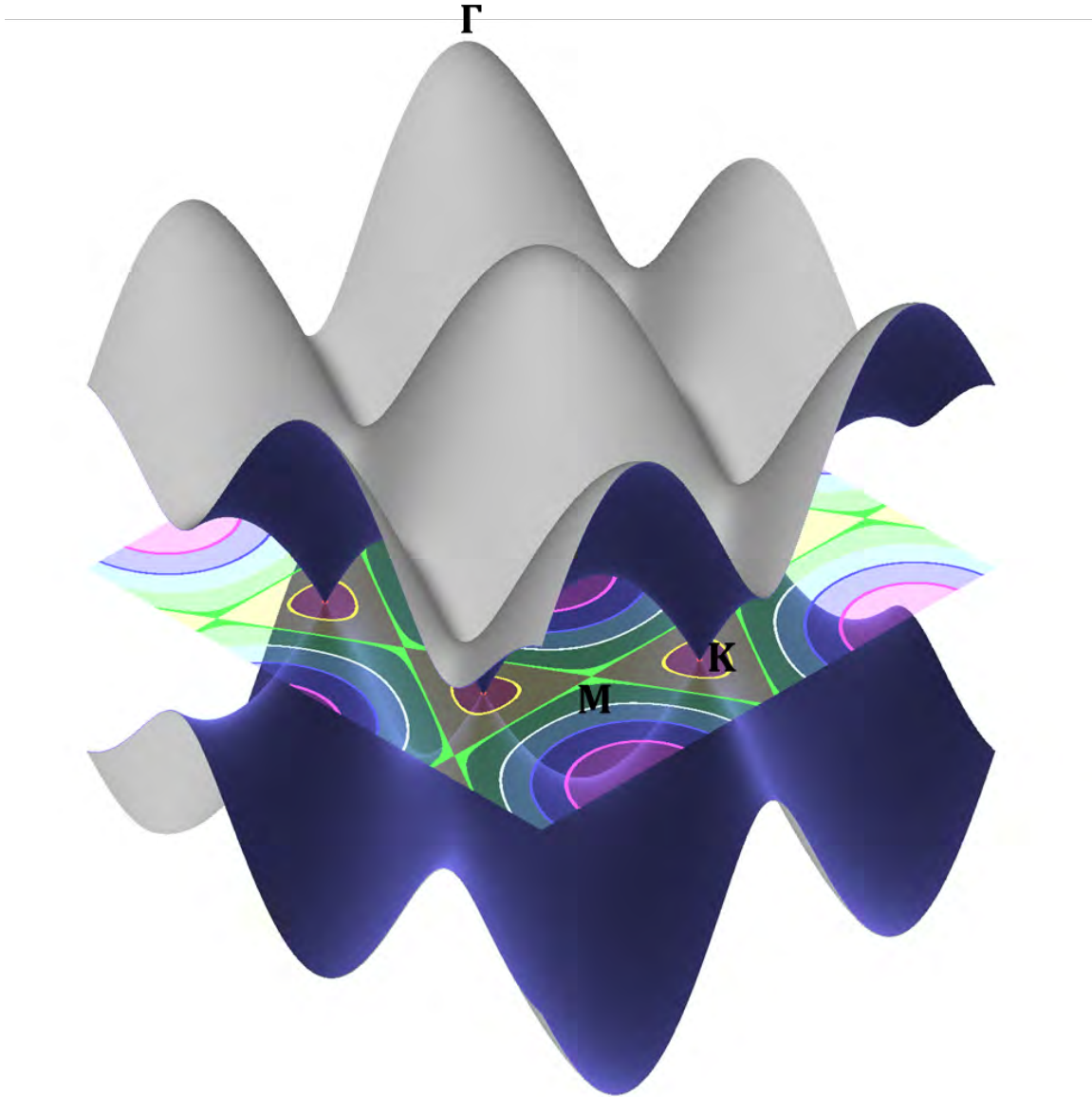
FIGURE 2.3. 3D graphene energy dispersion as a function of the wave-vector components k_x and k_y from π-bonding. There are two bands, one with positive energy, and the other with negative energy, touching at the zone corners.

2.2. Molybdenum Disulfide (MoS_2)

TMD monolayer consists of a transition metal layer that is sandwiched between two chalcogen layers, as shown schematically in Figures 2.4 (a) and (b). Although monolayer TMDs such as MoS_2 possess a large direct band gap, their low electrical mobilities limit their application in high-speed electronics [12]. However, TMDs may be useful in spintronic and
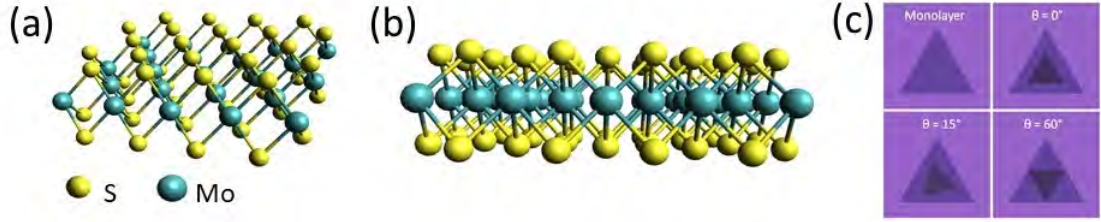
FIGURE 2.4. (a) Structure of monolayer MoS_2. (b) Side view of monolayer MoS_2. (c) Monolayer and bilayer MoS_2 at various twist angles.

valleytronic applications. Another potentially useful property of TMDs is the twist angle, θ, of bilayers, which is defined as the angle between the layers. Figure 2.4 (c) shows illustrations of TMD bilayers with twist angles of 0° (AA stacking), 15°, and 60° (AB stacking). Some interesting properties of twisted TMD bilayers are unconventional superconductivity at small twist angles [13], twist dependent valley and band alignment [14], and moiré pattern excitons [15].

2.2.1. Electronic Structure of Monolayer MoS_2

The lattice constant a for the in-plane unit cell is 3.09 Å, and the Mo-S bond length b is 2.39 Å. The in-plane Brillouin zone of MoS_2 is a hexagon with the following high-symmetry points [10, 16, 17]:

$$(2.12) \qquad \Gamma = (0,0); M = \frac{4\pi}{3a(0, \frac{\sqrt{3}}{2})}; K = \frac{4\pi}{3a(1,0)}$$

A monolayer MoS_2 has a direct band gap with direct $K \to K'$ and indirect $\Gamma \to Q$ gaps, about 1.79 eV and 2.03 eV respectively. In contrast to graphene, TMDs such as MoS_2 present an excellent orbital contribution for the valence and conduction bands. These bands are mainly constituted by the metal M five $4d$ orbitals and the six (each layer has three) $3p$ orbitals of the chalcogen X. These sum up to 93% of the bands total orbital weight. The first-principle calculations show that there is a local conduction band minimum at the Q point, which is midway between the Γ and K points, and a local valence band maximum at

the Γ point for monolayer MoS$_2$ as shown in Figures 2.5 (a) and (b). These become absolute extrema for multilayers MoS$_2$, where the conduction band is at Q and the valence band is at Γ. All these features need to be fully represented, in the entire Brillouin zone. Therefore, a robust tight-binding model is needed. Slater-Koster model with 11 bands, has been widely used [18]. These bands are made up of five d orbitals of the M metal atom and the six p orbitals of the two chalcogens X atoms in the unit cell. The base is written as:

(2.13) $$(p_x^t, p_y^t, p_z^t, d_{3z^2-r^2}, d_{xz}, d_{yz}, d_{x^2-y^2}, d_{xy}, p_x^b, p_y^b, p_z^b)$$

Where t and b represent the top and bottom planes of the chalcogen. The hopping integral between the orbitals is defined in terms of σ, π and δ ligands. The Hamiltonian in k-space can be expressed as:

(2.14) $$H = \begin{pmatrix} H_{MM} & H_{MX} \\ H_{MX^\dagger} & H_{XX} \end{pmatrix}$$

(2.15) $$H_{MM} = \epsilon_M + 2 \sum_{i=1,2,3} t_i^{MM} \cos(\boldsymbol{k} \cdot \boldsymbol{a_i})$$

(2.16) $$H_{XX} = \epsilon_X + 2 \sum_{i=1,2,3} t_i^{XX} \cos(\boldsymbol{k} \cdot \boldsymbol{a_i})$$

(2.17) $$H_{MX} = \sum_{i=1,2,3} t_i^{MX} e^{-i\boldsymbol{k} \cdot \boldsymbol{\delta_i}}$$

The nearest-neighbor hopping terms $t_{ij,\mu v}$ between M and X atoms and appropriate Slater-Koster parameters are fully described in Refs. [17, 18]

20
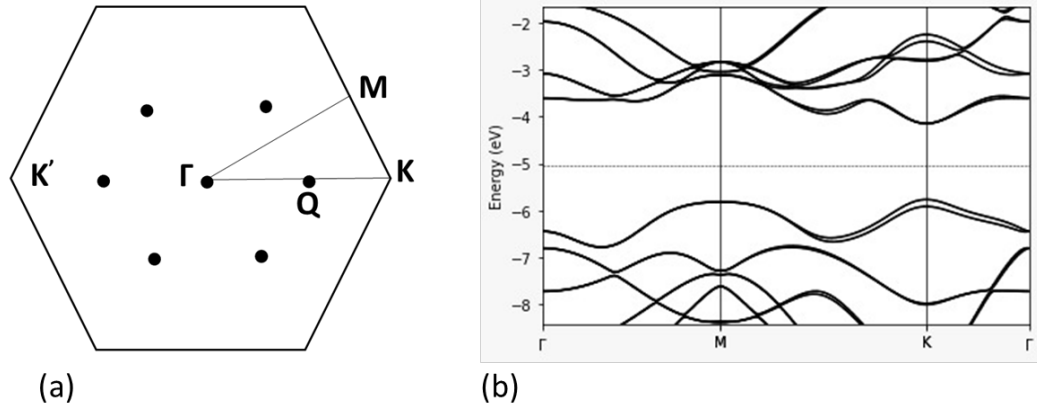
FIGURE 2.5. (a) Shows the Brillouin zone of MoS_2 with high-symmetry points. The Q points represents the conduction band edges in multilayers MoS_2 (b) Shows the corresponding band structure with high-symmetry locations.

2.2.2. Bilayers and Twisted Bilayers

BLs of graphene and TMD materials have recently attracted considerable interest due to the new properties they acquire as the twist angle between layers varies. The rotational misalignment between layers in BLs forms a moiré pattern that acts as an in-plane superlattice in addition to the atomic lattice. The moiré superlattice's length and electronic energy scales are controllable by the twist angle. For small twist angles of 1°, the interlayer coupling strengthens, and new phenomena arises. In TBL graphene, unconventional superconductivity has been reported at magic twist angles of about 1° [19]. In TBL TMDs, such moiré superlattices have been shown to confine interlayer excitons within their potential wells [20-23]. Interlayer excitons are bound electron-hole pairs in which the electron and holes are in different layers. Excitons in TMDs are optically active, follow Bose-Einstein statistics, and have long lifetimes [24]. These properties make ordered arrays of interlayer excitons confined by the superlattice a novel platform for studying nanophotonics, single light emitters, quantum information and quantum entanglement.

For interlayer excitons confined in $MoSe_2/WSe_2$ and WSe_2/WS_2 TBL heterostructures with twist angles of 0.5°, it has been experimentally found that the diffusion, position

21

and energy levels of the interlayer excitons can be tuned by varying the superlattice periodicity and/or applying an electric field [20-23]. In these experiments, the TBL heterostructures were formed from exfoliated flakes and encapsulated between layers of h-BN for isolation and protection. However, if the small-twist-angle heterostructures are stable under ambient conditions, it may be possible to simplify the encapsulation to only one h-BN layer or even omit the encapsulation entirely. The ambient stability of TBL TMDs has not been reported; therefore, it would be of interest to study their ambient stability as a function of twist angle. The ambient-air stability of TBLs with a wide range of twist angles was studied. For TBLs with small twist angles, we plan to measure the twist angle using scanning tunneling electron microscope (STEM), as a future research work. The TBLs will be deposited on TEM grids using existing transfer techniques. The most stable BL configurations are at twist angles of 0° and 60°, which are discussed in this dissertation. For small twist angles, the increased interlayer coupling produces atomic reconstructions in the layers [25]. This may increase the surface reactivity due to the formation of dangling bonds, resulting in a decrease in ambient-air stability. At larger twist angles, the interlayer coupling is weaker as compared to that at 0° and 60° [26]. A reduction in interlayer coupling may also decrease the stability since the layers may behave more like isolated MLs.

2.2.3. Heterostructures with Large Twist Angles

Heterostructures are extensively used in optoelectronics. They consist of two vertically stacked semiconductors with different band gaps. The band alignment at the interface between the two semiconductors determines the distribution of electrons and holes at the interface. TMD BL heterostructures are of considerable interest because they have a type II staggered band alignment, which makes them useful as photodetectors. In a Type II heterostructure, only one carrier type is transferred across the interface to the corresponding lower energy band of the other semiconductor; thus, photoexcited electron-hole pairs are efficiently separated. Due to the atomic-scale thinness of BLs, the time it takes to separate the carriers is ultrashort. In MoS_2/WS_2 BLs, the separation takes place under 100 fs [27,28]. In Ref. [27], the heterostructures were synthesized by transferring exfoliated flakes and thus

had random twist angles of 0°< θ <60°. In Ref. [28], the heterostructures were grown using CVD and thus had well-defined large twist angles such as 15° and 30°. In both cases, the charge transfer time remained constant independent of the twist angle. Understanding the effects of ambient exposure on the structural and electronic properties of TMD TBL heterostructures over a wide range of twist angles would motivate further research into the potential applications of these materials.

2.2.4. Few-layers

TMD FLs are more electrically conductive than MLs. They have band gaps that vary from 1-2 eV and depend on the number of layers. These properties make them more suitable than MLs in certain devices. For example, BL and FL FETs can carry higher on-state currents [29]. In addition, modulation of the number of layers along the lateral direction in FLs results in a laterally modulating band gap. This can be used to fabricate novel lateral heterostructures [30-32]. Also, FL-based devices have higher yields due to their mechanical strength [33, 34]. In general, TMD FLs have not received as much attention as MLs mainly because FLs have indirect band gaps while MLs have direct band gaps. Most studies on the ambient stability of TMD FLs have focused on exfoliated flakes submerged in water or placed in humid environments of $\geq 60\%$ RH [35-37]. Knowledge of their ambient air stability in standard humid conditions ($\approx 40\%$) is lacking but required for practical applications.

2.3. References

[1] Novoselov, K. S., Mishchenko, A., Carvalho, A., Neto, A. C. (2016). 2D materials and van der Waals heterostructures. Science, 353(6298), aac9439.

[2] Novoselov, K. S., Jiang, D., Schedin, F., Booth, T. J., Khotkevich, V. V., Morozov, S. V., Geim, A. K. (2005). Two-dimensional atomic crystals. Proceedings of the National Academy of Sciences, 102(30), 10451

[3] Franklin, A. D. (2015). Nanomaterials in transistors: From high-performance to thin-film applications. Science, 349(6249), aab2750.

[4] Geim, A. K. (2009). Graphene: status and prospects. Science, 324(5934), 1530MoS$_2$ 534.

[5] Chhowalla, M., Jena, D., Zhang, H. (2016). Two-dimensional semiconductors for transistors. Nature Reviews Materials, 1(11), 16052.

[6] EdX ChalmersX: ChM001x Graphene Science and Technology

[7] Wallace, P.R., 1947. The band theory of graphite. Physical review, 71(9), p.622.

[8] McClure, J.W., 1957. Band structure of graphite and de Haas-van Alphen effect. Physical Review, 108(3), p.612.

[9] Slonczewski, J.C. and Weiss, P.R., 1958. Band structure of graphite. Physical Review, 109(2), p.272.

[10] Avouris, P., Heinz, T.F. and Low, T. eds., 2017. 2D Materials. Cambridge University Press.

[11] Neto, A.C., Guinea, F., Peres, N.M., Novoselov, K.S. and Geim, A.K., 2009. The electronic properties of graphene. Reviews of modern physics, 81(1), p.109.

[12] Wang, H., Yu, L., Lee, Y.H., Shi, Y., Hsu, A., Chin, M.L., Li, L.J., Dubey, M., Kong, J. and Palacios, T., 2012. Integrated circuits based on bilayer MoS$_2$ transistors. Nano letters, 12(9), pp.4674-4680.

[13] Cao, Y., Fatemi, V., Fang, S., Watanabe, K., Taniguchi, T., Kaxiras, E. and Jarillo-Herrero, P., 2018. Unconventional superconductivity in magic-angle graphene superlattices. Nature, 556(7699), p.43.

[14] Yeh, P.C., Jin, W., Zaki, N., Kunstmann, J., Chenet, D., Arefe, G., Sadowski, J.T., Dadap, J.I., Sutter, P., Hone, J. and Osgood Jr, R.M., 2016. Direct measurement of the tunable electronic structure of bilayer MoS$_2$ by interlayer twist. Nano letters, 16(2), pp.953-959.

[15] Lin, M.L., Tan, Q.H., Wu, J.B., Chen, X.S., Wang, J.H., Pan, Y.H., Zhang, X., Cong, X., Zhang, J., Ji, W. and Hu, P.A., 2018. Moiré phonons in twisted bilayer MoS$_2$. ACS nano, 12(8), pp.8770-8780.

[16] Cappelluti, E., Roldán, R., Silva-Guillén, J.A., Ordejón, P. and Guinea, F., 2013.

Tight-binding model and direct-gap/indirect-gap transition in single-layer and multilayer MoS 2. Physical Review B, 88(7), p.075409.

[17] Roldán, R., López-Sancho, M.P., Guinea, F., Cappelluti, E., Silva-Guillén, J.A. and Ordejón, P., 2014. Momentum dependence of spin–orbit interaction effects in single-layer and multi-layer transition metal dichalcogenides. 2D Materials, 1(3), p.034003.

[18] Slater, J.C. and Koster, G.F., 1954. Simplified LCAO method for the periodic potential problem. Physical Review, 94(6), p.1498.

[19] Cao, Y., Fatemi, V., Fang, S., Watanabe, K., Taniguchi, T., Kaxiras, E. and Jarillo-Herrero, P., 2018. Unconventional superconductivity in magic-angle graphene superlattices. Nature, 556(7699), pp.43-50.

[20] Jin, C., Regan, E.C., Yan, A., Utama, M.I.B., Wang, D., Zhao, S., Qin, Y., Yang, S., Zheng, Z., Shi, S. and Watanabe, K., 2019. Observation of moiré excitons in WSe2/WS2 heterostructure superlattices. Nature, 567(7746), pp.76-80.

[21] Alexeev, E.M., Ruiz-Tijerina, D.A., Danovich, M., Hamer, M.J., Terry, D.J., Nayak, P.K., Ahn, S., Pak, S., Lee, J., Sohn, J.I. and Molas, M.R., 2019. Resonantly hybridized excitons in moiré superlattices in van der Waals heterostructures. Nature, 567(7746), pp.81-86.

[22] Seyler, K.L., Rivera, P., Yu, H., Wilson, N.P., Ray, E.L., Mandrus, D.G., Yan, J., Yao, W. and Xu, X., 2019. Signatures of moiré-trapped valley excitons in MoSe2/WSe2 heterobilayers. Nature, 567(7746), pp.66-70.

[23] Tran, K., Moody, G., Wu, F., Lu, X., Choi, J., Kim, K., Rai, A., Sanchez, D.A., Quan, J., Singh, A. and Embley, J., 2019. Evidence for moiré excitons in van der Waals heterostructures. Nature, 567(7746), pp.71-75.

[24] Eisenstein, J.P. and MacDonald, A.H., 2004. Bose–Einstein condensation of excitons in bilayer electron systems. Nature, 432(7018), pp.691-694.

[25] Weston, A., Zou, Y., Enaldiev, V., Summerfield, A., Clark, N., Zólyomi, V., Graham, A., Yelgel, C., Magorrian, S., Zhou, M. and Zultak, J., 2020. Atomic recon-

struction in twisted bilayers of transition metal dichalcogenides. Nature Nanotechnology, pp.1-6.

[26] Liu, K., Zhang, L., Cao, T., Jin, C., Qiu, D., Zhou, Q., Zettl, A., Yang, P., Louie, S.G. and Wang, F., 2014. Evolution of interlayer coupling in twisted molybdenum disulfide bilayers. Nature communications, 5(1), pp.1-6.

[27] Ceballos, F., Bellus, M.Z., Chiu, H.Y. and Zhao, H., 2014. Ultrafast charge separation and indirect exciton formation in a MoS_2–MoSe2 van der Waals heterostructure. ACS Nano, 8(12), pp.12717-12724.

[28] Ji, Z., Hong, H., Zhang, J., Zhang, Q., Huang, W., Cao, T., Qiao, R., Liu, C., Liang, J., Jin, C. and Jiao, L., 2017. Robust stacking-independent ultrafast charge transfer in MoS_2/WS2 bilayers. ACS Nano, 11(12), pp.12020-12026.

[29] Wang, H.; Yu, L.; Lee, Y.-H.; Shi, Y.; Hsu, A.; Chin, M. L.; Li, L.-J.; Dubey, M.; Kong, J.; Palacios, T. Integrated Circuits Based on Bilayer MoS_2 Transistors. Nano Letters. 2012, pp 4674–4680. https://doi.org/10.1021/nl302015v.

[30] Ramasubramaniam, A.; Naveh, D.; Towe, E. Tunable Band Gaps in Bilayer Transition-Metal Dichalcogenides. Physical Review B. 2011. https://doi.org/10.1103/physrevb.84.205325.

[31] Sun, M.; Xie, D.; Sun, Y.; Li, W.; Teng, C.; Xu, J. Lateral Multilayer/monolayer MoS_2 Heterojunction for High Performance Photodetector Applications. Scientific Reports. 2017. https://doi.org/10.1038/s41598-017-04925-w.

[32] Sahoo, P. K.; Memaran, S.; Nugera, F. A.; Xin, Y.; Díaz Márquez, T.; Lu, Z.; Zheng, W.; Zhigadlo, N. D.; Smirnov, D.; Balicas, L.; Gutiérrez, H. R. Bilayer Lateral Heterostructures of Transition-Metal Dichalcogenides and Their Optoelectronic Response. ACS Nano 2019, 13 (11), 12372–12384.

[33] Bertolazzi, S.; Brivio, J.; Kis, A. Stretching and Breaking of Ultrathin MoS_2. ACS Nano. 2011, pp 9703–9709. https://doi.org/10.1021/nn203879f.

[34] Wang, W.; Klots, A.; Prasai, D.; Yang, Y.; Bolotin, K. I.; Valentine, J. Hot Electron-Based Near-Infrared Photodetection Using Bilayer MoS_2. Nano Lett. 2015, 15 (11), 7440–7444.

[35] Budania, P.; Baine, P.; Montgomery, J.; McGeough, C.; Cafolla, T.; Modreanu, M.; McNeill, D.; Mitchell, N.; Hughes, G.; Hurley, P. Long-Term Stability of Mechanically Exfoliated MoS_2 Flakes. MRS Communications. 2017, pp 813–818. https://doi.org/10.1557/mrc.2017.105.

[36] Zhang, X.; Jia, F.; Yang, B.; Song, S. Oxidation of Molybdenum Disulfide Sheet in Water under in Situ Atomic Force Microscopy Observation. The Journal of Physical Chemistry C. 2017, pp 9938–9943. https://doi.org/10.1021/acs.jpcc.7b01863.

[37] Parzinger, E.; Miller, B.; Blaschke, B.; Garrido, J. A.; Ager, J. W.; Holleitner, A.; Wurstbauer, U. Photocatalytic Stability of Single- and Few-Layer MoS_2. ACS Nano. 2015, pp 11302–11309. https://doi.org/10.1021/acsnano.5b04979.

CHAPTER 3

EXPERIMENTAL SETUP AND CHARACTERIZATIONS

3.1. Lab Space and Facilities

Dr. Jose Perez is the principal investigator (PI) of the Nanomaterials Fabrication and Characterization Laboratory in the Department of Physics at the University of North Texas (UNT). The lab has 1000 sq. ft. of space and contains a chemical vapor deposition (CVD) system consisting of a tube furnace and gas handling system to grow 2D materials such as graphene and MoS_2. The CVD system has a vacuum load lock, introduction chamber, sample transfer system, and multiple gas inlets on each side of the tube. The lab also contains an ultra-high vacuum (UHV) surface characterization system with a scanning tunneling microscope (STM), Auger spectroscopy and low-energy-electron diffraction, electron beam evaporator, and an AFM system. There are 3 workstations with high efficiency particulate air (HEPA) filters, and two fume hoods as shown in Figures 3.1 and 3.2. In addition to this, we have access to advanced nanoscale device fabrication and characterization facilities at the Materials Research Facility (MRF) in the College of Engineering at UNT.

These facilities include electron beam lithography, sputtering, electron beam evaporation, reactive ion etching, metallization and characterization techniques including ellipsometry, high-resolution transmission-electron microscopy (TEM) and scanning electron microscopy (SEM), and a focused ion beam (FIB) system. These facilities are described in detail in the following sections.

FIGURE 3.1. Lab 1 layout showing workstations with HEPA filters for sample preparation.

FIGURE 3.2. Lab 2 layout showing plasma chamber, thermal evaporator, and UHV Auger spectroscopy, low-energy-electron diffraction and scanning tunneling microscope.

3.2. Helium Plasma Chamber for Low-Energy Electron Irradiation Experiments

Graphene has been the object of much research world-wide because of its unique electronic properties as discussed in Chapters 1 and 2. In addition, implementing robust fabrication techniques, will significantly help in integrating graphene into devices. One of these techniques is plasma etching. Plasma has found wide applications in today's world especially in semiconductor manufacturing industries [1-3]. In nature, they appear in interstellar space, stars, lighting strikes, etc. Plasma, known as the fourth state of matter, is an ionized gas, globally neutral, and displays collective effects. Basically, plasma comprises ions, electrons, radicals, and photons, and they can be easily demonstrated in the laboratory. When a gas is heated to certain temperature or subjected to strong electromagnetic fields, it gets ionized. Being constituted by electrical charges, ions and electrons, plasma can response to an electric and magnetic field including those that are produced by itself. In the laboratory, plasma can be created in a vacuum chamber using a flowing gas, and powered electrodes. With sufficient energy, it transforms to free electrons from atoms or molecules, and then both species, ions, and electrons, can coexist. The electrodes are usually powered by an electromagnetic energy. For capacitively-coupled plasma (CCP), an RF power is typically employed while inductively coupled plasma (ICP) uses an induction coil. Plasma is a complex medium that is characterized by a non-linear phenomenon, and understanding its behavior is extremely challenging. In addition, understanding the etching behavior of graphene is very crucial for integration into devices.

29
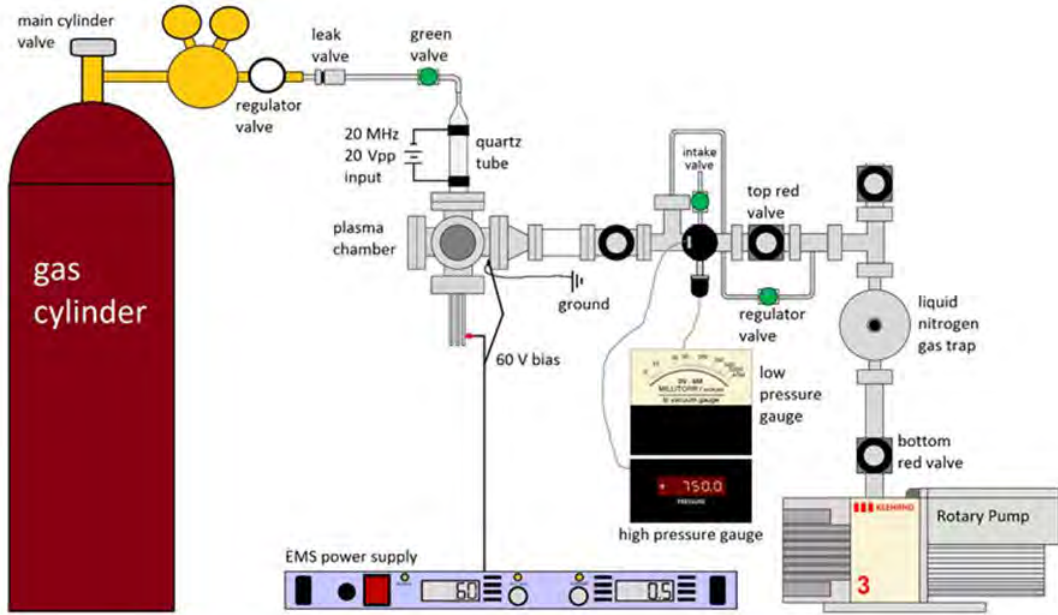
FIGURE 3.3. Schematic of the helium plasma system. Quartz tube is attached to a gas cylinder and the plasma chamber is connected to an EMS power supply for bias application. The rotary pump is the primary means of creating a vacuum in the system. Not shown is an attachable turbo pump, used during annealing (with permission from P. A. Ecton [26]).

Our experimental setup and procedures are described in detail in Refs. [4] and [5]. The comprehensive setup is shown in Figure 3.3. Graphene samples are mechanically exfoliated from highly oriented-pyrolytic graphite (HOPG) using the scotch tape method as shown in Figure 3.7. The sample is mounted on a sample holder with molybdenum clips as shown in Figure 3.5. This is to make electrical contacts on the sample. We check for electrical contacts prior to application, using a multimeter. An ideal resistance would be 0.8 $k\Omega$. The sample is then installed into the plasma chamber. The nitrogen trap is cleaned before installation into the chamber with methanol and wipes to remove contaminants. At this point, the trap has no nitrogen in it. Liquid nitrogen is filled into the trap, and the pump is switched on to pump out gases from the chamber. We employed a liquid nitrogen cooled gas trap which can cool oil vapor down to its condensation point for pressures below 1
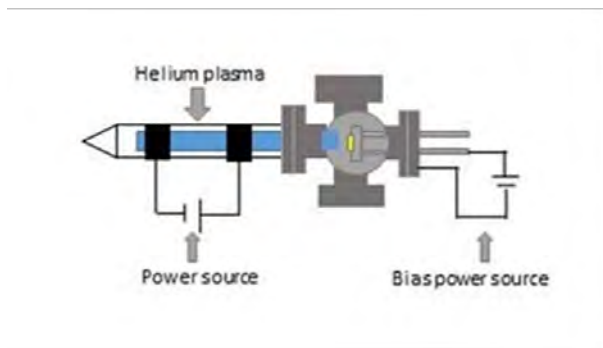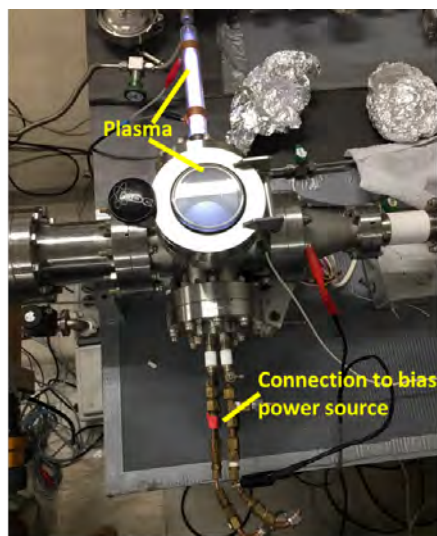
Figure 3.4. Helium plasma irradiation system showing the location of power supply contacts for generation of plasma as well as the location of the power supply for bias application. (a) Shows a high-level schematic of the setup. (b) Shows a picture of the actual system.

Torr. Afterwards, the intake valve is closed. The rotary pump is turned on until the pressure in the chamber reads ≈ 5 Torr. This is to also avoid back diffusion of oil from the pump. The chamber is typically pump down to 10 mTorr. The chamber is filled with Helium (He) gas by opening the gas valve at a pressure of 500 Torr, and then pumped out. This is done for five (5) times, and we refer to this as priming.

Before introducing He gas, the chamber will mostly have an initial pressure consisting of residual air particles, molecular nitrogen, molecular oxygen, and water vapor, and these can disrupt the experiment. As a result, the chamber must be primed before plasma exposure is conducted to ensure almost all the gas reactants are of the desired species, which would be molecular He. After priming, the gas valve is closed. For a constant flow of He, we chose a pressure of about 50 mTorr. The leak valve is cranked gently until a gas flow pressure of 50 mTorr is achieved. In the event of overpressure, we usually adjust the leak and the intake valves accordingly. When the chamber is accurately set with the required parameters, the cables from the DC supply are attached to the sample bias prongs. The red cable (+ve) goes
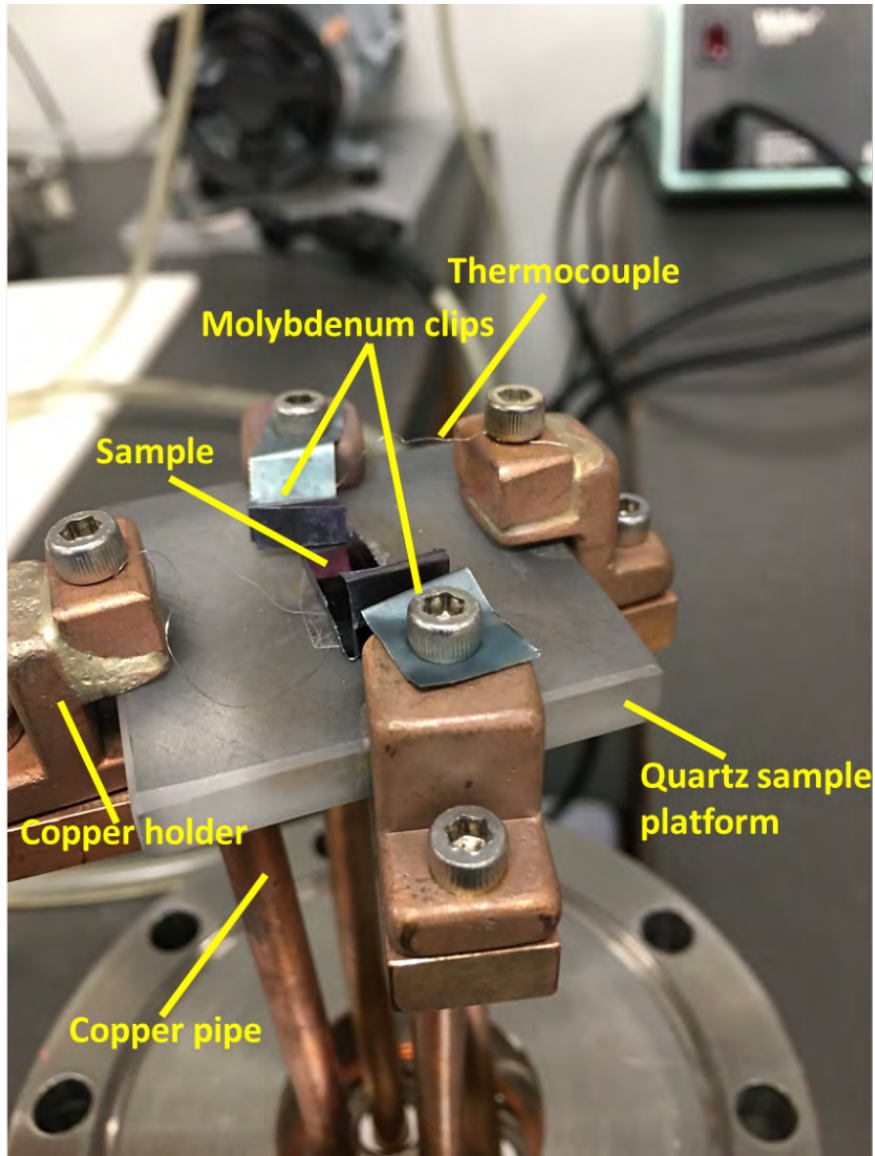
FIGURE 3.5. Sample holder for the helium plasma system. The sample is situated in between the molybdenum clips for ohmic contacts. The thermocouple wires are used for measuring the temperature during sample annealing.

to the sample and the black cable (-ve) goes to the main chamber and vice versa, to attract and repel electrons respectively as shown in Figure 3.4 (b).

The main chamber is always grounded, and we check to make sure it is well connected, for safety purposes. A positive bias on the sample relative to the chamber would attract electrons towards the sample and repels positive gas species within the plasma. A
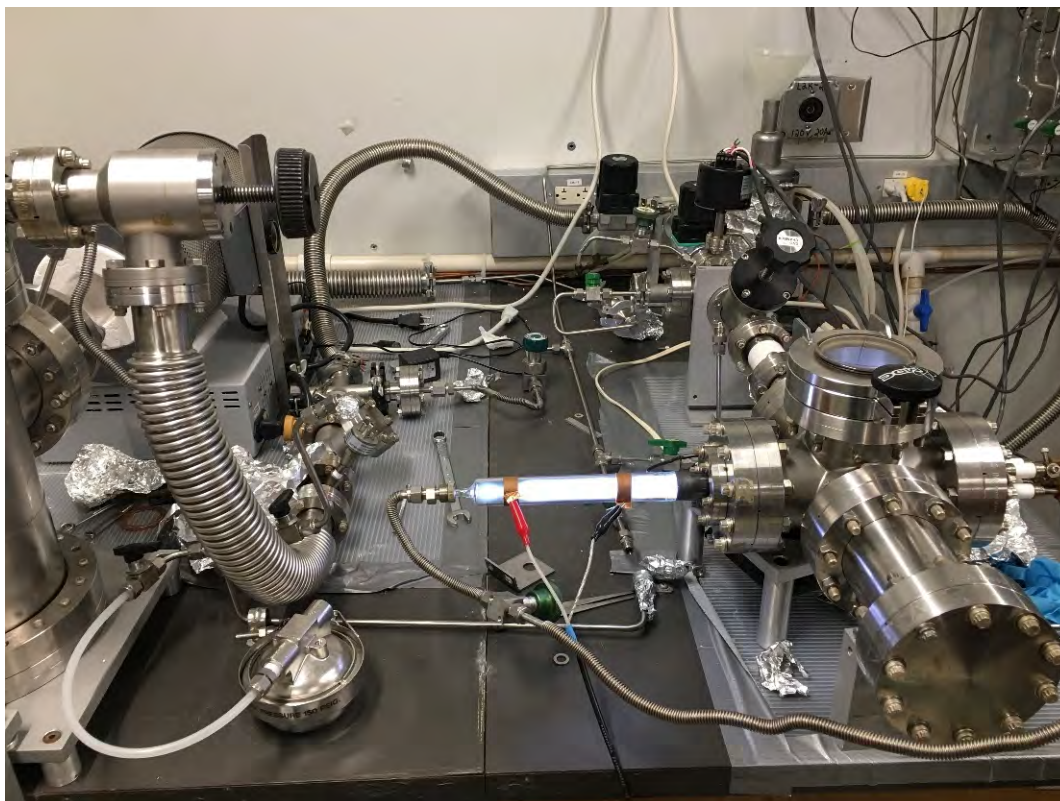
FIGURE 3.6. Quartz tube connected to power supply. The blue glow comes from the plasma that is being generated inside the tube. The electrons derived from the plasma are attracted or repelled to or from the sample respectively.

negative bias would repel electrons and attracts the positive gas species. An ammeter in series measures the current on the sample drawn from the plasma. The RF generator is set to a frequency of 20 MHz, 50 W power supply and a gain supply of about 8.8 V, which is capacitively coupled to two copper electrodes located outside the quartz tube. The gain vernier is cranked up until plasma gets ignited in the transparent quartz tube as shown in Figure 3.6.

A quartz tube is used for the visible part of the chamber and chosen because of its capability to withstand high temperatures generated from the plasma. Afterwards, the potential power supply is cranked up to a bias voltage of 60 V. The plasma exposure is for 30 minutes. The pressure gauges are constantly monitored, for any discrepancies, as maintaining a pressure of 50 mTorr is very critical. After, 30 minutes of irradiation, the

current and voltage from the potential power supply are turned down to zero and switched off. The RF generator and its power supply, and the gain supply are also turned off. The He gas regulator, cylinder valves, and the inlet valve to the quartz tube are tightly closed. The rotary pump is shut down. The nitrogen trap is uninstalled, and the plasma chamber is vented.

3.3. Sample Preparation

Chemical Vapor Deposition (CVD) is a gas phase deposition technique for depositing thin films on substrates. It is usually carried out in furnaces, using gases at high temperatures. CVD has found applications in industry for coating, and depositing dielectrics and polysilicon in semiconductor industries [6, 7]. The exfoliation method for deriving 2D materials is very limited in size, and not practical for high volume manufacturing. Hence, the
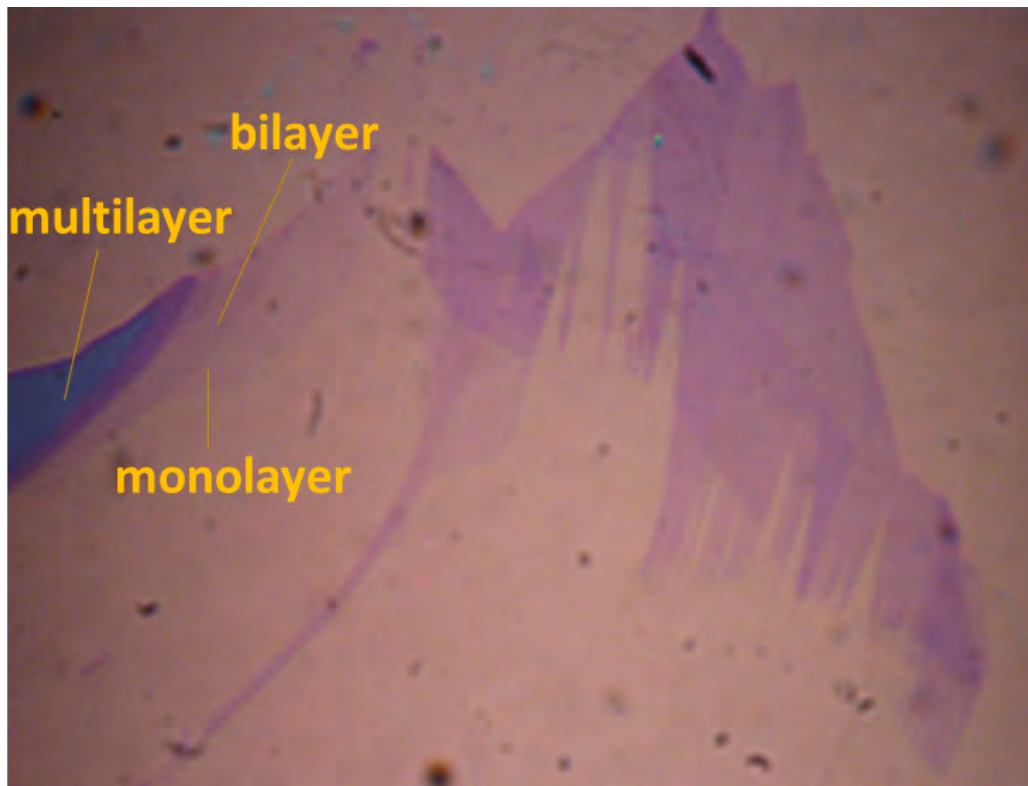
FIGURE 3.7. Shows graphene layers, mechanically exfoliated from HOPG on Si/SiO$_2$, using scotch tape method. The monolayer, bilayer and multilayer can be easily identified from optical microscopy.

need to grow large film domains is very necessary for 2D materials to be used in practical applications [8, 9]. A typical exfoliated graphene from a bulk graphite crystal is $\approx 5~\mu m$ but with CVD method, domains $> 20~\mu m$ can be easily achieved. Figure 3.7 shows a graphene sample exfoliated from highly-oriented-pyrolitic graphite (HOPG) onto 300 nm thick SiO_2 layers on Si substrates.

The CVD growth of our MoS_2 films were carried out in Dr. Philipose's Research Group at the Department of Physics. The films were synthesized on SiO_2/Si substrates [10, 11]. The substrates were subjected to the standard cleaning procedure with acetone and isopropyl alcohol. The novelty of this technique is the use of two different substrates referred to as the precursor and growth substrates. The precursor substrate functions as the Mo source. It is spin coated with an aqueous solution of 20 mg/mL $MoO_3/NH_3 \cdot H_2O$. This substrate allows for controlled concentration of MoS_2 vapors in the growth chamber. A second substrate that functions as the growth substrate is spin coated with an aqueous solution of $NaCl/NH_3 \cdot H_2O$ (NaCl, $\geq 99.5\%$, MilliporeSigma). These pre-treated precursor and growth substrates are then placed over an alumina boat, at the center of the high temperature zone of a quartz tube in a 3-zone Carbolite furnace. A separate alumina boat containing 30 mg of sulfur powder ($\geq 99\%$, MilliporeSigma) is placed in the low temperature zone located near the end of the quartz tube. Figure 3.8 (a) shows the locations of the
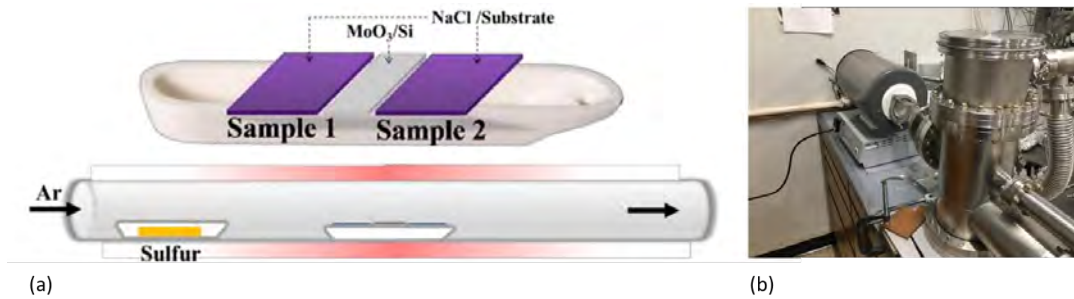
FIGURE 3.8. (a) Schematic of the growth chamber showing sample locations and placements in the furnace [10, 11]. (b) Shows a picture of Thermolyne 21100 tubular furnace. This furnace is different from the growth furnace, and was used for pre-heating samples.

35

precursor and growth substrates along with the sulfur source in the three-temperature-zone furnace. The tube furnace was first heated in air at 900 °C for 2 h and then brought to room temperature (RT). A growth temperature of 800 °C is reached in the main zone of the furnace at a ramp rate of 25 °C/min and held constant for 10 min. During this time, the Ar flow rate is maintained at 500 sccm. The temperature of the sulfur powder located at the edge of the secondary zone is about 120 °C, well above the melting point of sulfur. Sulfur vapors are carried by the inert gas towards the main zone of the furnace where it reacts with the Mo precursor. After 10 min, the furnace is gradually cooled to RT. The advantage of this method lies in the fact that it is possible to tune the growth regime by varying the concentration of NaCl on the pre-treated growth substrate. At a critical NaCl concentration, homogeneously distributed ML MoS$_2$ is produced with controllable dimensions. At high NaCl concentrations, continuous MoS$_2$ films with BL and FL domains are formed. The furnace is then turned off and allowed to cool to RT. We note that the CVD growth furnace and the heating furnace for the films are different. Figure 3.8 (b) shows the Thermolyne 21100 tubular furnace used for heating the samples. The degradation acceleration method we used is described in detail in Refs. [12, 13]. In summary, we pre-heated the samples at temperatures of 285 and 300 °C in a tube furnace in air at atmospheric pressure for 2 h.

3.4. Atomic Force Microscopy

Atomic force microscopy (AFM) technique is a subcategory of scanning probe microscopy (SPM). SPMs use raster scanning tip to measure the surface profile of materials. The information on the surface is gathered and then transmitted to a computer interface where an image of the surface is formed. The surface topography of materials can be measured because of the atomic force of interaction between the tip and the sample surface. The potential between the tip and the sample surface changes depending on the distance between any two atoms from the tip and sample. There are three major imaging modes: contact, non-contact and tapping (intermittent) mode. Apart from topography measurement, AFM can also be used to measure mechanical, electrical, magnetic, and thermal properties of materials [14]. From Lennard-Jones potential $U(r)$ in equation (3.1), the atomic interactions

36

can be described as repulsive and attractive. The first term of the equation represents the atomic repulsive interaction, and the second term represents the atomic attractive interaction. When two atoms are very far apart, there is no interaction between them but as soon that they get closer, attractive force comes to play. In this regime, the non-contact and tapping modes take advantage of this interaction. When the distance between the two atoms is very negligible, repulsive interaction prevails. In this regime, contact mode uses this interaction. Hence, the atomic force changes with the distance between the two atoms. As illustrated in Figure 3.9 (a). The main components of AFM are the XY and Z scanner, the tip, laser, and photodetector. The scanner can raster on the sample surface to get the topography information. A 3D image is formed based on this degree of freedom. The probe or tip is attached to a cantilever, the very end of the tip is used for interacting with the sample surface. The laser is used to monitor the cantilever's position. The laser beam can be tracked using the photodetector. Deflections, as the cantilever bends when scanning, is due to the atomic interactions. This is converted to electrical signal for the feedback. Therefore, a 3D topography image can be obtained.

$$(3.1) \qquad\qquad U(r) = +\frac{B}{r^{12}} - \frac{A}{r^6}$$

$$(3.2) \qquad\qquad F = -\frac{dU(r)}{dr}$$

$U(r)$ is the interatomic potential between the two atoms, r is the distance of separation between the two atoms, B and A gives a measurement of how close two nonbonding atoms are, and how strongly they can interact, and F is the atomic force.

In our laboratory, AFM measurements were carried out using a Q-Scope™ 250/400 Nomad™ from Ambios Technology Corporation as shown in Figure 3.9 (b). The scan head is 80 μm, capable of laterally imaging surface features on the order of nanometers and step heights on the order of angstroms. In our experiments, tapping (wave-mode) imaging was employed because contact mode probes usually have a higher tendency to damage samples. Wavemode is a type of intermittent contact imaging, in this imaging mode, high stiffness

cantilevers are set into oscillatory motion with a resonance frequency, by a separate piezo-electric vibrator. The high cantilever stiffness allows for oscillatory frequencies between 70 and 200 kHz. We used a 160 kHz resonance frequency. All data acquisitions were in TIFF formats. For further analysis and image processing, tilt removal filters were used to flatten images for background corrections, using a program called Gwyddion [15]. This is a freeware modular program for SPM (scanning probe microscopy) data visualization and analysis. Primarily, it is intended for the analysis of height fields of samples, obtained by scanning probe microscopy techniques like AFM.

3.5. Raman and Photoluminescence Spectroscopy

Raman spectroscopy is a vibrational spectroscopic technique that provides unique information about the molecular vibrations and crystal structures of molecules, discovered by C.V. Raman [16]. When light interacts with matter, it can either be absorbed or scattered. There are two types of scattering: Rayleigh scattering and Raman scattering. The Rayleigh scattering occurs when molecules absorbs light, goes to a virtual state, and then falls back to the initial state, thereby emitting energy that was originally absorbed. Here, the absorbed and emitted energy have the same values. In Raman scattering, the molecule that absorbed
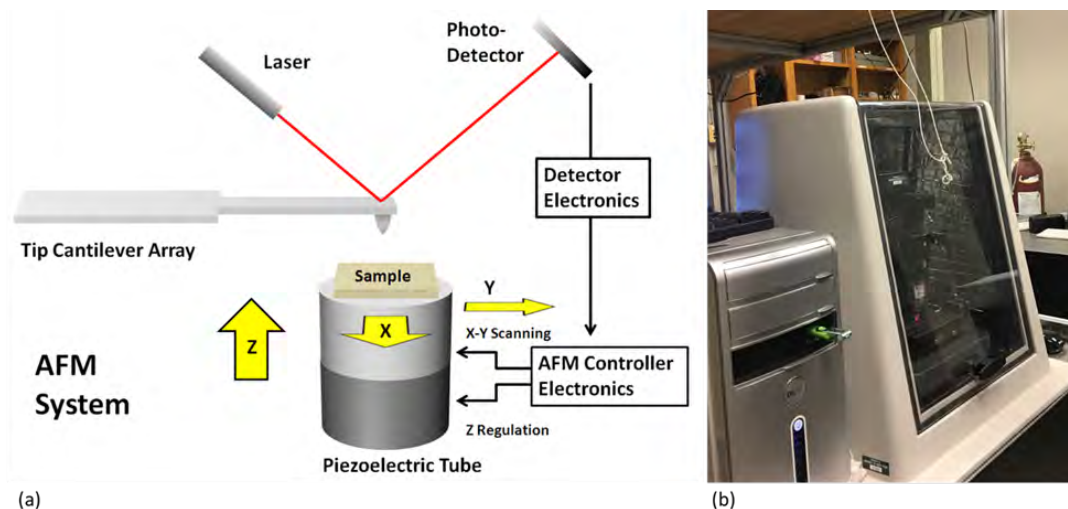
FIGURE 3.9. (a) Shows a schematic of an atomic force microscopy setup. (b) Shows a picture of the actual system.

light goes to a virtual state and falls back to a final state which is different from the initial state. When it emits energy it falls back down, the frequency of the energy of the light is going to be different to the incident light. Scattering occurs when the energy of the radiation does not match any energy separations in the molecule, it will be transmitted most of the time, or scattered at a small fraction of the times. Scattering can be thought of as two-photon process i.e. incident photon and scattered photon. The Rayleigh scattering is an elastic scattering while the Raman scattering is an inelastic scattering. If scattered photon is less energetic than the incident photon, the molecule has gained energy, and this called the Stokes scattering. If the scattered photon has gained energy from the molecule, this is called Anti-Stokes scattering. From classical electrodynamics, Raman scattering is based on the vibrational modulation of molecular polarizability as described in equations (3.3 – 3.10). This involves the interaction of a molecule with an incident electromagnetic wave (light), this interaction produces a dipole moment i.e. a molecular dipole moment is induced, leading to scattering of the incident light. The interaction of light and the molecule to produce a dipole moment generates an oscillating dipole moment which emits radiation (light scattering). The basis of the induced dipole moment stems from the polarizability of the molecule. The polarizability of the molecule is a function of nuclear coordinates or vibrations of the molecule.
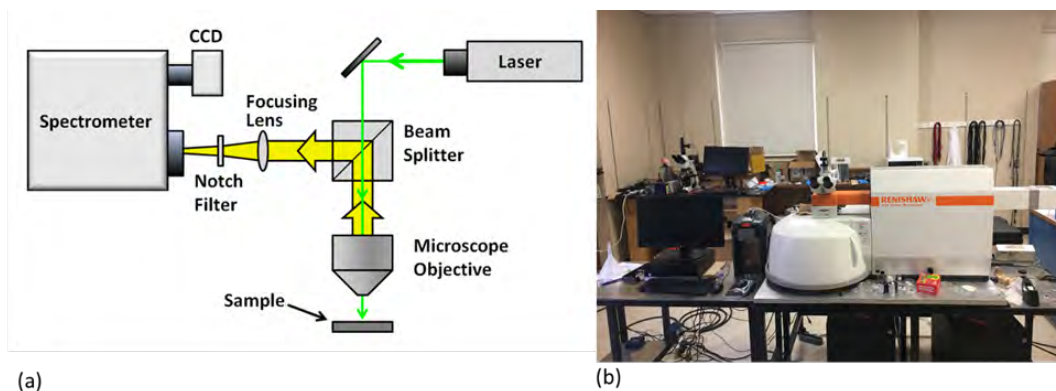
FIGURE 3.10. (a) Shows a schematic of Raman spectroscopy setup. (b) Shows a picture of the actual system.

39

The Raman spectrometer has an elegant working principle, the laser unit which creates light which goes through some mirrors, reflected by lenses, and goes through the sample. It is then deflected by a mirror to a detector as illustrated in Figure 3.10 (a). The change of the dipole moment vector, $\vec{p}$ depends on the electric field, $\vec{E}$ through a polarizability tensor, α given as [17, 18]:

$$(3.3) \qquad \vec{p} = \alpha \vec{E}$$

For a plane wave with frequency ω_0, the corresponding electric field vector can be described as:

$$(3.4) \qquad \vec{E} = \vec{E_0} \cos(\omega_0 t)$$

We can approximate the polarizability using the first order Taylor series:

$$(3.5) \qquad \alpha = \alpha_0 + \frac{\partial \alpha}{\partial Q} dQ$$

We assume that the molecules have a vibrational frequency ω_v and the individual atoms are moving in a harmonic manner about the equilibrium position. The normal coordinates displacement around this equilibrium can be described as follows:

$$(3.6) \qquad dQ = Q_0 \cos \omega_v t$$

Therefore, we can derive a new expression for the induced dipole moment. Applying trigonometric identity, this becomes:

$$(3.7) \qquad \vec{p} = \alpha_0 \vec{E_0} \cos(\omega_0 t) + \frac{\partial \alpha}{\partial Q_k} \frac{Q_0 \vec{E_0}}{2} \{\cos((\omega_0 - \omega_v)t + \cos((\omega_0 + \omega_v)t))\}$$

As discussed earlier and derived in equation (3.7), Raman scattering consists of Stokes and anti-Stokes scattering. In this equation, the radiating dipoles terms are clearly distinguished. The first term describes Rayleigh scattering while the second term describes Stokes and Anti-Stokes scattering. The dipoles could be Raman active or inactive. If the factor that is common to both Raman dipoles is zero, vibration mode is not Raman active, and this leads

to no Raman scattered light. The average radiated power from an electric dipole oscillation, induced in a molecule by an electric field of frequency ω_d, is written as:

$$(3.8) \qquad P_d = \frac{|p_d|^2 w_{\mathrm{d}}^4}{12\pi\epsilon_0 C^3}$$

p_d can be easily obtained from equation (3.8). Stokes and anti-Stokes power, $|p_d|$ can be expressed as:

$$(3.9) \qquad |p_d| = \frac{\partial \alpha}{\partial Q_k} \frac{Q_0 E_0}{2}$$

Therefore, if:

$$(3.10) \qquad \frac{\partial \alpha}{\partial Q_k} = 0$$

This implies that Raman is in inactive mode.

The facilities for Raman and PL spectroscopy characterization were provided by Dr. Cui at the Department of Physics as shown in Figure 3.10 (b). This laboratory contains a Renishaw inVia Raman Microscope with a minimum spot size of 764 nm, Renishaw Centrus CCD detector, and a spectral resolution of 1.75 cm^{-1}. The system can acquire Raman and PL spectroscopy maps with a minimum stage step size of 0.1 μm. The system uses the Renishaw WiRE 5.2 software to generate maps of fitted peak heights, positions, shifts, and full-width-at-half maxima (FWHMs). Such maps are useful in determining variations in peak position and FWHM caused by defects and strain [19]. We also utilized a Raman system at MRF for the SEM irradiation experiments on graphene. This a Thermo Electron Almega XR with an excitation laser wavelength of 532 nm, spot size of 0.6 μm^2, laser power of 6 mW, and a spectral resolution of 2 cm^{-1} [20]. It is well-known that monolayer graphene has a characteristic G peak at 1580 cm^{-1} and a sharp 2D peak at about 2700 cm^{-1} [21].

Photoluminescence (PL) spectroscopy has been often associated with Raman spectroscopy. PL is a technique that comprises phosphorescence and fluorescence processes. This process originates from absorption or emission between different electronic energy levels in the sample. Photons are emitted as the electron returns to the ground state or valence band as shown in Figure 3.11. The amount and type of PL depends on the laser wavelength and

the material composition. An appropriate laser wavelength is selected to avoid unwanted fluorescence. There are specific vibrational modes that appear for MoS_2 films. These are the Raman peaks associated with the crystalline structure of MoS_2. They appear at about 384 cm^{-1} and 409 cm^{-1} [22]. It is expected that if there is a degraded bilayer, then these peaks will broaden. Raman spectroscopy gives more detailed information on the crystallinity
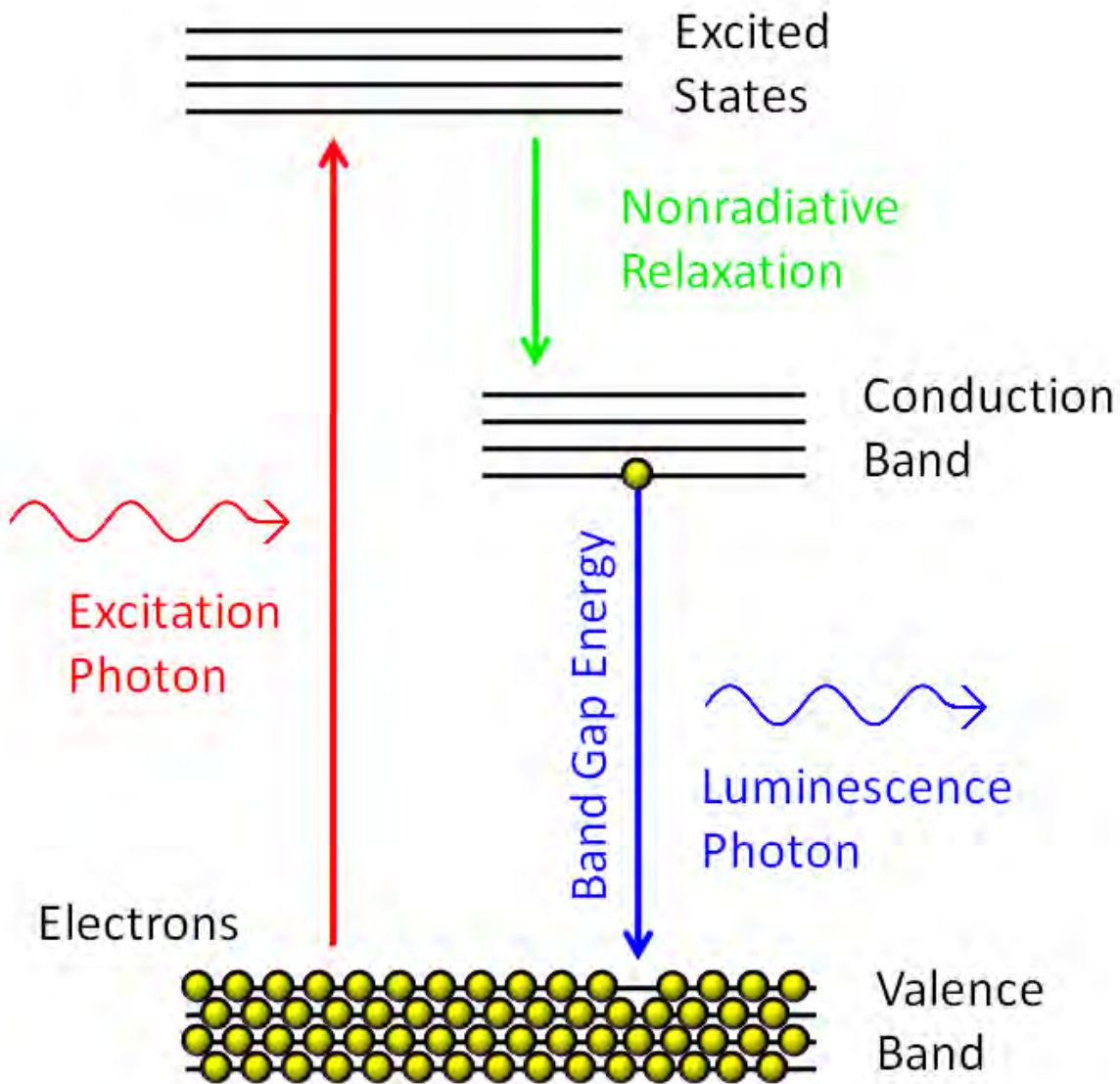
FIGURE 3.11. Shows a schematic of the energy diagram illustrating the photoluminescence process.

of the bilayer and multilayer MoS_2 samples. Although they structurally appear to not be degraded, in our experiments, using atomic force microscopy, their atomic lattice structure appears to have been affected by ambient air exposure. Raman spectroscopy informs in more detail about the crystallinity of the lattice. It is well known that Raman and Photoluminescence spectroscopy can be collected simultaneously for 2D MoS_2 [23]. In addition to the Raman spectra, using 532 nm laser excitation, we also collected photoluminescence data simultaneously. The photoluminescent is in a region about 4500 cm^{-1} from the laser line. The combination of Raman and photoluminescence data provided more information on the stability of the bilayer and multilayer MoS_2 samples as described in Ref. [13].

3.6. The SEM/E-Beam Lithography System

The Scanning Electron Microscope (SEM) is one of the fascinating characterization instruments. The basic principle is the scanning of a fine electron probe over a sample and using a variety of detectors to reconstructs an image from signals generated within the sample. An SEM requires an optical configuration to create a focused electron beam. The main component consists of a column for electron beam generation, a sample stage, a secondary electron detector for acquiring secondary electrons, vacuum pump, a monitor for displaying images connected to an operating system, and control pads [14]. The emitter or electron gun generates a beam of energetic electrons, and this beam is created by applying a potential to tungsten or lanthanum hexaboride. The beam passes through and processed by a set of electromagnetic lenses, focused at the specimen surface, and systematically scanned across the surface of a specimen. The beam is then deflected in the x and y axes by a pair of scanning coils (or deflector plates). These are found below the condenser lens system and associated with the objective lens area. The deflection enables the movement of the beam, as lines of consecutive dwell-times for the beam spot, across a rectangular area of the sample. The secondary electrons are detected by the electron detector. The electronic image is displayed on the computer monitor. SEMs are capable of magnifying samples from about 10 times up to 300,000 times. We made use of the JEOL JSM-7001F Scanning Electron Microscope/e-beam lithography system in the cleanroom at the UNT MRF as shown in

FIGURE 3.12. Shows the JEOL JSM-7001F SEM at the MRF. The SEM is on the left-hand side of the image. The XENOS XPG2 e-beam pattern writer is at the right-hand side of the image, seated on the table.

Figure 3.12. We investigate the effects of electron beam irradiation from this SEM on graphene exfoliated on 300 nm thick SiO_2, at energies of 1.5, 10 and 30 keV at dosages of about 30 C/cm^2. The SiO_2 was thermally grown on a high conductivity Si substrate with a resistivity of 0.01-0.02 Ω-cm. These results show the effects of charging on the substrate, especially at lower energies for which most of the primary beam charge is deposited in the SiO_2. The results are fully explained in Ref. [20]. In our irradiation experiments, the FEB system, JEOL JSM-7001F SEM was running at a pressure of 7 x 10^{-7} Torr. The accelerating voltages of the primary electrons could be varied from 0.5 to 30 kV. The system also included a XENOS XPG2 pattern writer. The primary beam from the SEM was written over an area measuring 2 x 2 μm^2.

3.7. X-ray Photoelectron Spectroscopy

Albert Einstein received the Nobel prize in physics for explaining the photoelectric effect in 1921 [24]. From this principle, Kai Siegbahn developed the modern-day X-ray Photoelectron Spectroscopy (XPS) in the 1950s [25]. XPS is also known as Electron Spectroscopy for Chemical Analysis (ESCA), a technique used to determine the quantitative atomic composition and chemistry of surfaces. Basically, a sample is irradiated with monochromatic soft x-rays and analyzing the energy of the detected electrons, resulting from the emission of photoelectrons whose energies are characteristic of the elements within the sample. Instrumentation includes but not limited to; ultrahigh vacuum system ($\approx 10^{-9}$ Torr), electron energy analyzer, X-ray source, Ar ion gun, neutralizer, electronic controls, and computer system for data acquisition as illustrated in Figure 3.13 (a). XPS spectra are created by plotting the intensities of photoelectrons versus their binding energy. The emitted photoelectron has kinetic energy (K.E) given by:

(3.11) $$K.E = hv - (E_B + \varphi)$$

Where hv is the energy of the photon, E_B is the binding energy of the atomic orbital from which the electron originates, and φ is the work function of the spectrometer.

X-rays excite electrons from a material surface. This is possible for all elements except Hydrogen, since it has just one electron in the inner shell. The electron energy depends on the
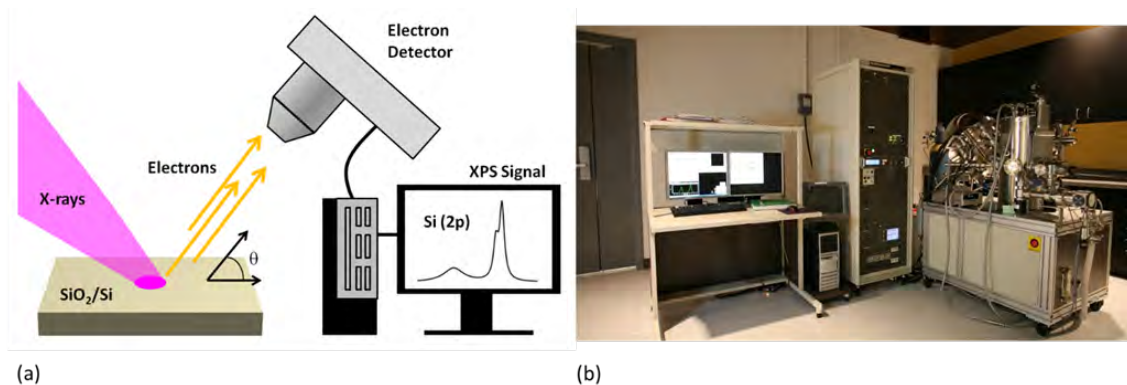
FIGURE 3.13. (a) Shows a schematic of an X-ray photoelectron spectroscopy setup. (b) Shows a picture of the actual system at the MRF.

elemental electron orbital binding energies. XPS can be used to calculate atomic percentage, and to determine layer thicknesses. For oxidation, the states of the atoms can be determined from shifts (chemical shifts) in the binding energies caused by bonding to other atoms. The XPS systems used in this dissertation are located at the MRF in the College of Engineering at UNT. These facilities include a PHI 5000 VersaProbe scanning XPS microprobe with a monochromated Al K-alpha source at 1486.7 eV, as shown in Figure 3.13 (b). This system uses a high flux X-ray source, providing a highly focused monochromatic X-ray beam for $200 \times 200 \ \mu m^2$ sample surface area. In addition, the high resolution 180° spherical capacitor energy analyzer provides analysis capability including XPS spectral, map, depth profile, line scan, and angle resolved analyses. Our results of XPS on MoS_2 degradation experiments are fully described in Ref. [12].

3.8. References

[1] Lee, C.G., Kanarik, K.J. and Gottscho, R.A., 2014. The grand challenges of plasma etching: a manufacturing perspective. Journal of Physics D: Applied Physics, 47(27), p.273001.

[2] Kanarik, K.J., 2020. Inside the mysterious world of plasma: A process engineer's perspective. Journal of Vacuum Science Technology A: Vacuum, Surfaces, and Films, 38(3), p.031004.

[3] Campbell, S.A., 2008. Fabrication engineering at the micro-and nanoscale (No. Sirsi) i9780195320176).

[4] Jones, J.D., Shah, R.K., Verbeck, G.F. and Perez, J.M., 2012. The Removal of Single Layers from Multi-layer Graphene by Low-Energy Electron Stimulation. Small, 8(7), pp.1066-1072.

[5] Jones, J.D., Hoffmann, W.D., Jesseph, A.V., Morris, C.J., Verbeck, G.F. and Pérez, J.M., 2010. On the mechanism for plasma hydrogenation of graphene. Applied Physics Letters, 97(23), p.233104.

[6] Zulehner, W., 2000. Historical overview of silicon crystal pulling development. Materials Science and Engineering: B, 73(1-3), pp.7-15.

[7] Hung, M.H., Lin, T.H., Cheng, F.T. and Lin, R.C., 2007. A novel virtual metrology scheme for predicting CVD thickness in semiconductor manufacturing. IEEE/ASME Transactions on mechatronics, 12(3), pp.308-316.

[8] Yu, H., Liao, M., Zhao, W., Liu, G., Zhou, X.J., Wei, Z., Xu, X., Liu, K., Hu, Z., Deng, K. and Zhou, S., 2017. Wafer-scale growth and transfer of highly-oriented monolayer MoS_2 continuous films. ACS nano, 11(12), pp.12001-12007.

[9] Liu, H.F., Wong, S.L. and Chi, D.Z., 2015. CVD growth of MoS_2-based two-dimensional materials. Chemical Vapor Deposition, 21(10-11-12), pp.241-259.

[10] Jiang, Y., Lin, Y., Cui, J. and Philipose, U., 2018. Effects of strategically placed water droplets on monolayer growth of molybdenum disulfide. Journal of Nanomaterials.

[11] Jiang, Y., Lin, Y., Littler, C., Syllaios, A.J., Neogi, A. and Philipose, U., 2021. Analyzing growth kinematics and fractal dimensions of molybdenum disulfide films. Nanotechnology, 32(24), p.245602.

[12] Yao, K., Femi-Oyetoro, J.D., Yao, S., Jiang, Y., El Bouanani, L., Jones, D.C., Ecton, P.A., Philipose, U., El Bouanani, M., Rout, B., Neogi, A., and Perez, J.M., 2019. Rapid ambient degradation of monolayer MoS_2 after heating in air. 2D Materials, 7(1), p.015024.

[13] Femi-Oyetoro, J., Yao, K., Hathaway, E., Jiang, Y., Ojo, I., Squires, B., Neogi, A., Cui, J., Philipose, U., Gadiyaram, N.K., Zhou, W., and Perez, J., 2020. Long-term Stability of Bilayer MoS_2 in Ambient Air. arXiv preprint arXiv:2010.06770.

[14] https://myscope.training/

[15] Nečas, D. and Klapetek, P., 2012. Gwyddion: an open-source software for SPM data analysis. Open Physics, 10(1), pp.181-188.

[16] Raman, C.V. and Krishnan, K.S., 1928. A new type of secondary radiation. Nature, 121(3048), pp.501-502.

[17] D. A. Long. Classical Theory of Rayleigh and Raman Scattering. pp 31–48, 2002.

[18] Raza, A., 2019. Raman spectroscopy enhanced by on-chip dielectric and metal

waveguides (Doctoral dissertation, Ghent University).

[19] Rice, C.; Young, R. J.; Zan, R.; Bangert, U.; Wolverson, D.; Georgiou, T.; Jalil, R.; Novoselov, K. S. Raman-Scattering Measurements and First-Principles Calculations of Strain-Induced Phonon Shifts in Monolayer MoS_2. Physical Review B. 2013. https://doi.org/10.1103/physrevb.87.081307.

[20] Femi-Oyetoro, J.D., Yao, K., Roccapriore, K., Ecton, P.A., Tang, R., Jones, J.D., Verbeck, G. and Perez, J.M., 2019. Effects of high-dosage focused electron-beam irradiation at energies 30 keV on graphene on SiO_2. Applied Surface Science, 469, pp.325-330.

[21] Reich, S. and Thomsen, C., 2004. Raman spectroscopy of graphite. Philosophical Transactions of the Royal Society of London. Series A: Mathematical, Physical and Engineering Sciences, 362(1824), pp.2271-2288.

[22] Li, H., Zhang, Q., Yap, C.C.R., Tay, B.K., Edwin, T.H.T., Olivier, A. and Baillargeat, D., 2012. From bulk to monolayer MoS_2: evolution of Raman scattering. Advanced Functional Materials, 22(7), pp.1385-1390.

[23] Tuschel, D., 2016. Photoluminescence spectroscopy using a Raman spectrometer. Spectroscopy, 31(9), pp.14-21.

[24] A. Einstein, 1905, 1921 Nobel Prize in Physics, Ann. Physik 17, 132.

[25] K. Siegbahn, Et. Al.,1967, Nova Acta Regiae Soc.Sci., Ser. IV, Vol. 20.

[26] Ecton P.A., 2016. Low-Energy Electron Irradiation of Preheated and Gas-Exposed Single-Wall Carbon Nanotubes (Doctoral dissertation, University of North Texas).

CHAPTER 4

EFFECTS OF HIGH-DOSAGE FOCUSED ELECTRON-BEAM IRRADIATION AT ENERGIES ≤ 30 KeV ON GRAPHENE ON SiO_2 [1]

4.1. Background

We report the effects of electron irradiation on graphene at energies ≤ 30 keV, to understand the cutting or etching of two-dimensional (2D) materials using electron systems from a scanning electron microscope (SEM). For example, in focused electron-beam (FEB), an electron beam (e-beam), typically from an SEM system, is used together with an ambient gas to cut and etch nanostructures, films and 2D materials. The electrons in the beam dissociate the gas into reactive species including ion species that etch the material in question. The advantage of using an SEM system instead of a transmission electron microscope (TEM), helium ion microscope, or e-beam based lithography system involving the use of a resist, are cost and avoidance of detrimental effects due to resist residue. The latter is particularly important for 2D materials because resist residue can dope and change the electronic properties of these materials. Although FEB techniques have been studied and used on a variety of materials, including 2D materials, none of these studies, to our knowledge, have investigated the effects of substrate charging on the precision, resolution, and line width of the patterns, or whether there could be direct-write without involving gas species. When a dielectric substrate is used as the supporting substrate for the film, nanostructure or 2D material, charge build up in the dielectric substrate due to the e-beam can occur. Depending on the total emitted electron yield of the dielectric substrate the charge built up can be positive or negative and spread over a region in the substrate considerably larger than the width of the electron beam. This charge in the substrate can attract the ion species in the gas that can react with the material being etched and increase the linewidth, while decreasing the precision and resolution.

We investigate the effects of electron beam irradiation from an SEM on graphene exfoliated on 300 nm thick SiO_2 at energies of 1.5, 10 and 30 keV, at dosages of about 30 C/cm^2. The SiO_2 was thermally grown on a high conductivity Si substrate with a resistivity of 0.01-0.02 Ω-cm. These results show the effects of charging on the substrate, especially at lower energies for which most of the primary beam charge is deposited in the SiO_2 [1]. In our irradiation experiments, the FEB system was a JEOL JSM-7001F SEM system running at a pressure of 7×10^{-7} Torr. The accelerating voltages of the primary electrons could be varied from 0.5 to 30 kV. The system also included a XENOS XPG2 pattern writer. The primary beam was written over an area measuring 2 x 2 μm^2. The primary beam was controlled by the pattern writer to write the square area by tracing a spiral starting from the perimeter of the square and traveling inwards towards the center. This trace pattern had been found to minimize the effects of charging in the past. As stated previously, the incident energies were 1.5, 10 and 30 keV. In all the experiments and data described in this section, the primary beam current was 0.64 nA, the total primary electron dosage was 28.8 C/cm^2, and total exposure time was 30 min. The parameters of total primary electron dosage and exposure time are like those used in the work of Thiele et al. [2]. The main objective of these studies was to see if the graphene would etch without the presence of a gas such as oxygen in the chamber that would dissociate under electron irradiation and produce reactive radicals that would etch the graphene. One may speculate that oxygen from the SiO_2 substrate may dissociate and react with the graphene causing it to etch.

Chen et al. [3] proposed that electron can dissociate oxygen atoms from SiO_2, and the dislodged O to reacts with graphene at defect sites, caused initially by the electron beam. However, we found no evidence for this. It appears that the SiO_2 substrate remains inert to the graphene during e-beam exposure. Since oxygen would be the only reactive species that would dissociate from the SiO_2. At lower energies, graphene monolayers on SiO_2 show effects that we attribute to the SiO_2 charging and contaminating with hydrocarbons. Carbon contamination is a result of primary, backscattered, or secondary electrons from the surface dissociating hydrocarbons in the chamber. Additionally, in dielectrics, because of

electrons being trapped at defects in the substrate, charging occurs. This phenomena in dielectric substrates have been reported to be caused by the migration of charged defects that can lead to volume expansion and outgrowths on the surface [4-6]. At higher e-beam energies various effects change such as dissociation cross sections for gases, hydrocarbon contamination, backscattered and secondary electron yields from the SiO_2, and the amount of primary beam electron charge deposited in the substrate. Also, most of the primary beam electrons have traversed through the SiO_2 without deflection and made it to the grounded conducting Si substrate, leaving graphene unetched. In this project, we present the effects and mechanisms of electron-beam irradiation on graphene on SiO_2.

4.2. Abstract

We investigate the effects of focused electron-beam irradiation on exfoliated graphene on SiO_2 substrates at energies of 1.5, 10 and 30 keV and dosage of 28.8 C/cm^2. Our objective is to understand the mechanism by which wide-area low-energy electron irradiation thins such samples. We test a previously reported mechanism in which the incident electrons produce defects in the graphene, pass through the graphene, and dissociate oxygen from the SiO_2 underneath. The dissociated oxygen then reacts with graphene, etching it from below. We conclude that although oxygen may play a role in the etching, incident electrons at 1.5, 10 and 30 keV that pass through the graphene do not etch it. We propose wide-area irradiation may dissociate oxygen from the uncovered SiO_2 substrate surrounding the graphene and produce etching from above.

4.3. Introduction

Experimental studies of electron beam effects on bare SiO_2 have been known as far back as 1970s. It has been reported that electron-beam irradiation on SiO_2 produces various effects. One of the major contributions was that, after irradiation, dissociation was observed on the SiO_2 surface, leaving behind an elemental Si surface. It was concluded that electron-beam energy, current density, the presence of impurities on the surface, and the residual gas pressure of oxygen played a key role for the mechanism behind SiO_2 damage

[7]. Another significant contribution was the discovery of electron-hole transport in SiO_2 films. Here, it was discovered that both holes and electrons travel across most of the SiO_2 surface without a significant amount of permanent trapping. It was proposed that the occurrence of a trapped positive charge at or near the SiO_2/Si interface is a significant fraction of the collected charge, indicating that some of the holes that migrate to the interface do not penetrate it [8]. Recently, the effects of electron irradiation of graphene on SiO_2 substrate have been extensively explored. Studies of electron irradiation of exfoliated graphene has primarily been on 300 nm thick SiO_2 at electron accelerating voltages in the range < 30 keV. This is because typically at energies in the range > 85 keV there is usually a knock-on collision of carbon atoms from the carbon matrix of graphene. These fundamental studies are necessary to potentially demonstrate an experimental condition for the optimization of graphene characterization and device fabrication. Presently, a detailed mechanism on the effects of electron irradiation on graphene has not been reached. Therefore, a clear mechanism is crucial. We investigate the effects of e-beam irradiation at energies of 1.5, 10 and 30 keV and dosages of about 30 C/cm^2 on monolayer graphene mechanically exfoliated on 300 nm thick SiO_2 thermally grown on a high conductivity Si substrate with a resistivity of 0.01-0.02 Ω-cm. The main objective of these studies was to see if the graphene would etch without the presence of a gas such as oxygen in the chamber. However, we found no evidence for this. It appears that the SiO_2 substrate remains inert to the graphene during e-beam exposure.

Graphene, a two-dimensional sheet of sp^2-bonded carbon atoms arranged in a hexagonal lattice, has attracted tremendous amounts of research because of its electronic properties that make it ideal for future devices [9]. Understanding the mechanism by which graphene etches and its behavior under e-beam irradiation is especially essential for understanding how to integrate it into future devices. There have been many previous publications on the low-energy (< 86 keV) electron irradiation effects on graphene exfoliated on SiO_2 [3, 10–14]. The value of 86 keV is the minimum energy to directly transfer momentum and cause knock-on damage to graphene [15].

Teweldebrhan and Balandin [10] performed electron irradiation on graphene with energies 5 keV and 20 keV of about 4-20 mC/cm^2 using a field-emission system. They observed an appearance of D peak from the Raman spectra, which attains its maximum after few minutes, and then begins to decrease as the electron irradiation dosage increase. They finally proposed that there is an amorphization of graphene, in which graphene is transformed to nanocrystalline and then to amorphous state as they increased the dosage. Childres et al. [16] studied the electronic transport properties of graphene after irradiating with a beam energy of 30 keV and a dosage of 60 mC/cm^2 using a scanning electron microscope. After electron irradiation, they observed a D peak in the Raman spectra, a decrease in the carrier mobility and a decrease in the charge neutrality point (CNP). They proposed that the cause of the damage after the electron irradiation led to trapping of holes. They further claimed that the electron doping was due to the interaction of the electron beam with the substrate at the SiO$_2$/Si interface. Xu et al. [14] performed electron irradiation on graphene samples with a 10 keV electron beam at a dosage of 3.6×10^5 C/cm^2 using an Auger electron spectroscope. They observed that apart from the appearance of a D peak, the G peak became significantly higher in intensity than the 2D peak. After doing Auger spectroscopy, they concluded that there are induced chemical reactions and structural transformations. They propose that the electron beam decomposed the SiO$_2$ substrate which created mobile oxygen atoms, and these oxygen atoms are responsible for etching the graphene.

Michalik et al. [17] used a field-emission scanning electron microscope for Electron Beam Induced Deposition (EBID) technique, to pattern cobalt contacts on graphene, using an electron irradiation dosage of 2000 mC/cm^2 and an accelerating voltage of 10 keV. They observed that the damage observed on graphene is due to precursor gas, and the molecules from the precursor gets attached to the graphene, which finally gets dissociated by the electron beam. They further observed that the induced damage can be removed by heating the samples. Thiele et al. [7] presented an electron-beam-induced oxidation of single- and bilayer graphene with Ti/Pt contacts, using a low-voltage scanning electron microscopy technique. They used an acceleration voltage of 3 keV. During this process, they injected

oxygen into the experimental setup, and they observed targeted etching at the focal point, enabling them to pattern graphene. In addition, their voltage-contrast imaging experiments was backed up with finite-element simulations. They concluded that secondary-electron intensities are responsible for etch profiles. Hari et al. [18] irradiated exfoliated graphene with electron exposure of 5 keV accelerating voltage and beam dosage of 2000 mC/cm^2 using a 3D field-emission gun dual beam system, they observed that the Raman spectra changed in the peak intensities due to degradation from the precursor gas. They conclude that graphene on SiO$_2$ is damaged due to the presence of oxygen atoms in the substrate.

In a recent paper, Chen et al. [3] proposed that because of electron irradiation, pristine graphene develops defects, and the incident electrons go through the graphene and dissociate oxygen from the SiO$_2$ underneath. In the model, the oxygen desorbs and reacts with the defective graphene, etching it from below. The incident electrons used in these studies had energies of 50-200 eV and dosage of about 30 C/cm^2 and were generated by a divergent electron cyclotron resonance (DECR) plasma system. This is a wide-area plasma electron source, that irradiated the whole sample including the uncovered SiO$_2$ substrate. They noted that incident electrons at these energies cannot reach the substrate since the electron mean free path is about 0.5 nm. Consequently, it was reported that secondary electrons produced by the incident electrons traverse to the substrate and cause oxygen dissociation. They concluded that the whole process could be more complicated. Comprehensively, it is seen that a well-defined and detailed mechanism is yet to be achieved on the electron irradiation effects of graphene exfoliated on SiO$_2$ at energies < 80 KeV.

In this work, we test this mechanism by using an e-beam lithography system to focus an e-beam on specific areas of the graphene that exclude the uncovered SiO$_2$, and present Raman spectroscopy data to determine if the graphene was etched. Our results provide new information on the thinning mechanism. Previous reports have shown that the dosage at which low-energy electron irradiation is carried out has a significant effect on graphene exfoliated on SiO$_2$. A typical field emission scanning electron microscopy (SEM) image of a sample may involve a beam current of 0.5 nA, an image area of 10×10 μm^2, and a

total irradiation time of 60 s. The resultant dosage would be 30 mC/cm^2. Using an SEM system at energies of 5 and 20 keV and dosages of 4–20 mC/cm^2, the appearance of a sharp Raman D peak in graphene was reported by Teweldebrhan and Balandin [10] and attributed to amorphitization. This D peak was found to be reversible in that it disappeared after annealing the sample at 200 °C for 30 min, and consequently attributed instead to graphene hydrogenation [11]. A reversible D peak was observed for incident energies from 100 eV to 30 keV and dosages from 1 mC/cm^2 to 1 C/cm^2 [11]. In addition to focused e-beam studies, there have also been studies using plasma electron sources in which the whole sample is irradiated. These studies have also shown the appearance of a reversible D peak at low dosages [12]; however, at dosages starting at about 0.4 C/cm^2, layer-by-layer thinning of graphene was observed and attributed to electron stimulated dissociation of carbon atoms [13]. Chen et al. [3] reported that thinning occurs using whole-sample irradiation at 200 eV for thin carbon films deposited on SiO$_2$ but not Si. Although they did not carry out similar experiments on exfoliated graphene on Si, they proposed that their mechanism was applicable to both exfoliated graphene and thin carbon films on SiO$_2$. According to them, the oxygen atoms diffuse outwards from underneath the graphene sample and etch the sample. A similar mechanism had been proposed by Xu et al. [14] to explain graphene layer removal because of e-beam irradiation at 10 keV from an Auger microscopy system. However, in these experiments, the irradiated area consisted of a nanometer-scale spot on which the e-beam was focused for about 30 min, and the resulting dosage was about 3.6×10^5 C/cm^2, about 4 orders of magnitude larger. Such large dosages are impractical for lithography and may produce other causes for thinning such as sample heating. If the mechanism proposed by Chen et al. [3] were correct, then it should also apply to focused e-beam irradiation at comparable dosages and higher energies for which it is well-known that oxygen species desorb from SiO$_2$ [19, 20].

4.4. Material and Methods

The graphene samples used in our experiments were mechanically exfoliated from highly oriented pyrolytic graphite (HOPG) onto a 300 nm SiO$_2$ substrate grown on a degener-

ately doped conducting silicon wafer. We determined monolayers using Raman spectroscopy [21] for the wide-area irradiation experiments, and optical microscopy for the e-beam irradiation experiments. The latter was done to avoid any possible effects due to the laser beam. In our irradiation experiments, we used a lithography system consisting of a JEOL JSM-7001F SEM system at a base pressure of 7×10^{-7} Torr capable of accelerating voltages from 0.5 to 30 kV, and a XENOS XPG2 e-beam pattern writer. The irradiated area was a 2×2 μm^2 square, and the path at which the e-beam exposed the square area was a spiral starting from the outer perimeter of the area going inwards. We used incident energies of 1.5, 10 and 30 keV. For all samples shown in the figures, the beam current was 0.64 nA, dosage 28.8 C/cm^2 , and total irradiation time 30 min. The dosage and irradiation time are at a comparable level to those in the experiments of Chen et al. [3] in which about 7 monolayers were removed from a multilayer flake at 50 eV, and the electron energies are much higher. We found that e-beam energies less than 1.5 keV resulted in loss of resolution and beam stability due to charging of the SiO$_2$ substrate. It has been reported that at incident electron energies of 2 keV, the desorption of O$^-$ ions from SiO$_2$ is about an order of magnitude greater than that of O$^+$ ions; and, the O$^-$ yield has a maximum at about 1.5 keV that is about an order of magnitude greater than the yield at 200 eV [19, 20]. The yield at 50 eV is less than the yield at 200 eV. Therefore, if the etching were due to such oxygen species, then more graphene would etch at 1.5 keV than at 50–200 eV. Scanning electron microscopy images were taken immediately after irradiation using the same system. In e-beam lithography of a standard resist such as polymethacrylate (PMMA), energies are typically > 30 keV to increase resolution and minimize beam spread in the resist, and dosages are 100–500 $\mu C/cm^2$. The dose level in our experiments is roughly five orders of magnitude larger while the beam current is comparable. Our dose level and beam current are comparable to those used in recent studies in which graphene on SiO$_2$ was directly etched at the nanometer scale by using an e-beam at 3 keV to dissociate oxygen radicals from injected O$_2$ gas [2]. It was concluded that the dissociation was due to primary, backscattered, and secondary electrons. In these studies, dosages of 1.5–29 C/cm^2 and a beam current of 0.1 nA were used at a pressure of 2×10^{-3}

Torr, to give practical patterning speeds at acceptable e-beam scattering rates by the gas molecules.

After irradiation, we used Raman spectroscopy to determine the presence of graphene in the irradiated areas. The Raman system used was a Thermo Electron Almega XR with an excitation laser wavelength of 532 nm, spot size of 0.6 μm^2, laser power of 6 mW, and a spectral resolution of 2 cm^{-1}. It is well-known that monolayer graphene has a characteristic G peak at 1580 cm^{-1}, a sharp 2D peak at about 2700 cm^{-1}, and, if the graphene has defects, a D peak at about 1340 cm^{-1}. The D peak observed after e-beam irradiation has a fullwidth-at-half-maximum (FWHM) of about 30 cm^{-1} at dosages for which it is reversible [11], and
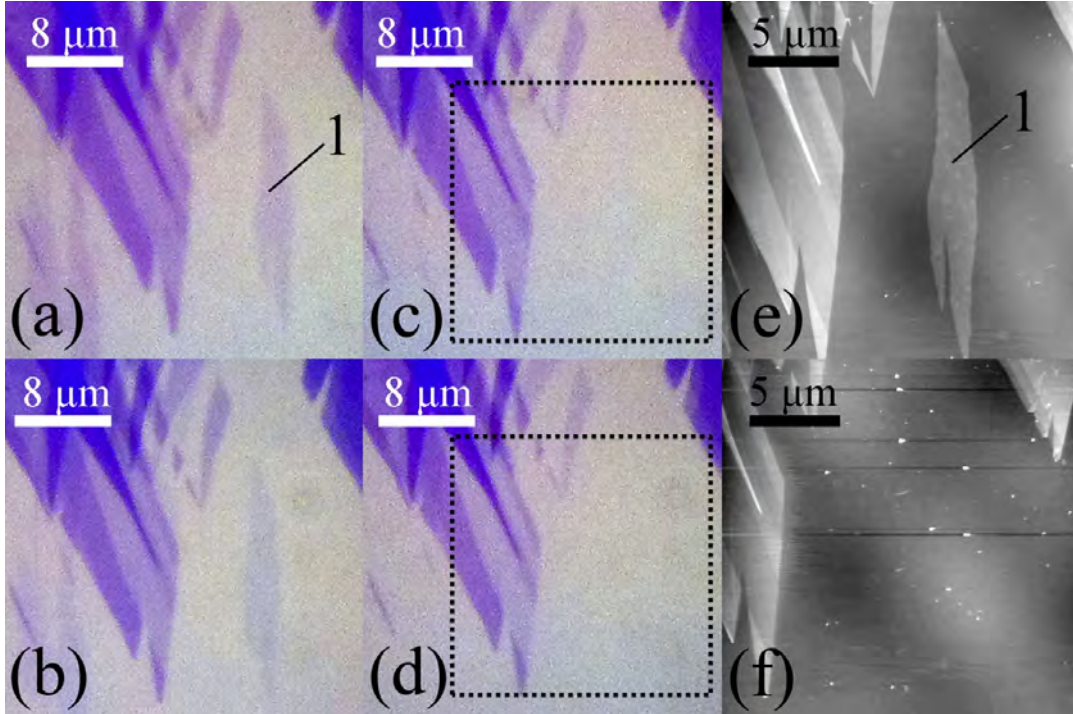
FIGURE 4.1. (a) Optical image of a monolayer graphene region indicated by the number 1. (b)-(d) Optical images after whole-sample irradiation using a plasma electron source at a dosage rate of 0.4 mA/cm^2 for a total of about 6, 12 and 15 min, resulting in dosages of 0.1, 0.3 and 0.4 C/cm^2, respectively. (e), (f) Atomic force microscopy images of the boxed regions in (c) and (d), respectively.

a FWHM of about 50 cm^{-1} for few-layer flakes that have been irreversibly thinned [13]. In contrast, carbon contamination deposited due to prolonged electron irradiation of SiO$_2$ at 15 keV and 0.3 nA has broad D and G bands with FWHMs greater than 100 cm^{-1} [22]. By inspecting the Raman spectra, we can determine the presence of graphene in an area and distinguish it from carbon contamination. We attribute this to the fact that lower energy primary electrons stay in the SiO$_2$ substrate near to the surface of the substrate and cause the most charging and defect formation. The higher energy 30 keV electrons penetrate deeper into the substrate and enter the conducting Si substrate that conducts them to ground, and so the 30 keV electrons do not cause as much damage to the substrate due to charging as the 1.5 or 10 keV electrons.

4.5. Results and Discussion

Figure 4.1 shows an example from a previous experiment involving the removal of a single monolayer exfoliated on SiO$_2$ using whole-sample irradiation from an electron source consisting of a He plasma, like the results in another paper [13]. The experimental set-up is described in detail in Ref. [12]. In Figure 4.1, the substrate had a bias of about +25 V relative to the chamber and an estimated electron dosage rate of 0.4 mA/cm^2 [13]. Figure 4.1 (a) shows the monolayer before irradiation, and Figure 4.1 (b)-(d) after a total of about 6, 12 and 15 min of irradiation, respectively, resulting in dosages of 0.1, 0.3 and 0.4 C/cm^2, respectively. Figure 4.1 (e) and (f) shows atomic force microscopy (AFM) images of the boxed regions in Figure 4.1 (c) and (d), respectively. Although the monolayer has thinned and is not optically visible in Figure 4.1 (c), it is still observable in the AFM image with well-defined edges. Finally, in Figure 4.1 (f) the monolayer completely disappears from the AFM image. Raman spectra taken after disappearance show no observable peaks associated with carbon, and multi-layer flakes are thinned uniformly across the flake [13]. At a substrate bias of +60 V and dosage rate of about 1 mA/cm^2, removal of at least 30 layers (10 nm) from a flake was observed in 30 min [13]. Using the same plasma system as in Ref. [13] at a substrate bias of +60 V and dosage rate of 1 mA/cm^2, we irradiated a 50 nm thick flake exfoliated on a conducting Si substrate for 20 min and observed no thinning using AFM. The Si substrate
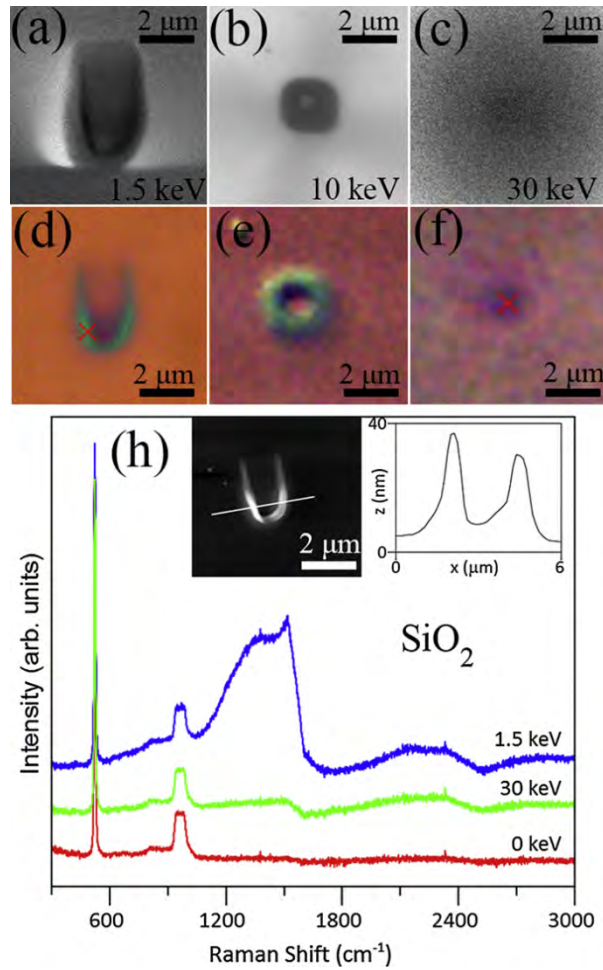
FIGURE 4.2. Scanning electron microscopy (SEM) images of distinct regions of bare SiO_2 after irradiation by (a) 1.5 keV, (b) 10 keV, and (c) 30 keV electron beam all with dosage of 28.8 C/cm^2. (d)-(f) Optical images corresponding to the area depicted in the SEM image directly above them. The crosses on (d) and (f) show the center of the Raman laser beam. (h) Raman spectra of the areas indicated by the crosses, where the 1.5 keV spectrum corresponds to the cross in (d), the 30 keV spectrum corresponds to the cross in (f), and the 0 keV spectrum was done on a region of uncovered SiO_2 without any irradiation. The inset on the left-hand-side of (h) shows an AFM image of the region shown in (d). The right-hand-side of the inset shows the height profile along the line drawn in the AFM image.

59

was obtained by removing the oxide from a Si sample using HF acid. These observations are consistent with those of Chen et al. [3] in which no etching was observed for thin carbon films deposited on Si and support the mechanism that oxygen in the substrate plays a role in thinning. To investigate the mechanism in more detail and determine if the etching occurs by incident electrons going through the graphene, we carried out e-beam experiments. We first irradiated uncovered areas of the SiO_2 substrate. Figure 4.2 (a)-(c) shows SEM images of SiO_2 after irradiation at 1.5, 10 and 30 keV, respectively. The dark and bright regions in the SEM images are due to charging and carbon contamination [23]. Charging occurs in dielectrics because of charge trapping at defects that are pre-existing or induced by the irradiation. Carbon contamination occurs because of dissociation of hydrocarbons in the chamber by the primary electrons or backscattered or secondary electrons emitted from the surface. Figure 4.2 (d)-(f) shows corresponding optical images of the irradiated areas. Figure 4.2 (h) shows Raman spectra obtained at the locations indicated by the crosses in Figure 4.2 (d) and (f), and an un-irradiated (0 keV) region of the SiO_2. The spectra are normalized so that their Raman Si peaks at 520 cm^{-1} have the same height. The optical images shown in Figure 4.2 (a) and (b) show that the irradiations at 1.5 and 10 keV produced U-shaped and circular features, respectively. It has been reported that e-beam irradiation can produce U-shaped and circular charged regions in a dielectric because of electromigration of charged defects that can lead to volume expansion and outgrowths on the surface [24, 25]. As shown in the AFM image in the inset in Figure 4.2 (h), the U-shaped feature has a height of about 30 nm.

We attribute these features to volume expansion of the SiO_2 and carbon contamination. As shown in Figure 4.2 (h), the Raman spectrum corresponding to the area irradiated at 1.5 keV shows two broad bands in the region from 1200 to 1600 cm^{-1}, and no observable 2D peak near 2700 cm^{-1}. We attribute the spectrum to carbon contamination, as is well-known [22]. As shown in Figure 4.2 (h), the Raman spectrum of the area irradiated at 30 keV shows significantly less carbon contamination. The optical image shown in Figure 4.2 (f) after 30 keV irradiation does not show Ushaped or circular features. We attribute this to the

greater penetration depth of 30 keV electrons that results in fewer electrons stopping within the 300 nm SiO_2 layer and producing defects. Using the Monte Carlo simulation software CASINO version 2.42 [26] that simulates electron trajectories in materials, we found the maximum Z values, Zmax, defined as the maximum of the distribution of the penetration depth of electrons. At 1.5, 10 and 30 keV, Zmax was about 38 ± 18 nm, 700 ± 350 nm, and 4000 ± 1600 nm, respectively. At 1.5 keV almost all the electrons stop within the SiO_2
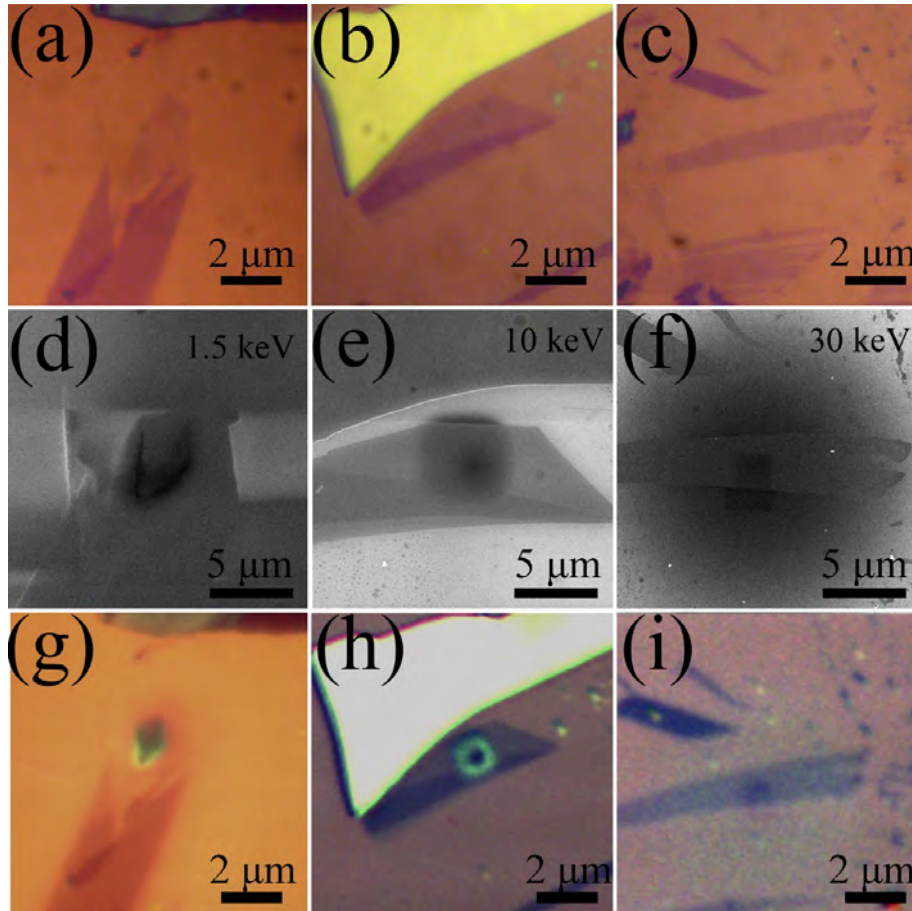
FIGURE 4.3. (a)-(c) Optical images of graphene monolayers before any irradiation. (d)-(f) Corresponding scanning electron microscopy images of the same monolayers after e-beam irradiation with energy (d) 1.5 keV, (e) 10 keV, and (f) 30 keV. All the images were taken after irradiation at a dosage of 28.8 C/cm^2 on a 2×2 μm^2 area. (g)-(i) Optical images corresponding to (d)-(f), respectively.

layer, at 10 keV the tail of the distribution is within the SiO_2, and at 30 keV almost none of the electrons stop in the SiO_2. Electrons that enter the conducting Si substrate do not produce charging effects. Figure 4.3 (a)-(c) shows optical images of monolayer regions before irradiation, and Figure 4.3 (d)-(f) shows the corresponding SEM images after irradiation at 1.5, 10 and 30 keV, respectively. The SEM images show contrast variations due to charging and contamination as in Figure 4.2. Figure 4.3 (g)-(i) shows the corresponding optical images after irradiation. Figure 4.3 (g) and (h) after 1.5 and 10 keV irradiation show similar U-shaped and circular features seen in Figure 4.2(d) and (e) and are attributed to the SiO_2 substrate.

Figure 4.4 shows a series of Raman spectra taken across the U-shaped region in Figure 4.3 (g) at the locations indicated by the crosses in the inset. The drawn line in the inset corresponds to the boundary between the monolayer and SiO_2. The spectrum labeled 1 in Figure 4.4 was taken at the left-most cross that is furthest from the monolayer. Figure 4.5 (a) shows a fit to this spectrum with two Lorentzian curves numbered 1 and 2 and located at 1346 cm^{-1} with a FWHM of 369 cm^{-1} and 1519 cm^{-1} with a FWHM of 115 cm^{-1}, respectively. We attribute these peaks to the D and G bands, respectively, of carbon contamination. As the Raman spectra are taken across the irradiated region (spectra numbered 2–12), sharp peaks develop superimposed on the broad D and G bands. Figure 4.5 (b) shows a fit to a spectrum in the series (number 9) with four Lorentzian curves numbered 1, 2, 3, and 4 located at 1325 cm^{-1} with a FWHM of 421 cm^{-1}, 1514 cm^{-1} with a FWHM of 115 cm^{-1}, 1344 cm^{-1} with a FWHM of 26.8 cm^{-1}, and 1592 cm^{-1} with a FWHM of 19.2 cm^{-1}, respectively. We attribute peaks 1 and 2 to the D and G bands of contamination, respectively, and peaks 3 and 4 to the sharp D and G peaks of irradiated graphene, respectively. There is also a 2D peak at about 2700 cm^{-1}. The spectrum labeled i in Figure 4.4 also indicates the presence of the sharp peaks, with less contamination. Therefore, we conclude that the monolayer was not removed by the irradiation and has carbon contamination on it. These findings are inconsistent with the mechanism proposed by Chen et al. [3] on how oxygen etch graphene. Although oxygen may play a role in the etching process, an alternative model on how this
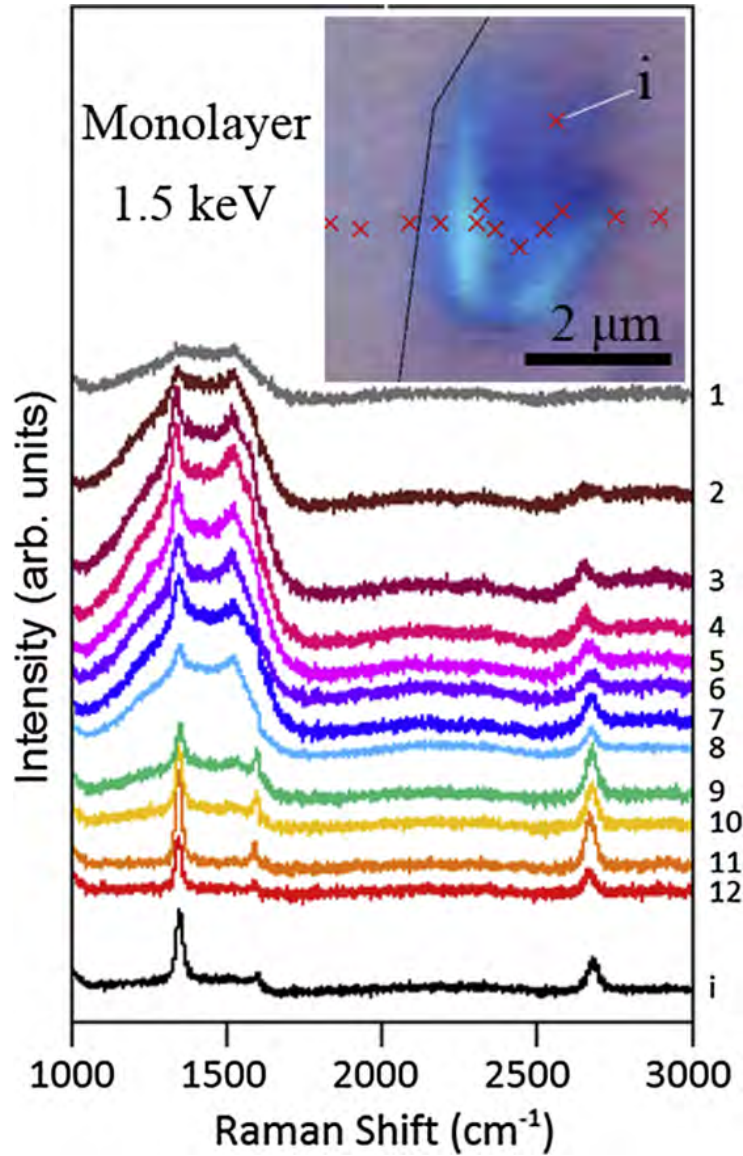
FIGURE 4.4. Raman spectra taken across the monolayer region irradiated at 1.5 keV shown in Figure 4.3 (g). The inset shows the locations where the Raman spectra was collected, with crosses denoting the center of the laser beam. The spectra are arranged from top to bottom (labeled 1–12) corresponding to the unlabeled crosses located from left to right in the inset. The cross labeled (i) in the inset corresponds to the spectrum labeled (i). The drawn line in the inset represents the boundary between the monolayer and substrate, where the area to the left of the line is SiO_2 and the area to the right is graphene.

occurs must be derived. One possibility involves the dissociation of oxygen from the large substrate surface surrounding the graphene sample and then migrating to the top surface of the graphene to etch it from above. Recombination of the oxygen into SiO_2 is prevented by the same mechanism (e-beam irradiation) that induces the dissociation. This would predict that a graphene sample that completely covers the SiO_2 would not etch excluding other oxygen sources.

This model is supported by experiments done with O_2 gas injected above exfoliated graphene on SiO_2 in an e-beam lithography system, where the O_2 gas was concluded to be dissociated into oxygen species by primary, backscattered and secondary electrons that induced etching of the graphene [2]. Figure 4.6 (a) and (b) shows optical images of the monolayer regions in Figure 4.3 (b) and (c), respectively, after irradiation at 10 and 30 keV. The crosses denote locations where Raman spectra were obtained. The optical image after 10 keV irradiation shows a circular feature as in Figure 4.2 (e) that is attributed to the SiO_2 substrate. The Raman spectra labeled 1–3 in Figure 4.6 (c) correspond to the crosses in Figure 4.6 (a) from left to right. The spectrum labeled 1 taken left-most from the irradiated region shows no observable contamination. The spectra labeled 2 and 3 taken in the irradiated region show sharp D and G peaks superimposed on broad D and G bands, indicating that the monolayer was not removed. The Raman spectrum for the area irradiated at 30 keV also shows sharp D and G peaks, with less contamination.

4.6. Conclusions

Focused e-beam irradiation at energies of 1.5, 10 and 30 keV at a dosage of 28.8 C/cm^2 of only monolayer areas exfoliated on SiO_2 did not result in removal of the irradiated areas. This finding is inconsistent with a previously reported mechanism in which incident electrons pass through the graphene and dissociate oxygen from the SiO_2 underneath causing etching of the graphene from below. This mechanism was proposed to explain etching of exfoliated graphene and thin carbon films on SiO_2 under wide-area irradiation. Our finding that graphene flakes exfoliated on Si do not show thinning under wide-area irradiation supports that oxygen in the substrate may play a role in thinning. We modify the previous mechanism
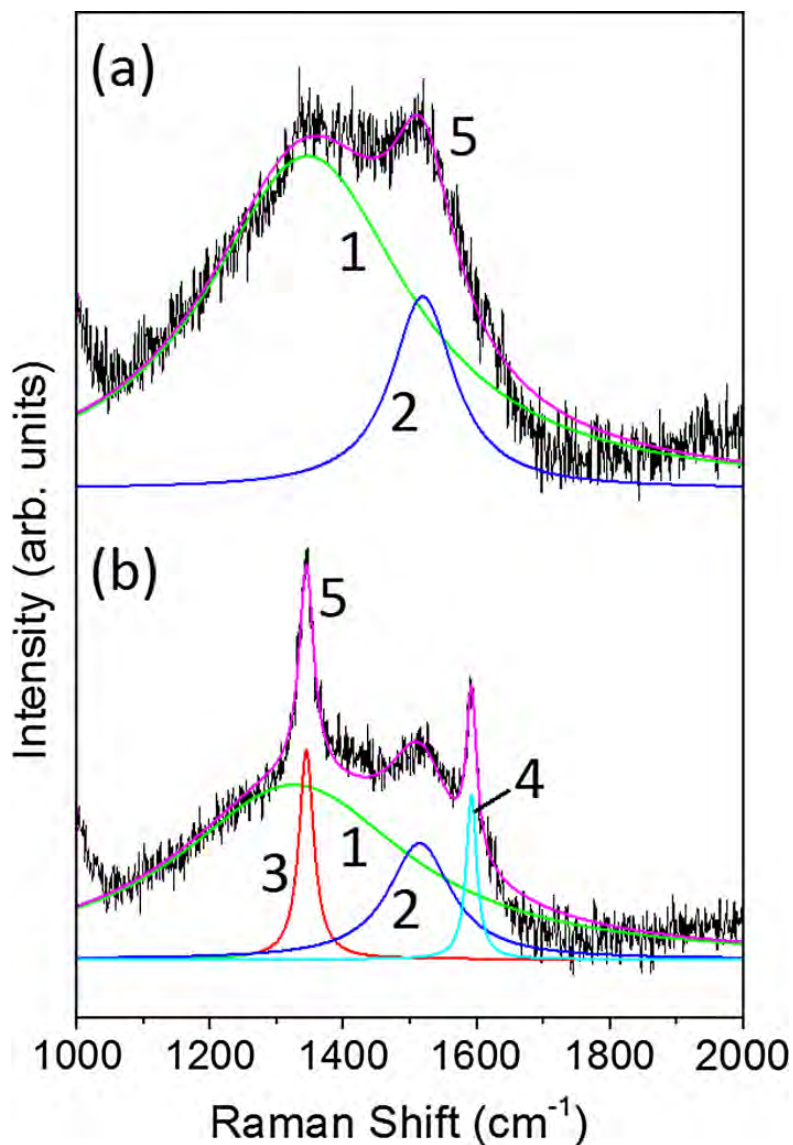
FIGURE 4.5. (a) Fit of Raman spectrum 1 from Figure 4.4 with two Lorentzian curves numbered 1 and 2 and located at 1346 cm^{-1} with a FWHM of 369 cm^{-1} and 1519 cm^{-1} with a FWHM of 115 cm^{-1}, respectively. (b) Fit of Raman spectrum 9 from Figure 4.4 with four Lorentzian curves numbered 1, 2, 3 and 4 located at 1325 cm^{-1} with a FWHM of 421 cm^{-1}, 1514 cm^{-1} with a FWHM of 115 cm^{-1}, 1344 cm^{-1} with a FWHM of 26.8 cm^{-1}, and 1592 cm^{-1} with a FWHM of 19.2 cm^{-1}, respectively. The fitted curves in (a) and (b) are numbered 5.
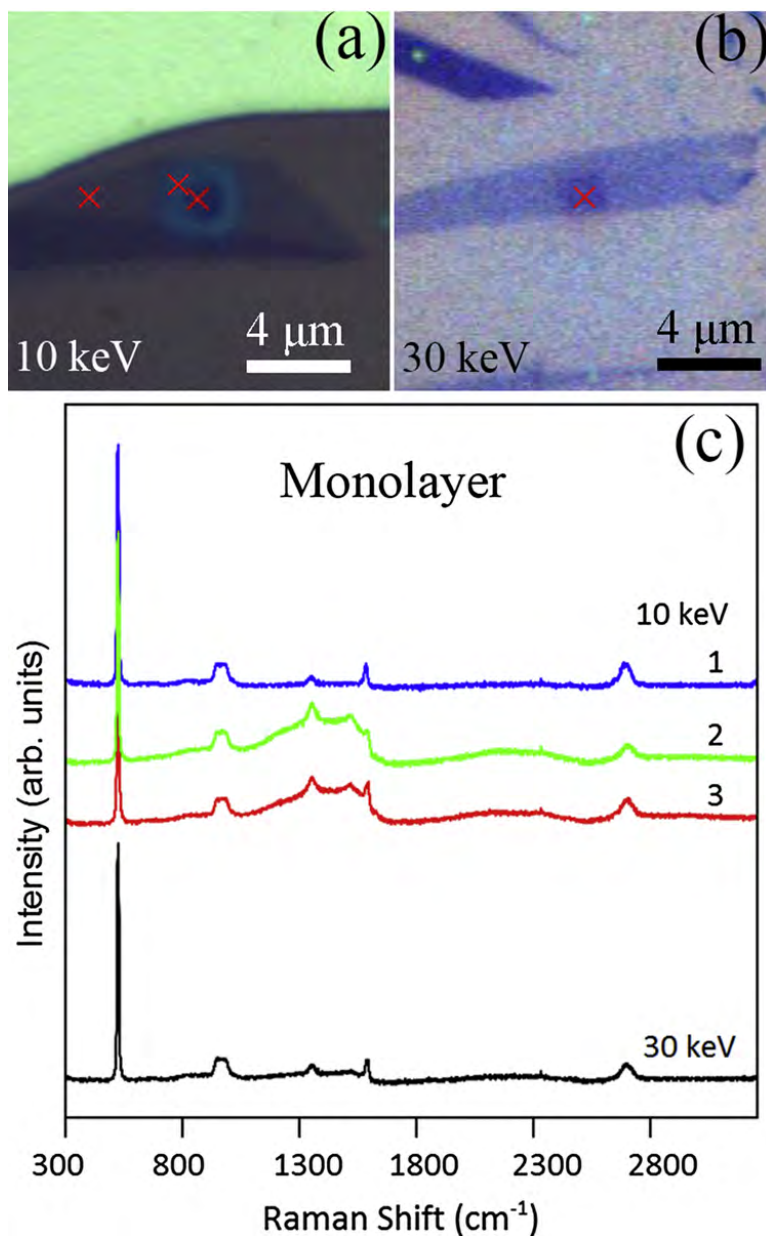
FIGURE 4.6. Optical images of the monolayer regions shown in Figure 4.3 (b) and (c) after irradiation by (a) 10 keV and (b) 30 keV electron beam, respectively. All the irradiations had a dosage of 28.8 C/cm². The crosses on (a) and (b) show the center of the Raman laser beam. (c) Raman spectra of the areas indicated by those crosses, where the numbers on the 10 keV spectrum represents the crosses on (a) going left to right.

by proposing that under wide-area irradiation, dissociated oxygen or neutral oxygen species from the uncovered SiO_2 substrate surrounding the graphene migrates to the top surface of the graphene and etches it from above. The larger surface area of the surrounding SiO_2 would provide a larger source of oxygen. Recombination of the oxygen into SiO_2 or other neutral species is prevented by the same e-beam irradiation that induces the dissociation. These results show that at a relatively high dosage and energies up to 30 keV, monolayer graphene is not removed. Even at incident energies of 1.5 and 10 keV that deposited considerable contamination and produced expansion of the SiO_2 substrate, monolayer graphene is not removed.

4.7. References

[1] Femi-Oyetoro, J.D., Yao, K., Roccapriore, K., Ecton, P.A., Tang, R., Jones, J.D., Verbeck, G. and Perez, J.M., 2019. Effects of high-dosage focused electron-beam irradiation at energies 30 keV on graphene on SiO_2. Applied Surface Science, 469, pp.325-330.

[2] Thiele, C., Felten, A., Echtermeyer, T.J., Ferrari, A.C., Casiraghi, C., Löhneysen, H.V. and Krupke, R., 2013. Electron-beam-induced direct etching of graphene. Carbon, 64, pp.84-91.

[3] C. Chen, C. Wang, D. Diao, Low energy electron irradiation induced carbon etching: triggering carbon film reacting with oxygen from SiO_2 substrate, Appl. Phys. Lett. 109 (5) (2016) 053104

[4] Stevens Kalceff, M.A., Thorogood, G.J., Short, K.T., 1999, Charge trapping and defect segregation in quartz, J. Appl. Phys. 86 (1) 205.

[5] Stevens-Kalceff, M.A., Electron-irradiation-induced radiolytic oxygen generation and microsegregation in silicon dioxide polymorphs, 2000, Phys. Rev. Lett. 84 (14) 3137.

[6] Lau, D., Hughes, A.E., Muster, T.H., Davis, T.J. and Glenn, A.M., 2010. Electron-beam-induced carbon contamination on silicon: Characterization using Raman spectroscopy and atomic force microscopy. Microscopy and Microanalysis, 16(1), pp.13-

20.

[7] S. Thomas J. Appl. Phys 45, (1974) 161

[8] O. L. Curtis Jr., J. R. Srour, K. Y. Chiu J. Appl. Phys. 45, (1974) 4506

[9] K.S. Novoselov, A.K. Geim, S. Morozov, D. Jiang, M. Katsnelson, I. Grigorieva, S. Dubonos, A.A. Firsov, Two-dimensional gas of massless Dirac fermions in graphene, Nature 438 (2005) 197.

[10] D. Teweldebrhan, A.A. Balandin, Modification of graphene properties due to electron-beam irradiation, Appl. Phys. Lett. 94 (1) (2009) 013101.

[11] J.D. Jones, P.A. Ecton, Y. Mo, J.M. Perez, Comment on "Modification of graphene properties due to electron-beam irradiation", [Appl. Phys. Lett. 94, 013101 (2009)], Appl. Phys. Lett. 95 (24) (2009) 013101.

[12] D. Jones, W.D. Hoffmann, A.V. Jesseph, C.J. Morris, G.F. Verbeck, J.M. Perez, On the mechanism for plasma hydrogenation of graphene, Appl. Phys. Lett. 97 (23) (2010) 233104.

[13] J.D. Jones, R.K. Shah, G.F. Verbeck, J.M. Perez, The removal of single layers from multi-layer graphene by low-energy electron stimulation, Small 8 (7) (2012) 1066.

[14] M. Xu, D. Fujita, N. Hanagata, Monitoring electron-beam irradiation effects on graphene by temporal Auger electron spectroscopy, Nanotechnology 21 (26) (2010) 265705.

[15] F. Banhart, Irradiation effects in carbon nanostructures, Rep. Prog. Phys. 62 (8) (1999) 1181.

[16] I. Childres, L. A. Jauregui, M. Foxe, J. Tian, R. Jalilian, I. Jovanovic, Y. P. Chen, Appl. Phys. Lett. 97 (2010) 173109.

[17] J.M. Michalik, S. Roddaro, L. Casado, M.R. Ibarra, J.M. de Teresa, Microelectron. Eng. 88 (2001) 2063.

[18] S. Hari, A.M. Goossens, L.M.K. Vandersypen, C.W. Hagen, Microelectronic Engineering 121 (2014) 122

[19] A.M. Lanzillotto, T.E. Madey, R.A. Baragiola, Negative-ion desorption from insu-

lators by electron excitation of core levels, Phys. Rev. Lett. 67 (2) (1991) 232.

[20] R.A. Baragiola, T.E. Madey, A.M. Lanzillotto, Multiply charged ions from electron bombardment of SiO_2, Phys. Rev. B 41 (13) (1990) 9541 21 Y.K. Koh, M.H. Bae, D.G. Cahill, E. Pop, Reliably counting atomic planes of fewlayer graphene (n ¿ 4), ACS Nano 5 (1) (2010) 269.

[21] D. Lau, A.E. Hughes, T.H. Muster, T.J. Davis, A.M. Glenn, Electron-beam-induced carbon contamination on silicon: characterization using Raman spectroscopy and atomic force microscopy, Microsc. Microanal. 16 (1) (2010) 13.

[22] M.T. Postek, A.E. Vladár, Does your SEM really tell the truth? How would you know? Part 4: Charging and its mitigation, Proc SPIE Int. Soc. Opt. Eng. 9636 (2015) 963605.

[23] M.A. Stevens Kalceff, G.J. Thorogood, K.T. Short, Charge trapping and defect segregation in quartz, J. Appl. Phys. 86 (1) (1999) 205.

[24] M.A. Stevens-Kalceff, Electron-irradiation-induced radiolytic oxygen generation and microsegregation in silicon dioxide polymorphs, Phys. Rev. Lett. 84 (14) (2000) 3137.

[25] D. Drouin, A.R. Couture, D. Joly, X. Tastet, V. Aimez, R. Gauvin, CASINO V2. 42-a fast and easy-to-use modeling tool for scanning electron microscopy and microanalysis users, Scan.: J. Scan. Microsc. 29 (3) (2007) 92.

CHAPTER 5

MECHANISM FOR ETCHING OF EXFOLIATED GRAPHENE ON SUBSTRATES BY
LOW-ENERGY ELECTRON IRRADIATION FROM HELIUM PLASMA ELECTRON
SOURCES [1]

5.1. Background

Chen et al. [1] proposed a mechanism for low-energy electron induced etching of thin amorphous carbon films and exfoliated multilayer graphene flakes on SiO_2/Si substrates. In their mechanism, electrons travel through the sample and reach the carbon/SiO_2 interface where they dissociate O atoms from the SiO_2 substrate. The O atoms then etch the carbon from below by reaction with C bonds that have been rearranged or damaged by the incident electrons as illustrated in Figure 5.1. In their letter, the authors observed etching at incident electron energies of 50-200 eV for amorphous carbon films 4-20 nm thick. They noted that incident electrons at these energies cannot reach the substrate since the electron mean free path is about 0.5-1.0 nm. Consequently, they considered that secondary electrons produced by the incident electrons are the ones that reach the substrate and cause O dissociation. They stated that the whole process could be more complicated. In this dissertation, we show that, at least for exfoliated multi-layer graphene flakes on SiO_2/Si substrates, their proposed mechanism appears to be incorrect. Using AFM, we show that the top surface of flakes that are about 55 nm (160 layers) thick exhibits etching on the order of that exhibited by thinner regions of the flake. In addition, the surfaces of such thick flakes exhibit features that are characteristic of etching. Given the practically zero diffusivity of O atoms perpendicular to graphene layers, these observations indicate that etching proceeds from the top surface of the flake downwards instead of upwards from the carbon/SiO_2 interface. We propose that the etching may be due to O atoms dissociated from bare regions of the SiO_2/Si substrate.

Chen et al. [1] do not state the coverage of the amorphous carbon films deposited on SiO_2/Si substrates. If any regions of the substrate were not covered with carbon film, or the underside of the substrate was not also covered, then O atoms may have dissociated from bare SiO_2 regions and the etching due to them instead of O atoms dissociated at the carbon/SiO_2 interface. In addition, extending this study to other technological important substrates (dielectric and conducting) helped to shed more light into the etching mechanism.

5.2. Abstract

The authors investigate the mechanism for etching of exfoliated graphene multilayers on SiO_2 by low-energy (50 eV) electron irradiation using He plasma systems for electron sources. A mechanism for this etching has been previously proposed in which the incident electrons traverse the graphene and dissociate oxygen from the SiO_2 substrate at the graphene/SiO_2 interface. The dissociated oxygen reacts with carbon defects formed by the electron irradiation and thereby etches the graphene from below. They study etching using graphene flakes of various thicknesses on SiO_2, low and higher resistivity Si, indium tin oxide (ITO), and silicon carbide (SiC). They find that thicker layer graphene on SiO_2 does not etch less than thinner layers, contrary to the previously proposed model. They find that etching does not occur on low-resistivity Si and ITO. Etching occurs on higher resistivity Si and SiC, although much less than on SiO_2. This is attributed to He ion sputtering and vacancy formation. From these observations, they propose that oxygen etches graphene from above rather than below. In addition, they propose He ions instead of incident electrons cause the defects that oxygen reacts with and etches.

5.3. Introduction

Graphene has attracted considerable interest due to its potential applications in electronics [2]. Etching is widely used in the fabrication of graphene device structures. We investigate the etching of exfoliated graphene on SiO_2 due to wide-area low-energy (LE) electron irradiation at 60 eV and dosages of about 0.7 C/cm^2. This type of etching has been reported when using electron sources based on plasma systems in which He gas is used
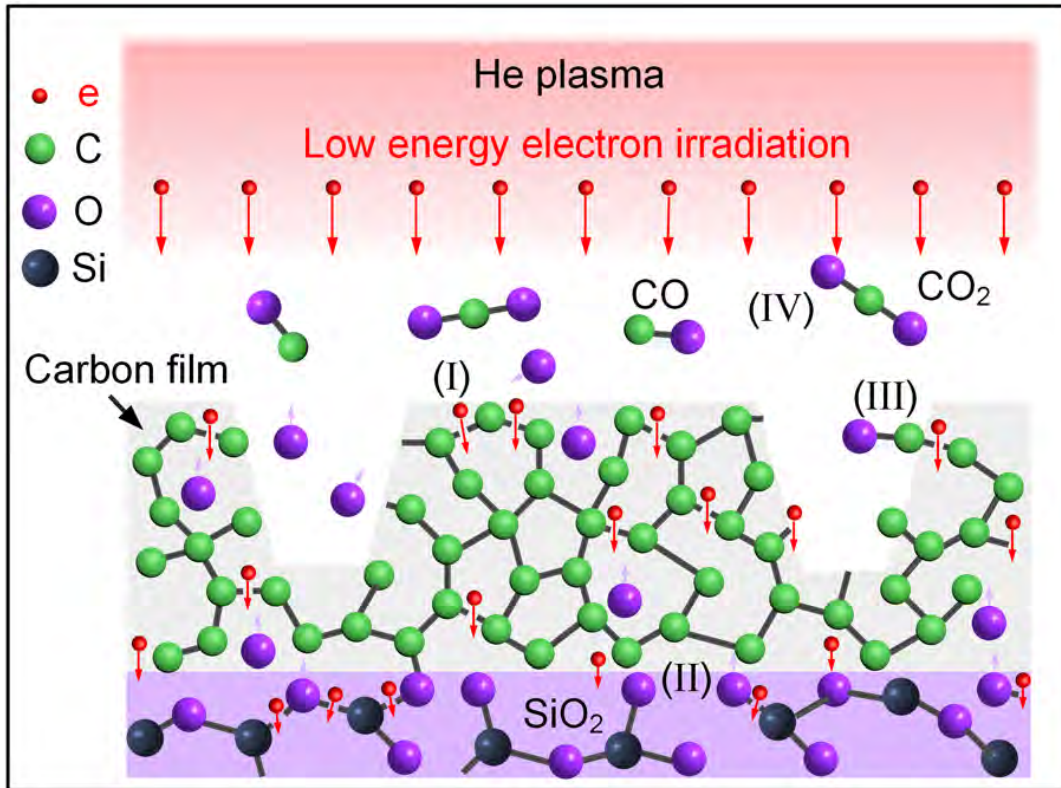
FIGURE 5.1. The mechanism of low-energy electron irradiation induced etching of the carbon film on the SiO_2 substrate. Under electron irradiation, carbon bonds are broken and carbon atoms are dissociated (step I). The electron irradiation breaks the Si–O bonds and creates mobile O atoms (step II). The mobile O atoms diffuse and react with the dissociated C atoms (step III). CO or CO_2 desorbs from the carbon surface (step IV). Reproduced from Chen, C., Wang, C. and Diao, D. Low energy electron irradiation induced carbon etching: Triggering carbon film reacting with oxygen from SiO_2 substrate. *Appl. Phys. Lett.*, **2016**, 109(5), 053104, with the permission of AIP Publishing.

[1]. A mechanism by which such etching occurs has been proposed in which the incident LE electrons travel through the graphene, dissociate oxygen from the SiO_2 substrate at the graphene/SiO_2 interface, and the dissociated oxygen etches the graphene from below [1]. However, details of the etching mechanism are not well known. Our objective is to better understand the mechanism by studying the effect of LE irradiation on other substrates such

as low- and high-resistivity Si, indium tin oxide (ITO), and silicon carbide (SiC). The effects of irradiation are studied using optical microscopy and atomic force microscopy (AFM). Our results provide new insights into the physical basis of the mechanism. Various methods have been reported for etching graphene such as reactive ion etching [3-5]. Choon-Ming et al. [3] studied the mechanisms of graphene fabrication that are induced by plasma for layer-by-layer thinning. They analyzed and compared several reported mechanisms using controlled parameters of various plasmas combined with sub-layer substrate effects. Based on their studies, they proposed an overview of plasma application as the basis of developing new approaches to achieve uniform graphene with the desired number of layers, and utilizing specific substrates to control excessive etching, for future graphene structures. Xie et al. [4] investigated the selective etching of graphene and graphene nanoribbon edges using hydrogen plasma. In their studies, they determined that an intermediate temperature of ≈ 300 °C for the hydrogen plasma reaction is necessary to avoid defects in the basal plane. However, defects are observable at low and high temperatures.

Other techniques have also been developed to etch multilayer graphene one layer at a time, such as mild nitrogen plasma irradiation. Yang et al. [6] used mild nitrogen plasma irradiation and reported that the process created defects in the top-layer graphene. It was observed that annealing in Ar/H_2 removed the defects, leaving the underneath layer unaffected. Al-Mumen et al. [7] used oxygen plasma to control the number of graphene layers etched. They reported that oxygen plasma at the ground electrodes produced significantly lower defects to the bottom graphene layer as compared to oxygen reactive ion etching using powered electrodes. Lim Woong Sun et al. [8] used sequential oxidation to study the atomic layer etching of graphene for device fabrication. Although, an increase of the D peak of the graphene was observed, which suggest defects, they were able to recover the structure with acceptable electrical characteristics through hydrogen annealing. Han et al. [9] obtained a monolayer graphene from thinning few graphene layers on an SiO_2/Si substrate using laser irradiation. They observed top graphene layers were etched completely while the monolayer graphene remained unetched. They explained that heat accumulation played a major role

on the upper graphene layers, because of light absorption. Also, SiO_2/Si substrate served as a heat sink preventing the monolayer graphene from etching. Fischbein et al. [10] employed focused high-energy electron-beam irradiation. They demonstrated that suspended graphene sheets can be manageably nanosculpted into nanopores and nanobridges with high spatial resolution. The exposure was done with a focused electron beam of a transmission electron microscope. They concluded that this technique would offer a route to fabricating graphene structures.

Lemme et al. [11] used helium ion beam to etch suspended and unsuspended graphene into devices with an in situ electrical measurement system during the lithography process. They showed that helium ion etching could be considered an alternative nanofabrication method for graphene devices in the minimum feature sizes of 10 nm. However, they observed contaminations issues for the unsuspended graphene on SiO_2 substrates. The etching process can be used to nanostructure and electrically isolate different regions in a graphene device. Evidently, beams have been used for direct etching of graphene in which etching occurs due to knock-on collisions. The threshold electron energy for knock-on collision in graphene is about 86 keV. Banhart et al. [12] reviewed atom displacements by knock-on collisions on graphene. They determined that the threshold electron energy necessary for momentum transfer through knock-on collision is about 86 keV and thus, the energies at which LE electron irradiation etching occurs (50–200 eV) are below this threshold. Of particular interest is the studies done by Chen et al. [1]. They demonstrated that etching occurs during LE electron irradiation due to dissociation of oxygen from the SiO_2. They performed electron irradiation experiments on graphene and amorphous carbon films on Si and SiO_2 respectively, using electron sources from a mirror-confinement cyclotron resonance plasma system. The aim is to provide the mechanism of carbon films and graphene etching on SiO_2 substrate, to determine if the substrate was a precursor for etching. In more detail, they used carbon films of thickness 4-20 nm and graphene of up to 13 layers. They observed that carbon films of thicknesses 4 and 8 nm decreased monotonically with irradiation energy. For thicknesses of 12 and 20 nm, there was no observed changes at 50 eV. Though, at subsequent

energies, etching was directly dependent on the film thickness.

However, we note that in our experiments, thicker layer graphene on SiO_2 do not etch lesser than thinner layers. After irradiation experiments, Chen et al. [1] further corroborated that etch pits were observed, and the G band from Raman spectroscopy disappeared indicating an etching has occurred. In addition, the appearance of a D band signified defects after the irradiation. They explained their etching mechanism as an inelastic scattering process, in which electrons transfer their energy to the carbon atom at the sample surface. The carbon atoms can break by electronic excitation. They proposed that the incoming electrons can penetrate the SiO_2 substrate and break the Si-O bonds, where the SiO_2 serves as a precursor. After the bonds are broken, oxygen atoms become mobile and react with the initial dissociated carbon atoms forming CO or CO_2. They finally concluded that the etching mechanism depends on the SiO_2 precursor, film thickness and electron irradiation energy.

It is known that an LE electron can excite bonds within a molecule such as SiO_2 to antibonding or nonbonding states, causing dissociation at thresholds of 15–20 eV. Knotek and Feibelman [13] studied the electron-stimulated desorption on certain oxides such as SiO_2. The incident beam excites a bonding electron to an antibonding or nonbonding state, and atom can desorb as a result of an effective potential between surface atom and solid being repulsive. In their model, a core electron must be excited to trigger desorption, leading to a bonding-site-dependent threshold energy. In Ref. [1], it was proposed that the incident electrons transverse the graphene layers, and the dissociated oxygen atoms etch the graphene by reacting with the carbon bonds that have been damaged by incident electrons. Etching of exfoliated graphene flakes consisting of up to about 13 layers was observed at electron energies of 50 eV and dosages of about 30 C/cm^2, which was deposited over a period of 30 minutes.

In addition, etching of amorphous carbon films 4–20 nm thick deposited on SiO_2 was also reported at incident electron energies of 200 eV and similar dosages as described above. It was also reported that amorphous carbon films exhibited etching on SiO_2 but not
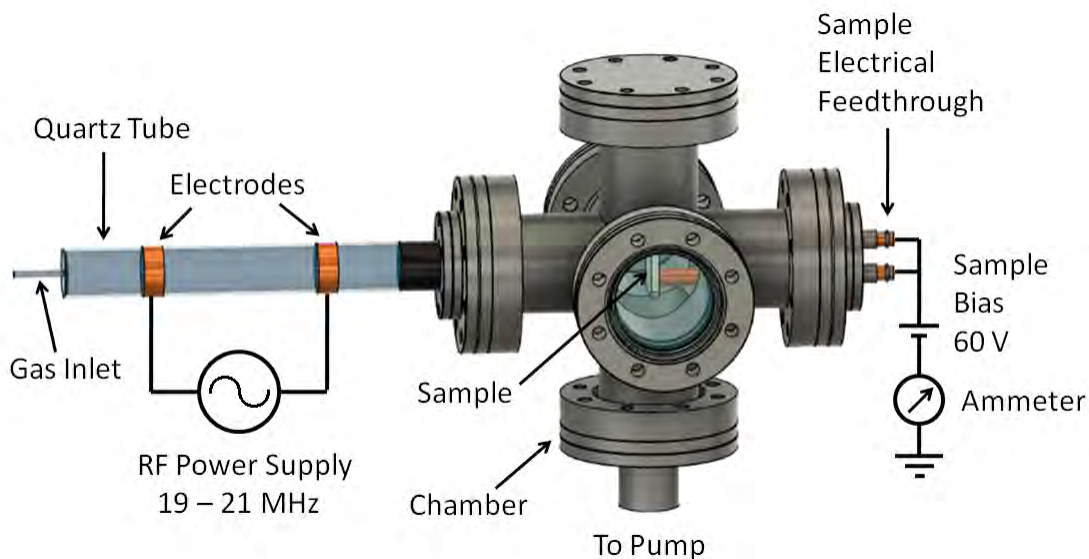
FIGURE 5.2. Sketch of experimental setup, not drawn to scale. The plasma is ignited within the quartz tube by a 50 W power supply capacitively coupled by two copper electrodes outside the tube. The sample is placed at a working distance of about 20 cm from the center of the excitation region between the electrodes. The electrode spacing is about 10 cm. The sample is biased at +60 V to attract electrons from the plasma, and the current is measured by the ammeter.

Si substrates, and thus it was concluded that oxygen desorption from an oxygen containing substrate was required for etching to occur on carbon films and exfoliated graphene. We note, however, that electron irradiation of electrically isolated graphene flakes on dielectric substrates can result in negative charging of graphene flakes because of the low emitted secondary and backscattered electron yields from graphene and carbon films, as discussed below. Negative sample charging can result in the attraction of He$^+$ ions onto the surface, and such an ion bombardment may produce defects that play a role in the etching.

Interestingly, in a paper by Lehtinen et al. [14] numerical calculations are reported that show that He ion bombardment of graphene sheets causes the greatest amount of single vacancy defects and sputtering at low energies of around 30–80 eV. Defect formation by

He ion bombardment proceeds by momentum transfer and in-plane recoil of carbon atoms. Therefore, it is of interest to study the etching mechanism in more detail.

5.4. Experiment

Our experimental setup and procedures are described in detail in Refs. [15] and [16]. A sketch of the system is shown in Figure 5.2. Samples are mechanically exfoliated from highly oriented-pyrolytic graphite using the scotch tape method. A remote RF capacitively coupled plasma system with He gas at a pressure of 50 mTorr is used to generate the electrons [15, 16]. The substrate is biased at +60 V attracting incident electrons at energies of about 60 eV [16]. We previously used this system to report the removal of single layers from exfoliated graphene by LE electron irradiation [15]. Chen et al. [1] used a mirror-confinement electron cyclotron resonance plasma system with He gas at 1.5×10^{-4} Torr to generate electrons at 50 eV. They state that He gas was used as the working gas to avoid the effect of ion impact on the carbon surface [1]. Helium ions would be formed as a result of electrons impacting He gas atoms. The use of plasma electron sources was necessitated by the need to expose the samples to high electron dosages on the order of 1–30 C/cm^2 during a reasonable exposure period of about 30 min.

The SiO$_2$ substrate was thermally grown to a thickness of 300 nm on a 500 μm thick Si (100) wafer with a resistivity of 0.01–0.02 Ωcm. The low-resistivity Si substrate was obtained from a 250 μm thick n-type Si (100) wafer with a resistivity of < 0.005 Ωcm. The higher resistivity Si sample was obtained from an Si wafer with a resistivity of about 10 Ωcm. The native oxides of the wafers were removed by dipping them in a solution of HF acid. The electron irradiation experiments were carried out shortly after oxide removal. During this time, oxide layers of about 2–4 Å are estimated to have grown on the Si [17]. The ITO was sputtered to a thickness of 100 nm from a bulk piece of 90% In$_2$O$_3$ and 10% SnO$_2$ (90/10) ITO onto a substrate consisting of a 10 nm thick Al$_2$O$_3$ film sputtered onto a low-resistivity 250 μm thick Si substrate. The SiC was obtained from Thin Film Devices, Inc. [18] and was 300 nm thick and deposited on an Si substrate.

5.5. Results and Discussion

Figure 5.3 (a) shows an optical image of an exfoliated flake on 300 nm SiO_2 on Si containing regions of various thicknesses. As is known for this oxide thickness, few-layer graphene appears light purple due to interference effects, while successively thicker regions appear darker, and totally reflecting regions appear yellow. Figure 5.3 (b) shows an optical image of the flake after exposure for 10 min at a substrate bias of +60 V and a dosage of about 0.7 C/cm^2. After exposure, the few-layer regions have disappeared, and the intermediate regions appear lighter. Figures 5.3 (c) and 5.3 (d) show AFM images taken before and after the exposure, respectively. Figure 5.3 (e) shows a height versus distance plot before (i) and after (ii) exposure taken along the line drawn in Figure 5.3 (d). As shown in Figure 5.3 (e), before exposure, the bright (yellow) and adjacent dark (purple) regions have heights of about 55 and 15 nm, respectively. After exposure, the bright (yellow) and dark (purple) regions have decreased in height to about 40 and 5 nm, respectively. Figure 5.3 (f) shows a higher resolution AFM image of the 40 nm thick region after exposure showing wide round features on the surface that are characteristic of etching.

We note that since the mean free path of electrons at 60 eV is about 0.48 nm [19], one would expect significantly more electrons to reach the graphene/SiO_2 interface under the 15 nm thick region than under the 55 nm thick region. If the etching were due to oxygen atoms dissociated at the graphene/SiO_2 interface, as in the model proposed in Ref. [1], then more etching should occur for the 15 nm region than the 55 nm region. However, the 15 nm thick region etches by 10 nm, while the 55 nm region etches by 15 nm. Secondly, from the wide, round features observed in the AFM images, etching appears to have occurred on top of the flake. If the etching were due to oxygen atoms dissociated from underneath the flake, then the oxygen would have to diffuse 55 nm through the graphene to reach the top surface. However, theoretical studies have shown that oxygen atoms do not diffuse normal to the graphene surface and react at defect sites [20], and exfoliated graphene is relatively defect-free. Therefore, these results support that etching occurs from above the sample instead of the graphene/SiO_2 interface. If oxygen plays a role in etching, then we propose that it
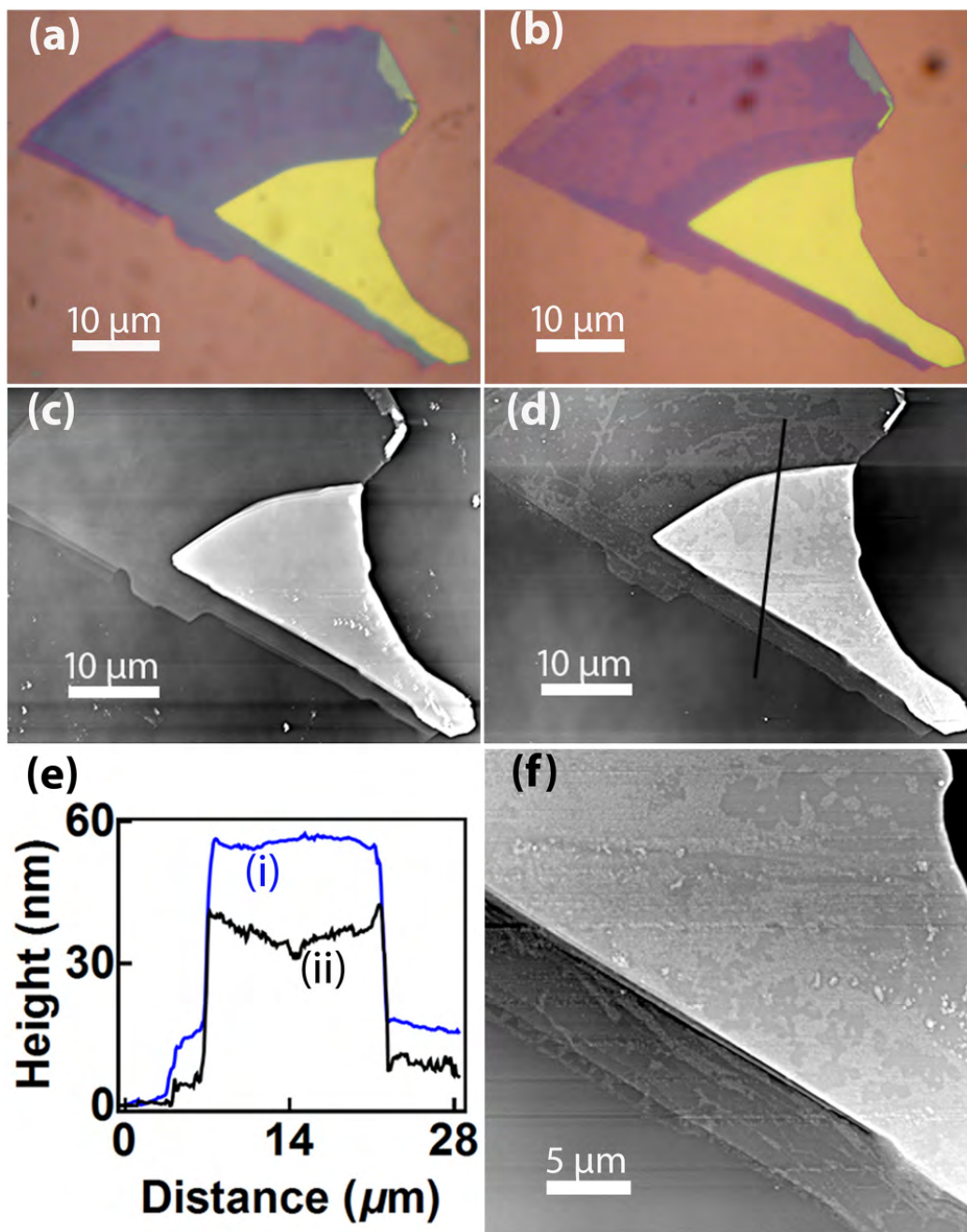
FIGURE 5.3. Optical images of a graphene flake on SiO_2 (a) before and (b) after 10 min of electron exposure to a dosage of 0.7 C/cm^2. (c) and (d) AFM images before and after exposure, respectively. (e) Height profiles of the graphene flake before and after the exposure along the line drawn in (d). (f) AFM image of the thick bright (yellow) region from (d).

mainly dissociates from the surrounding SiO_2 substrate, diffuses to the exfoliated graphene, and etches it from above. We do not know why the sample in Figure 5.3 preferentially etches at the center of the flake. It may be due to diffusion or charging effects. However, the preferential etching at the center is a small effect.

We then irradiated an exfoliated flake on the low resistivity Si substrate to test the oxygen dissociation hypothesis. Figure 5.4 (a) shows an AFM image of a graphene flake before any irradiation. The height of this flake is about 60 nm as shown by Figure 5.4 (d), which is comparable to the thick flake on SiO_2 discussed previously in Figure 5.3. Figure 5.4 (b) shows an AFM image of the same flake after 10 min of exposure under the same irradiation conditions as those of Figure 5.3. Figure 5.4 (c) is another AFM image of the same flake after an additional 10 min of exposure under the same conditions as before, bringing the total exposure time of the sample to 20 min. Figure 5.4 (d) shows the height profiles of the three AFM images all taken along the line scan indicated by the line drawn in Figure 5.4 (a). These height profiles are horizontally displaced for clarity, and they show no observable differences in height, indicating that the thick flake of graphene has not etched. We further corroborated our results by measuring a thin flake of graphene on a different area of the same substrate containing the thick graphene flake in Figure 5.4. Figure 5.5 (a) is an AFM image of a 13 nm graphene flake before irradiation, with a height comparable to the thin graphene sample on the SiO_2 substrate shown in Figure 5.3. Figure 5.5 (b) is an AFM image of the same thin flake after 10 min of irradiation. Figure 5.5 (c) is an AFM image of the same sample after an additional 10 min of exposure. The height profiles of all three AFM images along the line in Figure 5.5 (a) are superimposed and shown in Figure 5.5 (d). As with Figure 5.4 (d), these lines are displaced horizontally for clarity. The height of the graphene flake remains at approximately 13 nm despite the 10 and 20 min of irradiation, indicating that thin samples on low-resistivity Si also do not etch. Chen et al. [1] concluded that the oxygen for etching comes from the SiO_2 and not from O_2 or H_2O gases in the chamber or adsorbates on the sample surface based on their observation that thin carbon films etch when deposited on SiO_2 but do not etch when deposited on Si. Our results

that exfoliated graphene etches on SiO_2 but does not etch on low-resistivity Si support the conclusion that the oxygen comes from the SiO_2.

In addition, Chen et al. [1] annealed the samples before irradiation at 400 °C for 30 min in the chamber under flowing He gas to remove H_2O adsorbates or any possible contamination on the sample surfaces. In Ref. [15], we reported etching of exfoliated graphene on SiO_2 by LE electron irradiation in which the samples were preheated in situ at a pressure of 1×10^{-5} Torr for 1 h at a temperature of 400 °C before irradiation. As discussed in Ref. [15], it has been reported that heating multilayer graphene at 150 °C desorbs H_2O, CO_2, and N_2 and heating at 200 °C desorbs O_2. These experiments also support that oxygen does not come from preadsorbed molecules on the sample surface.

However, these results do not exclude the possibility that the conductivity of the substrate plays a role in the etching. As previously mentioned, electrically isolated graphene flakes on a dielectric material such as SiO_2, when irradiated by electrons, tend to charge negatively, which may lead to He^+ ion bombardment. It was not possible to measure the charging of the substrate. However, the charging can be inferred from the total emitted electron yield. The charging of a sample is determined by the total emitted electron yield $(\delta + \eta)$, where δ is the secondary electron yield and η is the backscattered electron yield. If $(\delta + \eta) > 1$, the sample charges positively, and if $(\delta + \eta) < 1$, the sample charges negatively. For 10 nm thick SiO_2/Si and incident electrons of about 50 eV, δ is about 1.5, and so SiO_2 would charge positively [21]. However, graphene has been measured to have an ultralow δ of around 0.10 [22]. The backscattered yield, η, increases with atomic weight and for a low atomic weight atom such as C is about 0.1 [23]. Thus, we propose that graphene would charge negatively with respect to the surrounding substrate if irradiated with electrons and electrically isolated on a dielectric substrate. We note that when $(\delta + \eta) < 1$ and negative charging occurs, samples can charge to as much as the primary electron beam potential [24]. The negative charge on the graphene would attract the He^+ ions, the main He ion species. As discussed previously, He^+ ion bombardment causes the greatest number of defects and sputtering at low energies [14]. Thus, the defects that are necessary for etching to occur may
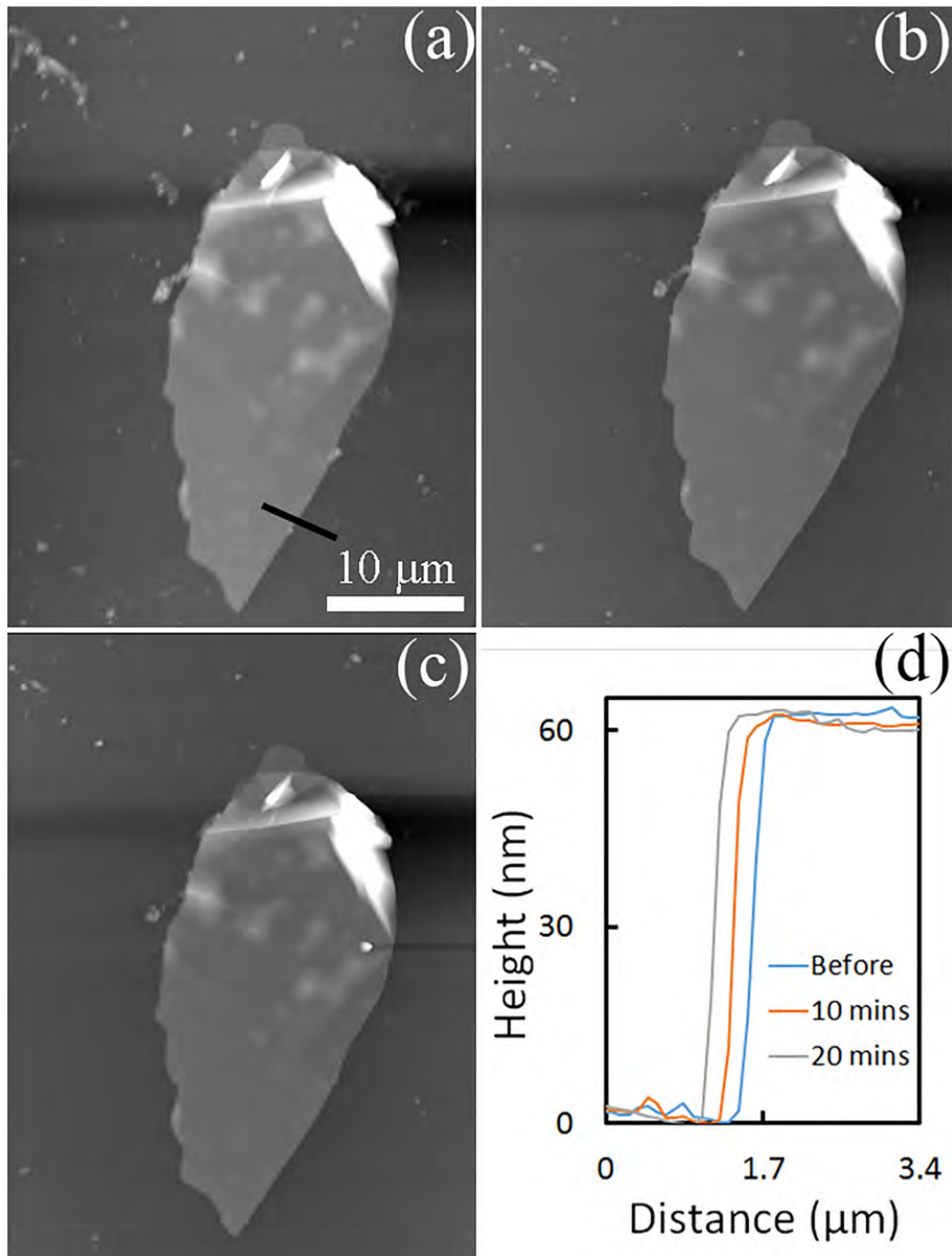
FIGURE 5.4. AFM images of a thick graphene flake on low-resistivity Si (a) before, (b) after 10 min, and (c) after 20 min of exposure. (d) Height profiles of the flake before irradiation, after 10 min, and after 20 min of exposure along the black line drawn on (a). The scale bar in (a) is the scale for images (a)–(c).

be produced by the He ions instead of the incident electrons. We note that in Ref. [1], it was reported that amorphous carbon films up to 20 nm in thickness on SiO_2 also etched under LE electron irradiation at 50–200 eV. This phenomenon was not well understood since the mean free path of electrons is on the order of 0.48 nm [19], as previously discussed.

Amorphous carbon films also have a low secondary electron yield of about 0.65–0.9 for freshly made samples in this energy range [25]. We propose the He^+ ion bombardment may
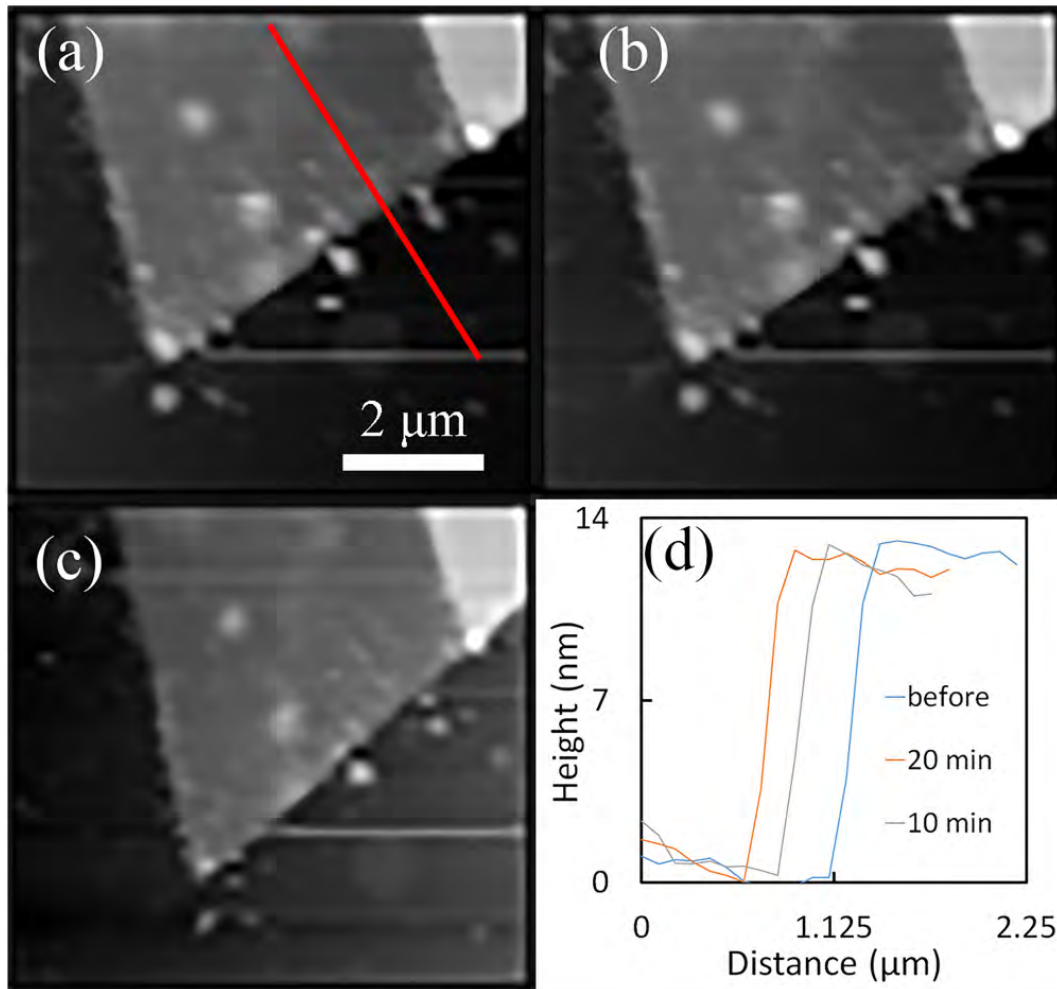
FIGURE 5.5. AFM images of a thin graphene flake on low-resistivity Si (a) before irradiation, (b) after 10 min, and (c) after 20 min of exposure. (d) Height profiles of the flake before irradiation, after 10 min, and after 20 min of exposure along the red line drawn on (a). The scale bar on (a) is the scale for images (a)–(c).

be responsible for the etching. To test this hypothesis, we tested if the presence of oxygen in a conducting substrate would induce etching. On a conducting substrate, graphene would
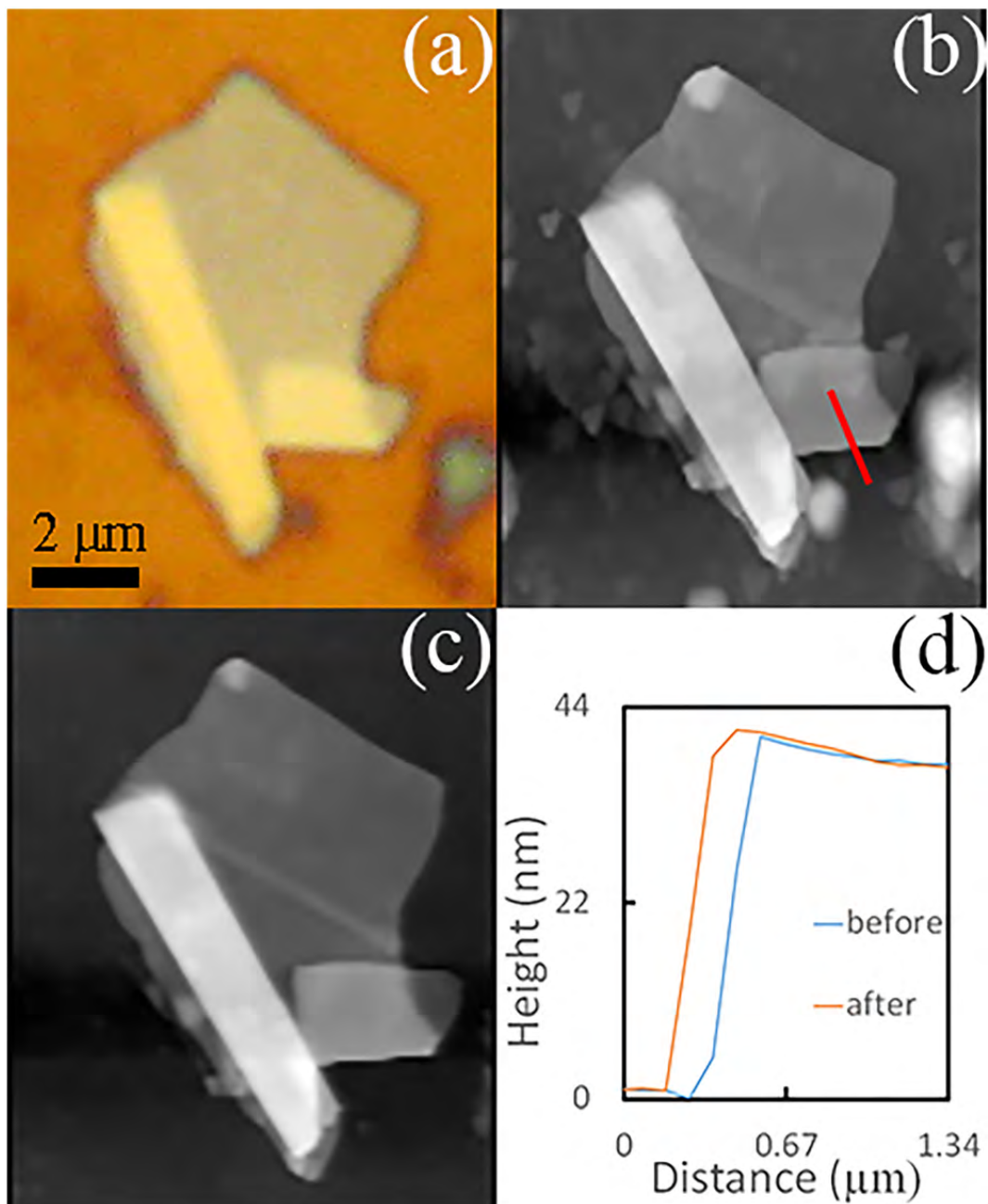
FIGURE 5.6. (a) Optical image of a thick graphene flake on ITO. (b) and (c) AFM images of the flake before and after 10 min of irradiation, respectively. (d) Height profiles for the flake before and after irradiation along the red line drawn on (b). The scale bar on (a) is the scale for images (a)–(c).
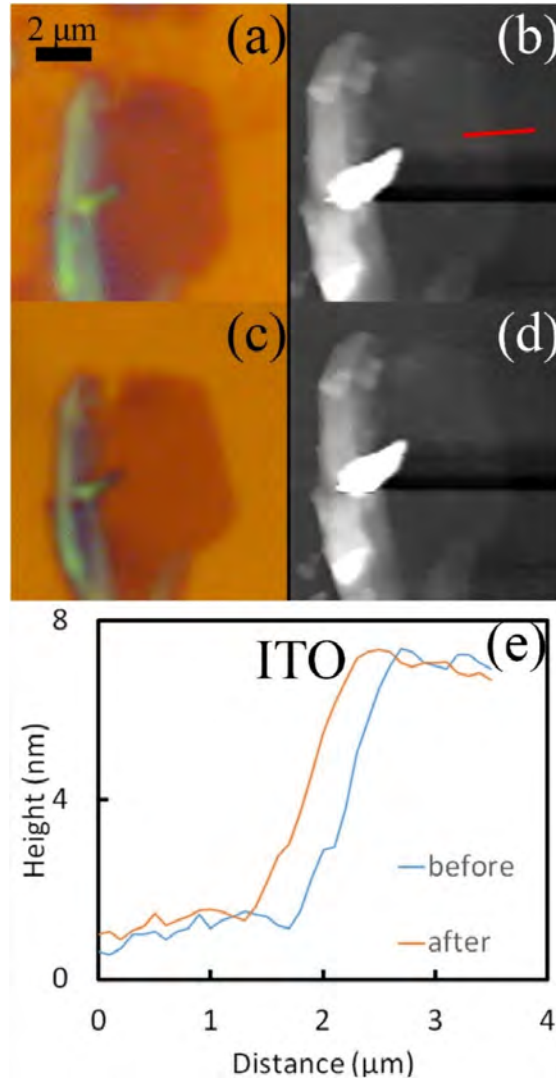
FIGURE 5.7. (a) Optical image of a thin graphene flake on ITO and (b) the corresponding AFM image. (c) Optical image of the same flake after 10 min of irradiation and (d) the corresponding AFM image. (e) Height profiles for the flake before and after irradiation along the red line drawn on (b). The scale bar on (a) is the scale for images (a)–(d).

not be electrically isolated and would not build up a negative charge. For that, we irradiated graphene exfoliated on an ITO substrate. We expect oxygen to be dissociated from the ITO by the mechanism discussed previously [13]. Additionally, it has been reported that oxides with a cation and anion Pauling electronegativity difference of > 1.7 are highly susceptible to

O^+ dissociation and desorption due to LE electron beam irradiation [13, 26]. This criterion is met by a variety of materials including SiO_2 and Al_2O_3 [13, 26]. ITO is a mixture of In_2O_3, which has an electronegativity difference of 1.8, and SnO_2, which has an electronegativity difference of 1.7, and thus also satisfies this criterion. Figure 5.6 (a) is an optical image of a graphene flake on ITO before electron beam irradiation, and Figure 5.6 (b) is the corresponding AFM image. Figure 5.6 (c) is an AFM image of the same flake after 10 min under irradiation at the same conditions as all the previous exposures. Finally, Figure 5.6 (d) shows the height profiles of both the AFM images denoted by the line in Figure 5.6 (b). As in the previous figures, the height profile lines are displaced horizontally for clarity.

The heights before and after the irradiation are the same, which indicates that exfoliated graphene on ITO did not etch. We also collected data for a thin area of graphene on ITO, with Figures 5.7 (a) and 5.7 (b) showing an optical and AFM image of a 7 nm thick flake, respectively. Figures 5.7 (c) and 5.7 (d) show optical and AFM images, respectively, of the flake after 10 min of irradiation. Figure 5.7 (e) superimposes the heights of the flake taken along the line from Figure 5.7 (b) before and after the irradiation and is displaced horizontally for clarity. The heights for both the AFM images are the same, and so it is concluded that thin graphene also does not etch on ITO. In the ITO experiment, any excess electrons on the graphene flake are conducted through the substrate and exit to ground, failing to build a negative charge on the graphene. As a result, there would be no He^+ ion bombardment. The oxygen that we expect to be dissociated fails to react with and etch the multilayer graphene in the same magnitude as we see for the SiO_2 substrate. Therefore, we conclude that oxygen and defects caused by the electron irradiation may not necessarily catalyze the etching of graphene. Additionally, it seems that the conductivity of the substrate may play a role in the mechanism; specifically, conducting substrates, regardless of the availability of oxygen, do not cause etching of exfoliated graphene. We believe that this is so because graphene on conducting substrates only experiences LE electron irradiation, and any defects that LE electrons produce in the graphene are not etched by oxygen. We propose that only when He^+ ions are accelerated due to the negative charge buildup in graphene on

dielectric substrates will the proper defects form that allow oxygen to etch the graphene. This proposition is consistent with our experiments as graphene on SiO_2 experiences ion bombardment and oxygen dissociates from SiO_2 and therefore etches graphene, but low resistivity Si and ITO do not etch because there is no charge buildup in the graphene and therefore no ion bombardment.

The final two substrates we irradiated aim to provide instances where electrically isolated graphene on a substrate without oxygen will etch. For this purpose, we used SiC, a dielectric material without any oxygen, and higher resistivity Si, which will provide insights into the effect of substrate resistivity on etching. For both the samples, only thin graphene flakes were analyzed as it is easier to see height changes. One may speculate that thin graphene flakes on any substrate would etch, but our results from the low-resistivity Si in which the thinner pieces did not etch show otherwise. Figure 5.8 (a) is an optical image of the graphene flake on SiC before irradiation. We note that few-layered graphene flakes exfoliated on SiC are light shades of green, and thicker flakes have a darker color of green. Figure 5.8 (b) is the AFM image corresponding to the graphene sample from Figure 5.8 (a). Figure 5.8 (c) is an optical image of the same graphene flake shown in Figure 5.8 (a) after 10 min of electron beam irradiation under the same conditions as all the previous exposures. It is noted that the color of the graphene flake is of a slightly lighter shade of green than that of Figure 5.8 (a). Figure 5.8 (d) is another optical image of the flake after an additional 10 min of irradiation. The color of the graphene sample appears to be of an even lighter shade of green. Figure 5.8 (e) is an AFM image of the flake after the combined 20 min of irradiation, corresponding to the graphene flake from Figure 5.8 (d). Figure 5.8 (f) shows the height profiles along the line in the AFM image shown in Figure 5.8 (b). We believe that the ridge on the border of the graphene sample is either polymer from the tape or a wrinkle in the graphene. However, the inner region is ascribed to graphene. The height profile for the flat graphene in the inner region of the sample before irradiation is 2–4 nm higher than the height profile for the region after 20 min of irradiation, indicating that LE electron irradiation on SiC etches exfoliated graphene, albeit not nearly as much as SiO_2. Therefore,
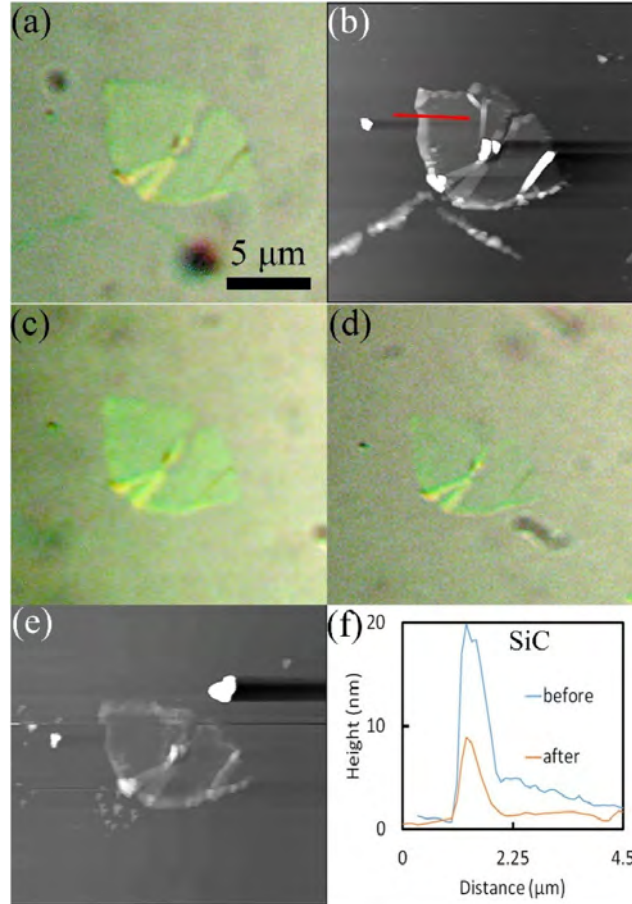
FIGURE 5.8. (a) Optical image of a thin graphene flake exfoliated on SiC and (b) the corresponding AFM image. (c) and (d) Optical images of the same flake after 10 min irradiation and (d) 20 min irradiation. (e) AFM image corresponding to (d). (f) Height profiles for the flake before and after 20 min of irradiation along the red line drawn on (b). The scale bar on (a) is the scale for images (a)–(e).

since graphene on SiC etches despite SiC not having oxygen in the substrate, we propose that He$^+$ ion bombardment causes the etching by the mechanisms discussed previously of sputtering and vacancy formation [14]. Additionally, since SiC etches much less compared to SiO$_2$, we propose that oxygen reacting at defects etches graphene at a much faster rate than only ion bombardment. We did not measure the density of metastable He species in the chamber. Therefore, we did not consider the effects of metastable He in our experiment.
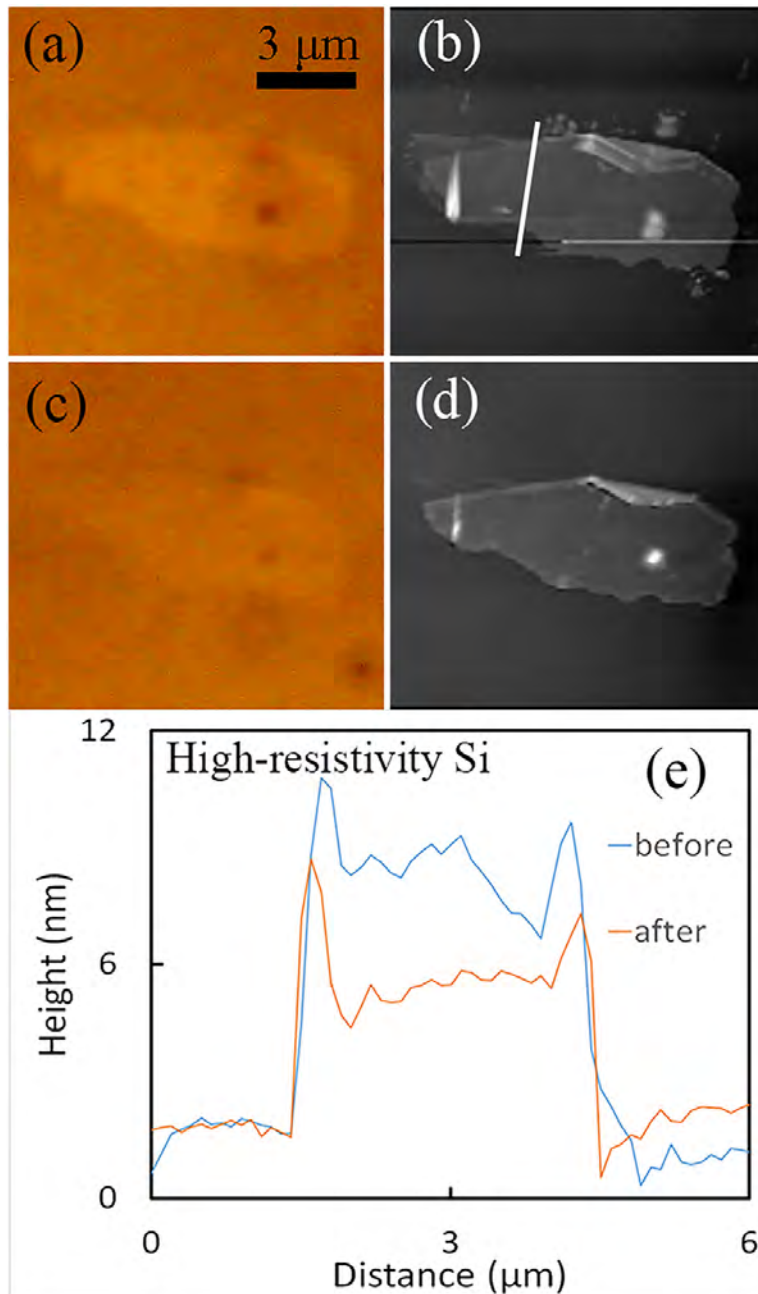
FIGURE 5.9. (a) Optical image of a thin graphene flake exfoliated on high resistivity Si and (b) the corresponding AFM image. (c) Optical image of the same flake after 10 min of irradiation and (d) the corresponding AFM image. (e) Height profiles for the flake before and after irradiation along the white line drawn on (b). The scale bar on (a) is the scale for images (a)–(d).

To further investigate the relationship between etching and substrate resistivity, we irradiated graphene exfoliated on the higher resistivity 10 Ωcm Si substrate. Since the resistance is higher, the incident electrons on the graphene would produce a higher negative potential than for the low-resistivity Si. Figure 5.9 (a) is an optical image of a 10 nm thin flake, and Figure 5.9 (b) is the corresponding AFM image. Figure 5.9 (c) is an optical image of the same flake after 10 min of irradiation. The flake appears fainter than the flake of Figure 5.9 (a), indicating that the flake has thinned. Figure 5.9 (d) is the corresponding AFM image. Figure 5.9 (e) shows the height profiles of the flake before and after the irradiation along the line shown in Figure 5.9 (b). The height has decreased to about 3–5 nm after the irradiation, suggesting that the higher the resistivity of the Si, the more the exfoliated graphene on the substrate etches. The increased damage on the graphene is seen on the higher resistivity Si but not on the low-resistivity Si. This corroborates our hypothesis that the substrates with greater resistivity allow negative charge to build up on the graphene creating an electric field which attracts He$^+$ ions.

Spinney et al. [27] and Sommer et al. [28] reported etching of carbon films and suspended graphene monolayers, respectively, using gas-assisted focused electron beam etching
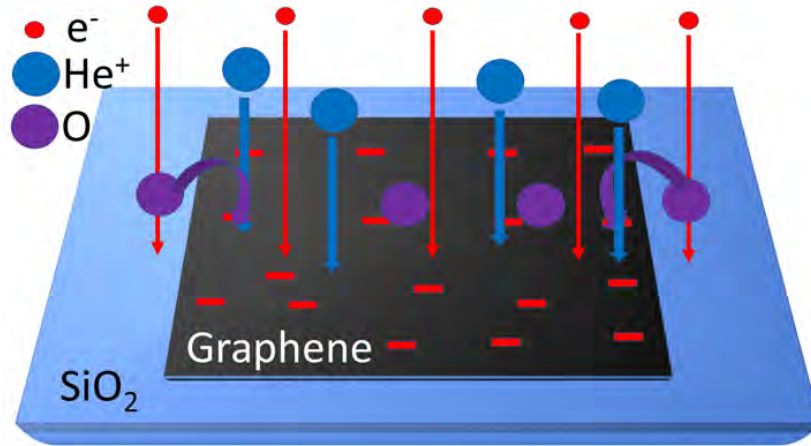
FIGURE 5.10. Our model illustrates the etching mechanism of graphene on SiO$_2$. Incident electrons from Helium plasma dissociate oxygen from the substrate and etches graphene from below.

at beam energies of 5 and 30 keV, respectively, with water vapor as the gas. It was proposed that etching occurred due to dissociation of water adsorbed on the sample surface resulting in oxidation of carbon. We note that carbon films contain defects, and the suspended graphene layer was reported in Ref. [28] to display a Raman D peak after etching, indicating the process induced defects. Thus, these experiments do not contradict our conclusion that oxygen reacts with defects formed by He$^+$ ions.

5.6. Summary and Conclusions

We propose that graphene exfoliated on SiO$_2$ experiences etching from the top of the sample as shown in Figure 5.10 rather than from the bottom as described in Ref. [1]. This is supported by our observation that thinner regions of graphene do not etch at a faster rate than thicker regions. We propose that oxygen is dissociated from the surrounding SiO$_2$ substrate and diffuses to above the graphene sample and etches it. This is in contrast with a previously proposed model [1] in which oxygen dissociates at the graphene/SiO$_2$ interface and etches the graphene from below. We find that exfoliated graphene does not etch on low-resistivity Si, in support of the oxygen dissociation hypothesis. We further find that etching does not occur on ITO, where etching would be expected from the previously proposed model [1] since ITO contains oxygen. However, etching occurs on higher resistivity Si and SiC, although much less than on SiO$_2$. We attribute this to negative charge build up on the graphene flakes that accelerates He$^+$ ions near the surface and causes sputtering and defect formation. As a result of the defects formed by the He$^+$ ions, oxygen can react with and etch graphene. This contrasts with the previous model [1] in which electrons cause the necessary defects to allow oxygen to etch graphene. We propose that graphene will etch on dielectric substrates, and if oxygen dissociates from the dielectric substrate, the etching occurs at a much higher rate. If there is no oxygen in the dielectric substrate, etching still occurs due to sputtering of the graphene by He$^+$ ions. We propose that conducting substrates, however, will not result in etching regardless of the dissociation of oxygen due to lack of He$^+$ ion bombardment.

5.7. Acknowledgement

5.8. References

[1] C. Chen, C. Wang, and D. Diao, Appl. Phys. Lett. 109, 053104 (2016).

[2] K. S. Novoselov, A. K. Geim, S. Morozov, D. Jiang, M. Katsnelson, I. Grigorieva, S. Dubonos, and A. A. Firsov, Nature 438, 197 (2005).

[3] C. M. Seah, B. Vigolo, S. P. Chai, and A. R. Mohamed, Carbon 105, 496 (2016).

[4] L. Xie, L. Jiao, and H. Dai, J. Am. Chem. Soc. 132, 14751 (2010).

[5] I. Childres, L. A. Jauregui, J. Tian, and Y. P. Chen, New J. Phys. 3, 025008 (2011).

[6] X. Yang, S. Tang, G. Ding, X. Xie, M. Jiang, and F. Huang, Nanotechnology 23, 025704 (2011).

[7] H. Al-Mumen, F. Rao, W. Li, and L. Dong, Nanomicro Lett. 6, 116 (2014).

[8] W. S. Lim et al., Carbon 50, 429 (2012).

[9] G. H. Han et al., ACS Nano 5, 263 (2011).

[10] M. D. Fischbein and M. Drndic, Appl. Phys. Lett. 93, 113107 (2008).

[11] M. C. Lemme, D. C. Bell, J. R. Williams, L. A. Stern, B. W. Baugher, P. Jarillo-Herrero, and C. M. Marcus, ACS Nano 3, 2674 (2009).

[12] F. Banhart, Rep. Prog. Phys. 62, 1181 (1999).

[13] M. L. Knotek and P. J. Feibelman, Phys. Rev. Lett. 40, 964 (1978).

[14] O. Lehtinen, J. Kotakoski, A. V. Krasheninnikov, A. Tolvanen, K. Nordlund, and J. Keinonen, Phys. Rev. B 81, 153401 (2010).

[15] J. D. Jones, R. K. Shah, G. F. Verbeck, and J. M. Perez, Small 8, 1066 (2012).

[16] J. D. Jones, W. D. Hoffmann, A. V. Jesseph, C. J. Morris, G. F. Verbeck, and J. M. Perez, Appl. Phys. Lett. 97, 233104 (2010).

[17] M. Morita, T. Ohmi, E. Hasegawa, M. Kawakami, and M. Ohwada, J. Appl. Phys. 68, 1272 (1990).

[18] Thin Film Devices, Inc., 1180N. Tustin Ave., Anaheim, CA 92897.

[19] S. Tanuma, C. J. Powell, and D. R. Penn, Surf. Interface Anal. 37, 1 (2005).

[20] M. Topsakal, H. Şahin, and S. Ciraci, Phys. Rev. B. 85, 155445 (2012).

[21] J. J. Fijol, A. M. Then, G. W. Tasker, and R. J. Soave, Appl. Surf. Sci. 48–49, 464 (1991).

[22] J. Luo, P. Tian, C. T. Pan, A. W. Robertson, J. H. Warner, E. W. Hill, and A. D. Briggs, ACS Nano 5, 1047 (2011).

[23] L. Reimer, Springer Series in Optical Sciences (Springer, Berlin, 1998), Vol. 45, p. 135.

[24] M. T. Postek and A. E. Vladár, Proc. SPIE 9636, 963605 (2015).

[25] A. Santos, N. Bundaleski, B. J. Shaw, A. G. Silva, and O. M. N. D. Teodoro, Vacuum 98, 37 (2013).

[26] C. G. Pantano and T. E. Madey, Appl. Surf. Sci. 7, 115 (1981).

[27] P. S. Spinney, D. G. Howitt, S. D. Collins, and R. L. Smith, Nanotechnology 20, 465301 (2009).

[28] B. Sommer, J. Sonntag, A. Ganczarczyk, D. Braam, G. Prinz, A. Lorke, and M. Geller, Sci. Rep. 5, 7781 (2015).

CHAPTER 6

RAPID AMBIENT DEGRADATION OF MONOLAYER MoS$_2$ AFTER HEATING IN

AIR [1]

6.1. Background

In contrast to graphene and hBN that are very stable in ambient air, TMD monolayers degrade after prolonged exposure to ambient air. The degradation of monolayer MoS$_2$ and WS$_2$ grown on SiO$_2$ substrates using CVD was first reported in Ref. [2]. These authors describe the noticeable formation of cracks along grain boundaries and quenching of PL in monolayers that were kept in ambient air for about a year. They attributed the degradation to oxidation at chalcogen vacancy sites. They found that water vapor played an important role in the degradation. In Ref. [4] it was reported that the degradation was a photo-induced process since it did not occur in samples that were shielded from light. Furthermore, photon irradiation at energies above the exciton binding energy resulted in degradation, while irradiation at lower energies had no effect. Consequently, it was thought that the degradation was due to Forster resonance energy transfer (FRET) [31]. In FRET, the photon emitted during exciton decay is virtual and excites other reactions, in this case, reactions that produce degradation. Degradation has also been reported in TMD monolayer flakes that were mechanically exfoliated on SiO$_2$ after about 4 months of ambient air exposure and attributed to adsorption of H$_2$O [5].

We investigate the accelerated degradation of CVD-grown MoS$_2$ monolayers that occurs after the monolayers are first preheated in air at 280-330 °C for 2h and then exposed to ambient air at RT. The accelerated degradation occurs on the order of about 2 weeks instead of a year, as observed when the monolayers are not preheated. We refer to degradation that occurs when the samples are not preheated as natural degradation. We found that in both accelerated and natural degradation, the degradation proceeds by the growth of

dendritic structures. Thus, we concluded that the same degradation mechanism occurs in both accelerated and natural degradation. To explore the degradation mechanism in more detail, we carried out a fractal analysis of the dendritic structures. We calculated the fractal dimension of the dendrite using the box counting method to be 1.6, strikingly close to the fractal dimension of structures formed by diffusion limited aggregation (DLA) [23]. We concluded that adsorbed H_2O molecules diffuse either on the monolayer surface or in the interface between the monolayer and SiO_2 and initiate degradation. We also carried out extensive Raman spectroscopy and XPS studies and concluded that dendritic areas have a Raman spectrum consistent with reported phonon shifts from defects [32], and that preheating produces additional MoO_3 oxide sites on the monolayer. This led us to propose a mechanism for degradation that builds upon a previously reported mechanism [26]. In our mechanism, the H_2O diffuses to oxide sites where they initiate chemical reactions that liquefy the oxides. The liquefied oxides cannot protect the monolayer from additional oxidation, resulting in a self-propelled degradation process. The accelerated degradation proceeds faster because of the additional oxide sites introduced during preheating.

6.2. Abstract

We report that heating chemical vapor deposition grown monolayer MoS_2 in air at temperatures as low as 285 °C for 2 h results in rapid degradation of the monolayer within 2.5 weeks of ambient air exposure after heating. We find that the rapid degradation proceeds via the growth of dendrites on the basal plane that have a fractal dimension close to that of diffusion-limited aggregation. We also observe dendrites in unheated samples that have been in ambient air for a year. We explain the rapid degradation after heating to an increase in MoO_3. We propose that the mechanism for dendrite growth involves the diffusion of H_2O to oxide sites. This results in the liquefication of the oxides. The liquefied oxides do not protect the surface from further oxidation. Putting heated samples in a dry box for 2 weeks immediately after heating prevents the rapid degradation from occurring.

6.3. Introduction

Two-dimensional transition metal dichalcogenides (TMDs), specifically MoS_2, have been extensively studied in recent years due to their potential applications in optoelectronics [1]. However, there have been numerous studies on the stability of these materials under ambient conditions [2–6], which may be a large impediment to their realization in practical applications. These reports demonstrate that a degradation effect occurs for MoS_2 layers on SiO_2, either chemical vapor deposition (CVD) grown or exfoliated, after they are left for an extended period in ambient air at room temperature (RT). For CVD grown monolayer films, the onset time for noticeable degradation is about a year. The phenomenon for CVD grown samples was first reported by Gao et al. [2] to involve extensive cracking along grain boundaries and quenching of photoluminescence. They attributed the cracking to a mechanism in which chalcogen vacancies are thermodynamically favorable to be replaced by O and OH radicals, causing subsequent oxidation and degradation of the monolayer. In another study, CVD grown MoS_2 monolayers were reported to show cracking along grain boundaries after 18 months in ambient air, which was attributed to oxidation at sulfur vacancies and film stress [3]. It was reported that changing the growth conditions could slow the degradation, presumably by changing the vacancy density and film stress. Finally, Kotsakidis et al. [4] reported that ambient degradation of CVD grown monolayer WS_2 is a photo-induced process since samples kept in darkness did not show changes after 10 months but samples in ambient light developed changes attributed to photo-oxidation at sulfur vacancies. For exfoliated flakes, Budania et al. [5] reported that flakes left in ambient air for about 4 months developed small speckles that, given enough time, thin and decompose the flake. The authors attributed the speckles to water (H_2O) adsorption and found that the speckles decrease in size and number after the sample is put in vacuum.

In this paper, we report the degradation of CVD grown MoS_2 monolayers on SiO_2 under ambient conditions that occurs over a significantly shorter time on the order of weeks. The degradation occurs after the sample is first heated in air at temperatures as low as 285 °C for 2 h. We study the degradation using optical microscopy, atomic force microscopy

(AFM), Raman spectroscopy and x-ray photoelectron spectroscopy (XPS). Our results are important in understanding unintentional effects when TMD monolayers are heated in air and then exposed to ambient conditions. Examples include techniques for thinning thick TMD multi-layers into monolayers. For example, Wu et al. [7] and Zhou et al. [8] reported the thinning of MoS_2 by thermally annealing samples in air at 330 °C and above, where the thinning initiated at defects on the basal plane by creation of etch pits that eventually removed a layer. Laser thinning has also been reported, such as for WS_2 [9] and MoS_2 [10]. In this technique, a laser irradiates the sample in air, heating it to local temperatures at which layer removal occurs. These techniques work because the bottom layer is more chemically stable and has a greater thermal conductivity due to its contact with the substrate and, therefore, is not etched, whereas the thicker layers are etched [11]. Another application of heating is to reveal and study oxidation and wear sites such as grain boundaries. Rong et al. [12] heated monolayer WS_2 films at about 380 °C for 20 min in air to selectively etch the grain boundaries and determine the quality of the films. In another paper [13], AFM images were used to characterize wear and oxidation of TMD monolayers after exposure to air at temperatures of about 400 °C for 5 min. Finally, Lu et al. [14] proposed that oxidation of vacancies in TMD monolayers by laser heating may significantly enhance their conductivity and photoconductivity by passivating the surface. In all the above reports [7–14], it has been assumed that the monolayer is not adversely affected by the heating. However, our results indicate that monolayers are affected, so appropriate measures should be taken. Other applications of thermal treatments include bandgap modulation of MoS_2 monolayers by vacuum thermal annealing [15], and growth of large MoS_2 monolayers using a high thermal conductivity Au foil [16]. We note that our observations are distinct from previously reported accelerated degradation effects in which the sample is kept at elevated temperatures of 80 °C and 65% relative humidity for 20 min [2], or on a hot plate at 350 °C for 5 min in air [3]. In the above cases, the accelerated degradation was concluded to have occurred while the sample was heated. In our experiments, the rapid degradation occurs after the sample is heated and placed in ambient air at RT.

6.4. Methods

The MoS_2 films were grown on 300 nm thick SiO_2/Si substrates using sodium chloride (NaCl) as a promoter [17]. The MoS_2 substrates were prepared by dissolving 1 mg of NaCl (99.5%) in 1 ml of ammonium hydroxide (28% NH_3 in H_2O) with sonication for 10 min. The promoter was spread evenly over the substrates by spin coating at 3000 rpm for 60 s. The CVD setup and growth conditions used are the same as those previously reported [17]. Briefly, the tube furnace was cleaned by annealing at 900 °C for 2 h under air flow. After the tube furnace was brought to RT, the growth substrate and crucibles containing sulfur and MoO_3 were placed in the tube. Before raising the temperature of the furnace, the tube was flushed with 500 sccm of ultrahigh purity Ar gas at atmospheric pressure for 10 min. The Ar flow was then reduced to 100 sccm, and the temperature ramped at a rate of 25 °C/min to a growth temperature of 800 °C for 20 min. The degradation experiments were carried out by heating the samples in a different tube furnace in air at atmospheric pressure. The AFM images were collected using an Ambios Q-Scope in tapping mode. The Raman mapping was performed using a Thermo Scientific DXR Raman microscope using a 532 nm laser, beam diameter of 0.8 μm and scan step size of 1 μm. The XPS data was collected using a PHI 5000 Versaprobe scanning XPS microprobe with a monochromated Al K-alpha source at 1486.7 eV.

6.5. Results and Discussion

Figures 6.1 (a) and (b) show optical and AFM images, respectively, of a CVD grown MoS_2 monolayer on SiO_2 approximately 1 month after growth. The white arrows in (b) indicate holes in the SiO_2 substrate and monolayer that appear after growth. Figure 6.1 (c) shows an optical image of the same monolayer immediately after heating in air at 330 °C for 2 h. Etch pits are observed on the basal plane, as indicated by the two red arrows. Figure 6.1 (d) shows an optical image of the monolayer after 2.5 weeks in ambient air at RT and relative humidity of about 43%. The red arrow indicates a large area of reduced contrast on the basal plane. Figure 6.1 (e) is an AFM image of the boxed region in Figure 6.1 (d) showing that regions of reduced contrast contain dendrites. The white arrows indicate holes shown
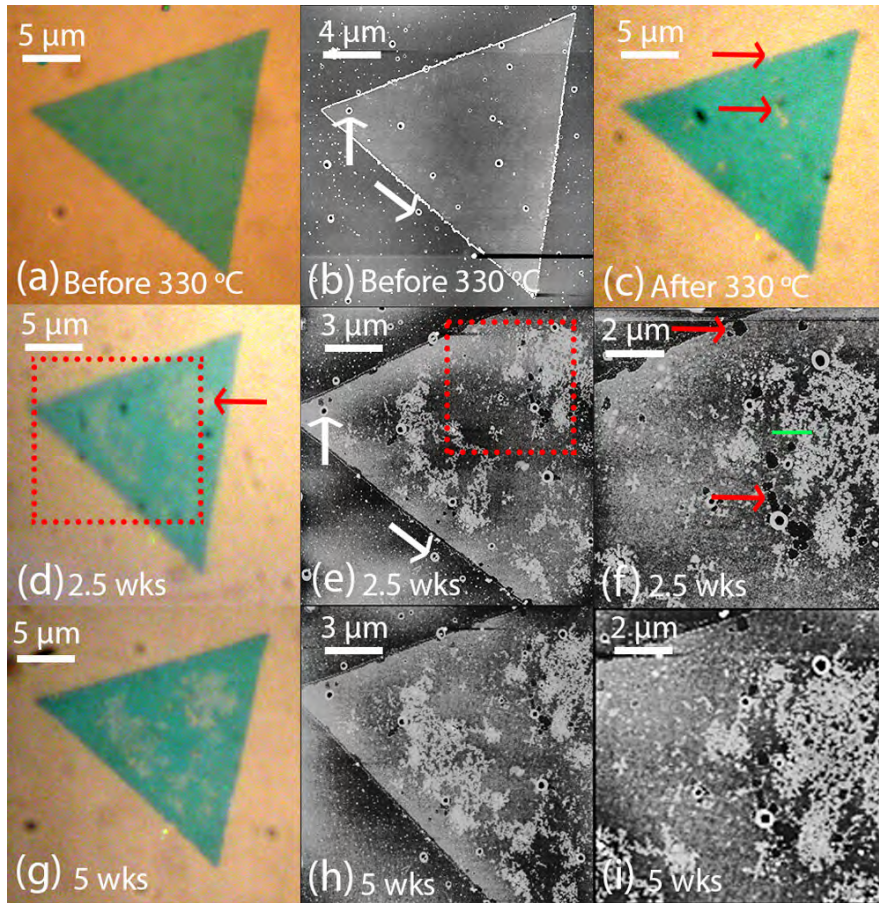
FIGURE 6.1. (a) and (b) Optical and AFM images, respectively, of a CVD grown MoS_2 monolayer 1 month after growth and just before heating. The white arrows indicate holes on the substrate and monolayer that appear after growth. (c) Optical image after heating in air at 330 °C for 2 h. Etch pits are indicated by the red arrows. (d) Optical image after exposure to ambient air for 2.5 weeks. Areas of reduced contrast are indicated by the red arrow. (e) AFM image of the red boxed area in (d). The white arrows indicate holes shown in (b). (f) AFM image of the boxed area in (e), showing etch pits indicated by the red arrows. The green line indicates the distance along which the height profile was measured. (g) and (h) Optical and AFM images, respectively, after an additional 2.5 weeks in ambient air. (i) AFM image of the area in (f) after an additional 2.5 weeks under ambient air.

in Figure 6.1 (b). These holes appear in other publications reporting images of CVD grown monolayers [18, 19]; to our knowledge, they have not been previously discussed. We believe the holes occur during CVD growth and are not due to the pre-heating or degradation, since they are also observed in Figure 6.1 (b), before heating and degradation. Figure 6.1 (f) shows a high-resolution image of the boxed region in Figure 6.1 (e), showing in detail the dendritic structure. The green line indicates a region along which an AFM height profile was obtained, as discussed below. The red arrows in Figure 6.1 (f) indicate the same etch pits indicated by the red arrows in Figure 6.1 (c). Figure 6.1 (g) and (h) show optical and AFM images, respectively, of the sample after an additional 2.5 weeks in the same ambient environment. The areas of reduced optical contrast have grown, as shown by the increase of the dendritic areas in the AFM image. Figure 6.1 (i) shows the same region as in Figure 6.1 (f) after an additional 2.5 weeks. The dendrites have grown, whereas the etch pits indicated by the red arrows have not grown. This observation shows that the mechanism for the growth of etch pits is different from that of the dendrites.

In addition, we note that the dendrites are not all originating from etch pits. Etch pits have been reported by Yamamoto et al. [20] to nucleate at preexisting vacancy defects. At a given temperature, etch pits grow laterally in size by thermal oxidation of edge sites given a longer thermal exposure time, and have a constant pit density. We conclude that the etch pits we observe after heating are due to preexisting defects such as vacancies, and that other areas of the monolayer with no etch pits did not have such preexisting defects. Therefore, there is no relationship between dendrites and etch pits. To study the morphology of the dendrites, we extracted the pixels of the large dendritic area on the right side of Figure 6.1 (f) and converted it to black pixels for fractal analysis. Figure 6.2 (a) is the result of this conversion. Figure 6.2 (b) shows the AFM height profile along the green line in Figure 6.2 (a), which is in the same location as the green line in Figure 6.1 (f). The dendrites have a maximum height of about 2 nm. We calculated the fractal dimension of the dendritic structure in Figure 6.2 (a) using the box counting method [21] and software Fractalyse version 2.4 [22]. Figure 6.2 (c) shows a plot of the *log* of the number of boxes of side length r, $N(r)$,
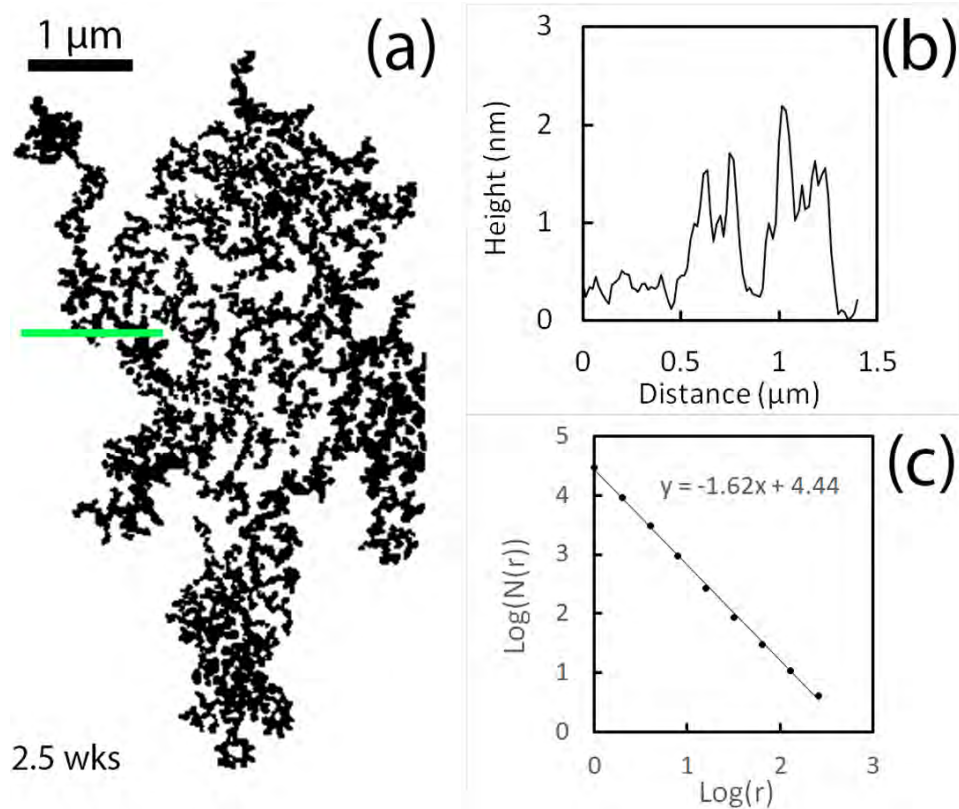
FIGURE 6.2. (a) Dendrite structure extracted from Figure 6.1 (f). (b) Height profile along the green line in (a) and Figure 6.1 (f). (c) Plot of *log* of the number of boxes of side length r, $N(r)$, that is needed to cover the dendrite versus $log(r)$, yielding a fractal dimension of 1.62.

which is needed to cover the dendritic structure versus $log(r)$. The solid circles are data points. Linear regression results in the line shown in Figure 6.2 (c) that has a slope of 1.62, which gives a fractal dimension of 1.62. This number is close to the fractal dimension of 1.59 for diffusion-limited aggregation (DLA) [23]. We do not know exactly where the formation location is, whether it is the upper or lower surface. However, we hypothesize that water is adsorbed on top of the MoS_2 monolayer and oxidizes the sample by diffusing along the upper surface because we observe the dendrites sometimes originating in the basal plane. If it were diffusing from underneath, we believe the dendrites would always originate at the edges, as observed in previous reports of formation of labyrinth structures due to wetting of the MoS_2 monolayer-mica interface [24].
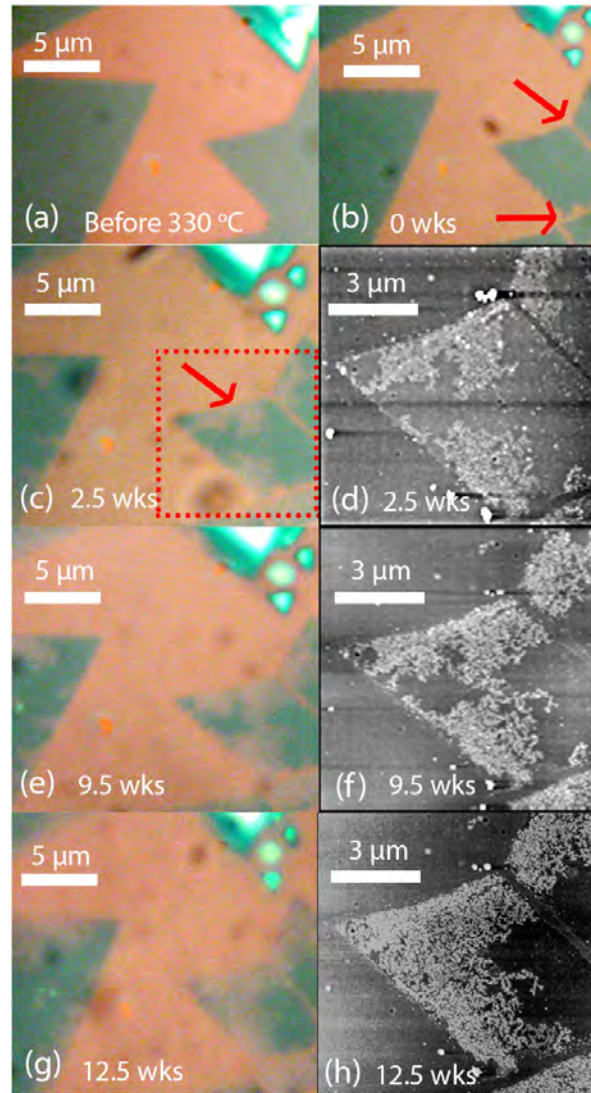
FIGURE 6.3. (a) Optical image of a CVD grown MoS_2 monolayer 1 month after growth and just before heating. (b) Optical image of the monolayer after heating in air at 330 °C for 2 h. Etching of grain boundaries is indicated by the red arrows. (c) Optical image after the monolayer was left in an ambient air for 2.5 weeks. The red arrow indicates an area of reduced optical contrast. (d) AFM image of the red boxed area in (c). (e) and (f) Optical and AFM images, respectively, after an additional 7 weeks in ambient air. (g) and (h) Optical and AFM images, respectively, after an additional 3 weeks in ambient air.
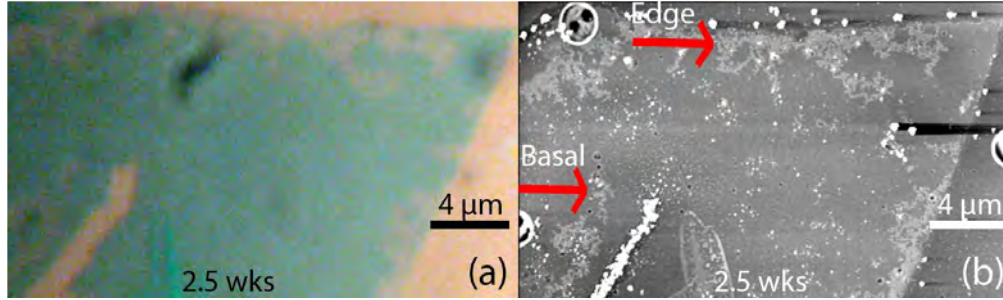
FIGURE 6.4. (a) Optical image of monolayer MoS$_2$ after heating at 330 °C in air for 2 h and then exposure to ambient air for 2.5 weeks. (b) AFM image of the monolayer in (a). Red arrows indicate dendrites originating on the edge and basal plane.

Figure 6.3 (a) shows an optical image of a different CVD grown MoS$_2$ monolayer on MoS$_2$ that is about 1 month old. Figure 6.3 (b) shows an optical image of the same monolayer immediately after heating in air at 330 °C for 2 h. The red arrows show the etching of grain boundaries. There appears to be no regions on the basal plane having reduced optical contrast. Figure 6.3 (c) shows an optical image of the same monolayer after 2.5 weeks under the same ambient conditions as in Figure 6.1. Once again, areas of reduced optical contrast are observed on the basal plane, as indicated by the red arrow. Figure 6.3 (d) is an AFM image of the boxed region in Figure 6.3 (c) showing that the areas of reduced optical contrast are dendritic, as in Figure 6.1. The dendrites in this case appear to originate from the edges of the monolayer, in contrast to the dendrites in the case before in Figure 6.1 that appear to originate within the basal plane. We do not know exactly why the dendrites originate at locations inside the basal plane in Figure 6.1 while at the edges in Figure 6.3.

We propose that dendrites originate at edges due to their high concentration of oxidized sites, and on areas of the basal plane that develop a high concentration of oxidized sites due to the heating. We grew on about 23 substrates and observed dendrites on all monolayers grown on a given substrate. For a given monolayer, we found that dendrites appear to originate only at the edges, or only the basal plane, or both the edges and basal plane, despite all these monolayers being put under the same experimental conditions. In

Figure 6.4, we have included optical and AFM images of a monolayer in which the dendrites originate at both edges and the basal plane. Once the dendrites start growing, we find that, given enough time, the dendrites become more densely packed and grow over the inside of the basal plane and the edges, covering most of the monolayer. In Figure 6.5, we have included an image of a monolayer that has been entirely covered with dendrites. Figures 6.3 (e) and (f) show optical and AFM images, respectively, of the sample after an additional 7 weeks under the same ambient conditions. The dendrites have increased in size, but the cracks formed by the etching of the grain boundaries have not significantly changed. Figures 6.3 (g) and (h) show optical and AFM images, respectively, of the monolayer after an additional 3 weeks in ambient air. The dendrites have almost completely covered the left side of the sample.

We conclude that the dendrites are not limited to grow from areas of grain boundaries. Our results are different from [2–6] in that we observe that dendrites originate not only on edges but also the basal plane. This may be because the heating introduces a high concentration of oxidized sites on areas of the basal plane. We also report the degradation involves the growth of raised dendrites, whereas the references report that degradation involves cracking of the monolayer. In order to investigate the temperature dependence of the degradation, we compared samples that were preheated at 260 °C and 285 °C.
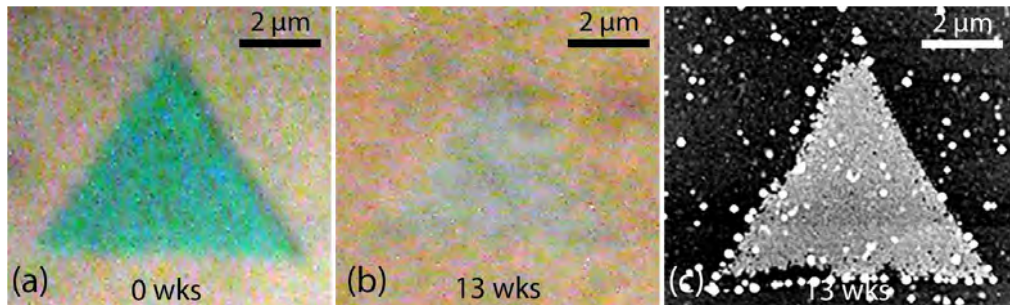
FIGURE 6.5. (a) Optical image of monolayer MoS_2 immediately after heating at 330 °C in air for 2 h. (b) Optical image of the sample in (a) after exposure to ambient air for 13 weeks. (c) AFM image of the sample in (b) showing complete coverage of the basal plane by dendrites.
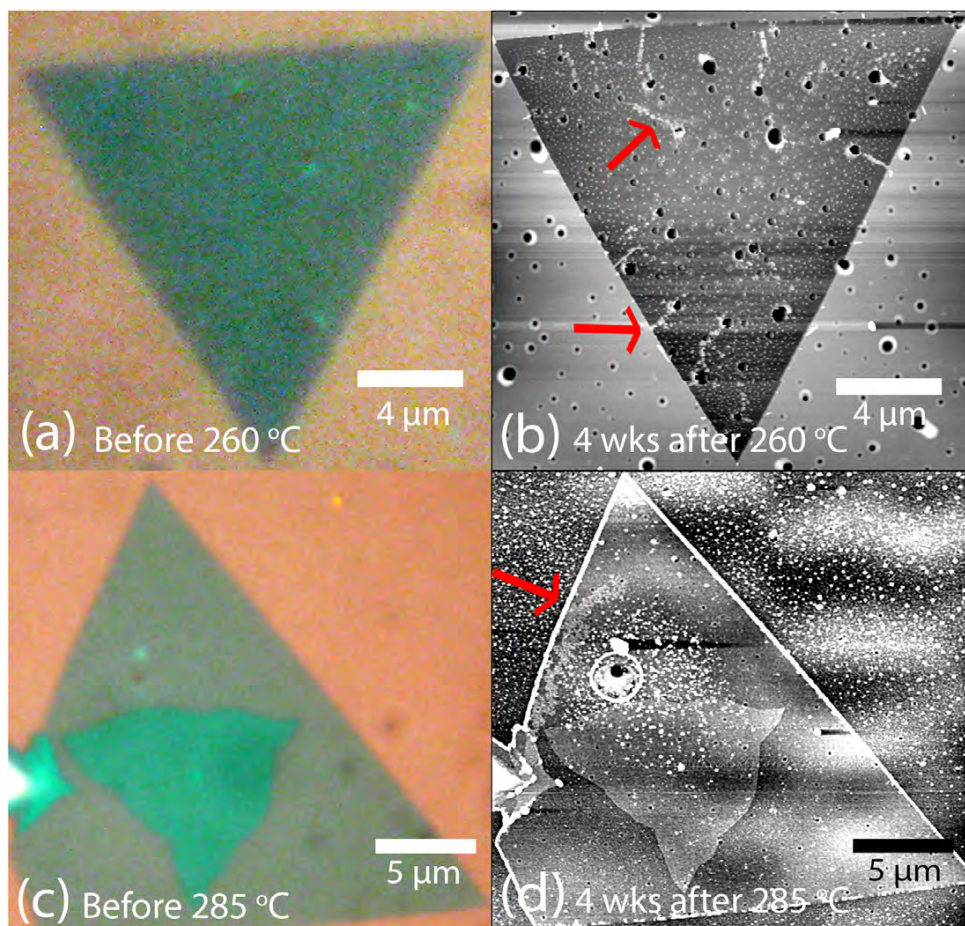
FIGURE 6.6. (a) Optical image of a CVD grown MoS_2 monolayer 1 month after growth and just prior to heating. (b) AFM image after heating in air at 260 °C for 2 h followed by exposure to ambient air for 1 month. The red arrows indicate small dendrites. (c) Optical image of a different CVD grown MoS_2 monolayer 1 month after growth and just prior to heating. (d) AFM image after heating in air at 285 °C for 2 h followed by exposure to ambient air for 1 month. The red arrow shows larger dendrites.

Figure 6.6 (a) shows an optical image of a monolayer about 1 month after growth. The monolayer was then preheated at 260 °C for 2 h. Figure 6.6 (b) shows an AFM image of the monolayer after 1 month in ambient air. The red arrows indicate the formation of small dendrites. Optically, the dendrites are not observable. Figure 6.6 (c) shows an optical image of a different monolayer that is about 1 month old. The sample was heated at 285 °C
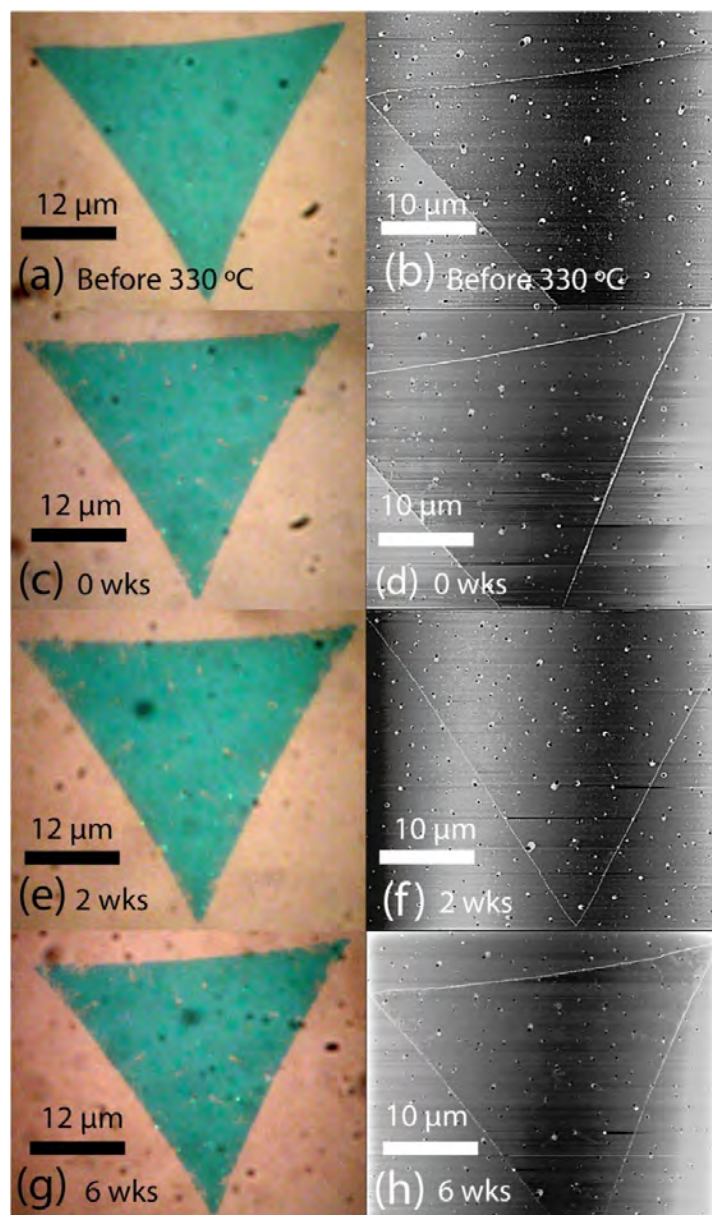
FIGURE 6.7. (a) and (b) Optical and AFM images, respectively, of a CVD grown MoS$_2$ monolayer 2 months after growth and just prior to heating. (c) and (d) Optical and AFM images, respectively, after heating in air at 330 °C for 2 h. (e) and (f) Optical and AFM images, respectively, after 2 weeks in the dry box. (g) and (h) Optical and AFM images, respectively, after exposure to ambient air for a month.

for 2 h in air. Figure 6.6 (d) shows an AFM image of the monolayer after about 1 month of exposure to ambient air. The red arrow indicates the formation of a larger dendritic area that is also observed optically. As shown in Figures 6.1 and 6.3, preheating at 330 °C causes significantly larger dendritic areas. To study the degradation mechanism further, we exposed preheated samples to a low-humidity environment immediately after heating. Figures 6.7 (a) and (b) show optical and AFM images, respectively, of a CVD grown MoS_2 monolayer about 2 months after growth. Figures 6.7 (c) and (d) show optical and AFM images, respectively, of the same monolayer immediately after heating at 330 °C for 2 h. There are visible etch pits but no regions of low optical contrast. The sample was then immediately placed in a dry box at approximately 5% relative humidity and RT. The dry box was transparent, and the sample was exposed to ambient light while in the dry box. Figures 6.7 (e) and (f) show optical and AFM images, respectively, of the monolayer after 2 weeks in the dry box. No noticeable degradation is observed. The sample was then removed from the dry box and placed in ambient air at about 53% relative humidity and RT. Figures 6.7 (g) and (h) show optical and AFM images, respectively, of the monolayer after 1 month in ambient air, showing no significant changes.

From these results, we conclude that water vapor in the air is necessary for the dendrites to form; and, the rapid degradation exhibited by preheated samples is slowed by putting them in a dry box for 2 weeks before long-term exposure to ambient air. The latter conclusion is distinct from that of Gao et al. [2] who reported that the degradation of CVD grown WS_2 monolayers is slowed while the sample is kept with a desiccant. Instead, we find that the rapid degradation in ambient air is prevented during the period of observation of 1 month. We also did an experiment in which samples were placed in the dry box for 1 week, heated at 330 °C for 2 h, and then exposed to ambient air for 2 weeks. As shown in Figure 6.8, these samples developed significantly fewer dendrites after exposure to ambient air than the samples in Figures 6.1 and 6.3 that were not placed in a dry box before heating. We attribute this result to less adsorbed water on samples placed in the dry box. We propose these samples oxidize less when heated due to less adsorbed water, resulting in less

oxidized sites and less degradation when exposed to ambient air. We also studied samples that were grown using the NaCl promoter but not preheated before exposure to ambient air. The samples were exposed to air for a year. The exposure time is like that used in previous studies on degradation [2, 3]. These experiments provide a control to determine if the NaCl promoter affected the stability of MoS_2. Figure 6.9 (a) shows an optical image of an unheated monolayer kept in ambient air for a year. An area of reduced optical contrast is indicated by the red arrow. Figure 6.9 (b) is the corresponding AFM image. The area of
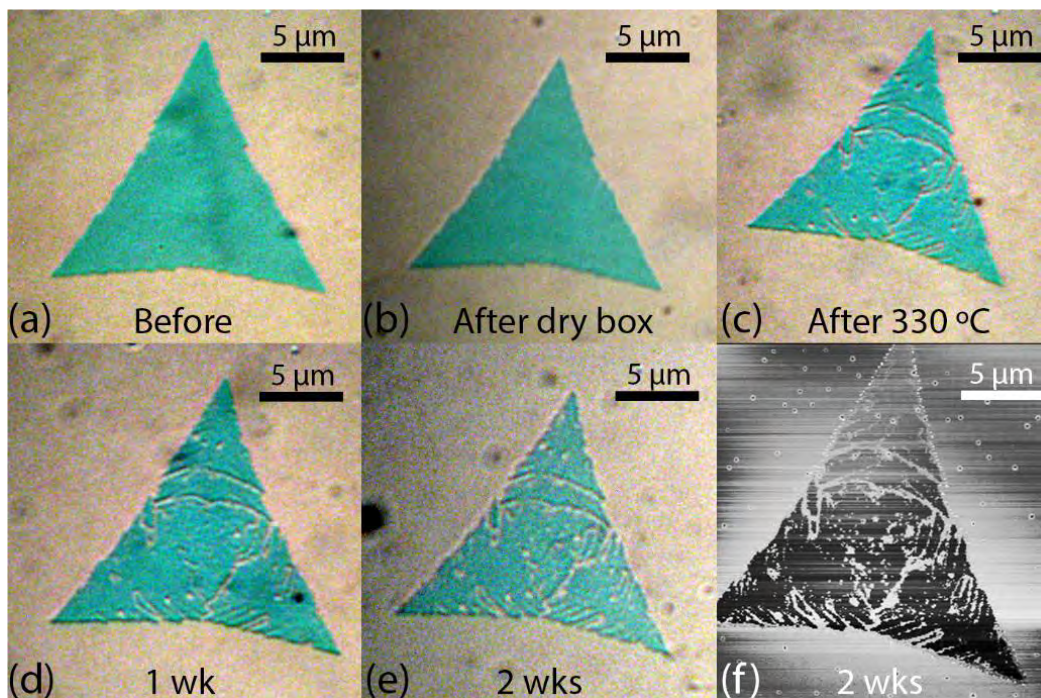
FIGURE 6.8. (a) Optical image of a week old MoS_2 monolayer before placement in a dry box. (b) Optical image of the sample in (a) after 1 week in a dry box. (c) Optical image of the sample in (b) immediately after heating at 330 °C for 2 h in air. Etching of the sample along grain boundaries is observed. (d) and (e) Optical images of the sample in (c) after exposure to ambient air for 1 week and 2 weeks, respectively. The etched regions do not appear significantly different after the exposure to ambient air. (f) AFM image of the sample in (e) showing significantly fewer dendrites than in samples shown in Figures 6.1 and 6.3, that were not placed in a dry box before heating.
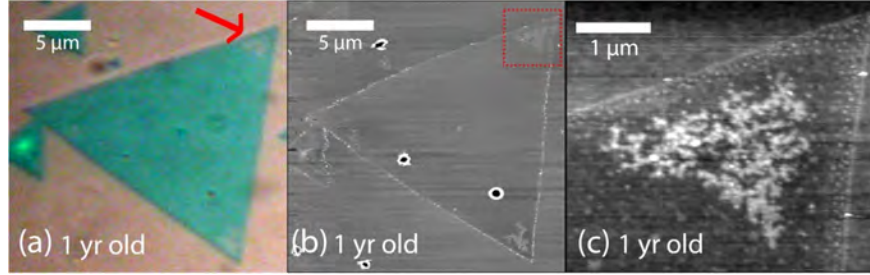
FIGURE 6.9. (a) Optical image of a CVD grown MoS$_2$ monolayer 1 year after growth. The red arrow indicates an area of reduced contrast. (b) AFM image of the monolayer. (c) High-resolution AFM image of the boxed area in (b).

reduced optical contrast is enclosed by the red box. Figure 6.9 (c) shows a high-resolution AFM image of the boxed area in Figure 6.9 (b) showing dendrites. The dendrites resemble those in Figures 6.1 and 6.3, in which the samples rapidly degraded. These observations indicate that the mechanism for rapid degradation of preheated samples may be like that of the slow degradation previously reported [2, 3]. The amount of degradation in the unheated sample shown in Figure 6.9 is less than or comparable to that reported for samples that were exposed to air for a year [2, 3], showing that the NaCl in our experiment does not adversely affect the stability of unheated MoS$_2$. We also heated samples at 330 °C for 2 h that were grown without using NaCl and found that dendrites started to grow after 5 days of ambient air exposure, as shown in Figure 6.10. These results suggest that NaCl does not influence the stability of MoS$_2$. The MoS$_2$ monolayers were grown on SiO$_2$/Si substrates without NaCl using the same CVD system used in the NaCl-assisted growth. The substrates were cleaned using acetone, alcohol, and DI water before insertion into the tube furnace with source crucibles.

Growth was started by flowing 500 sccm of ultrahigh-purity Ar gas for 10 min and then reducing the flow rate to 10 sccm, while ramping the temperature to 700 °C at a rate of 25 °C/min. After this, the furnace was turned off and allowed to cool to RT naturally. The MoS$_2$ monolayer domain sizes we obtained were about 5 μm, on the order of previous reports [2, 3]. The use of NaCl as a promoter has been shown to enable 5-100× increases
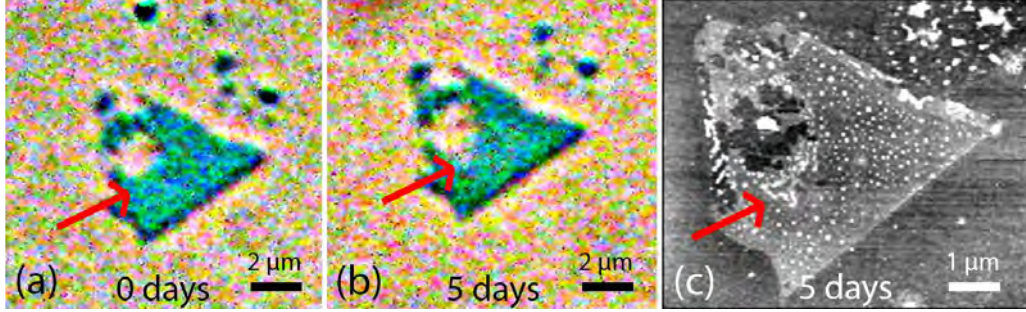
FIGURE 6.10. MoS$_2$ monolayer grown on SiO$_2$ using CVD without NaCl. (a) Optical image right after heating in air at 330 °C for 2h. Red arrow indicates a region of the monolayer that has not degraded. (b) Optical image after 5 days in ambient air. Red arrow indicates a region of reduced optical contrast. (c) AFM image of the sample in (b). Red arrow indicates a dendrite.

in MoS$_2$ monolayer domain size [33, 34]. The domain sizes we obtained by using NaCl as a promoter were as large as 40 μm.

We also studied the samples using Raman spectroscopy and XPS. Figure 6.11 (a) shows, for reference, an AFM image of the sample shown in Figure 6.1 (h) that was preheated at 330 °C and then exposed to air for 5 weeks. Figure 6.11 (b) shows a Raman map of the E$_{2g}$ peak at about 383 cm^{-1}. Areas of lower E$_{2g}$ intensity correspond to the dendritic areas in Figure 6.11(a). Figure 6.11(c) shows a map of the Si Raman peak from the substrate at about 520 cm^{-1}. A larger Si peak is observed for the dendritic areas, indicating that the dendritic areas may contain less material.

However, the AFM images show many elevated regions in the dendritic areas. A possible explanation for this is that the material in the dendrites may be sharper than the AFM tip, causing them to appear larger than expected. Figure 6.11 (d) shows Raman spectra taken at the four black cross marks, labelled 1-4, in Figure 6.11 (b), with decreasing peak intensity, corresponding to cross marks further from the upper-right vertex of the monolayer. It is observed that the E$_{2g}$ peak shifts to higher wavenumbers for locations further from the vertex and closer to the dendrites, while the A$_{1g}$ peak does not shift. Peak shifts in the Raman spectrum of monolayer MoS$_2$ have been attributed to defects [25]. Figures 6.12

110
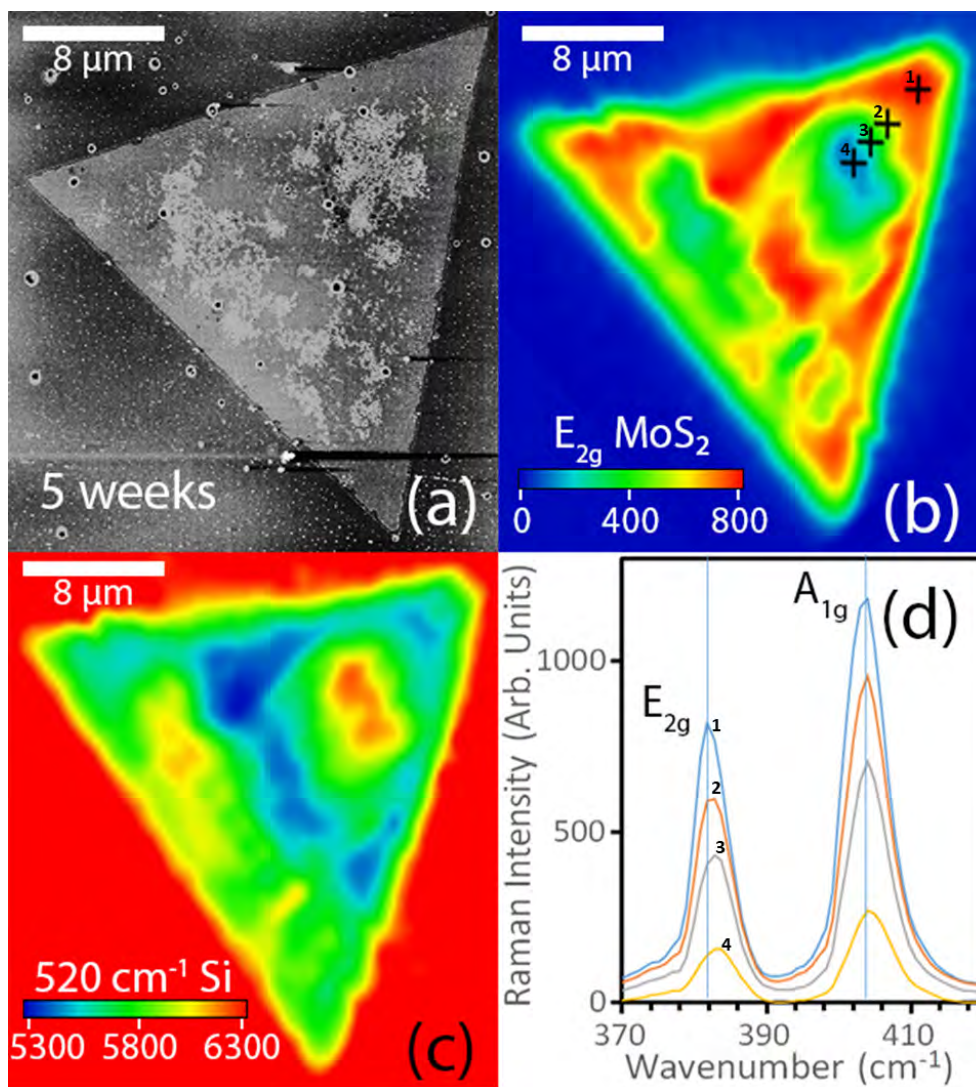
FIGURE 6.11. (a) AFM image of the sample in Figure 6.1(h). (b) Raman spectroscopy map of the E_{2g} peak of the sample, where intensity increases from blue to red, as indicated by the legend numbered in arbitrary units. (c) Raman spectroscopy map of the Si peak at 520 cm^{-1}. (d) Raman spectra taken at the points indicated by black crosses in (b), where decreasing peak intensity corresponds with crosses further from the vertex.

and 6.13 show XPS spectra of the Mo 3d region acquired over an area of 200×200 μm^2. The solid circles are data points, and the solid gray curves are fits using the 5 Lorentzian curves labeled 1–5, representing the (1) S 2s, (2) Mo^{4+} 3d$_{5/2}$, (3) Mo^{4+} 3d$_{3/2}$, (4) Mo^{6+}
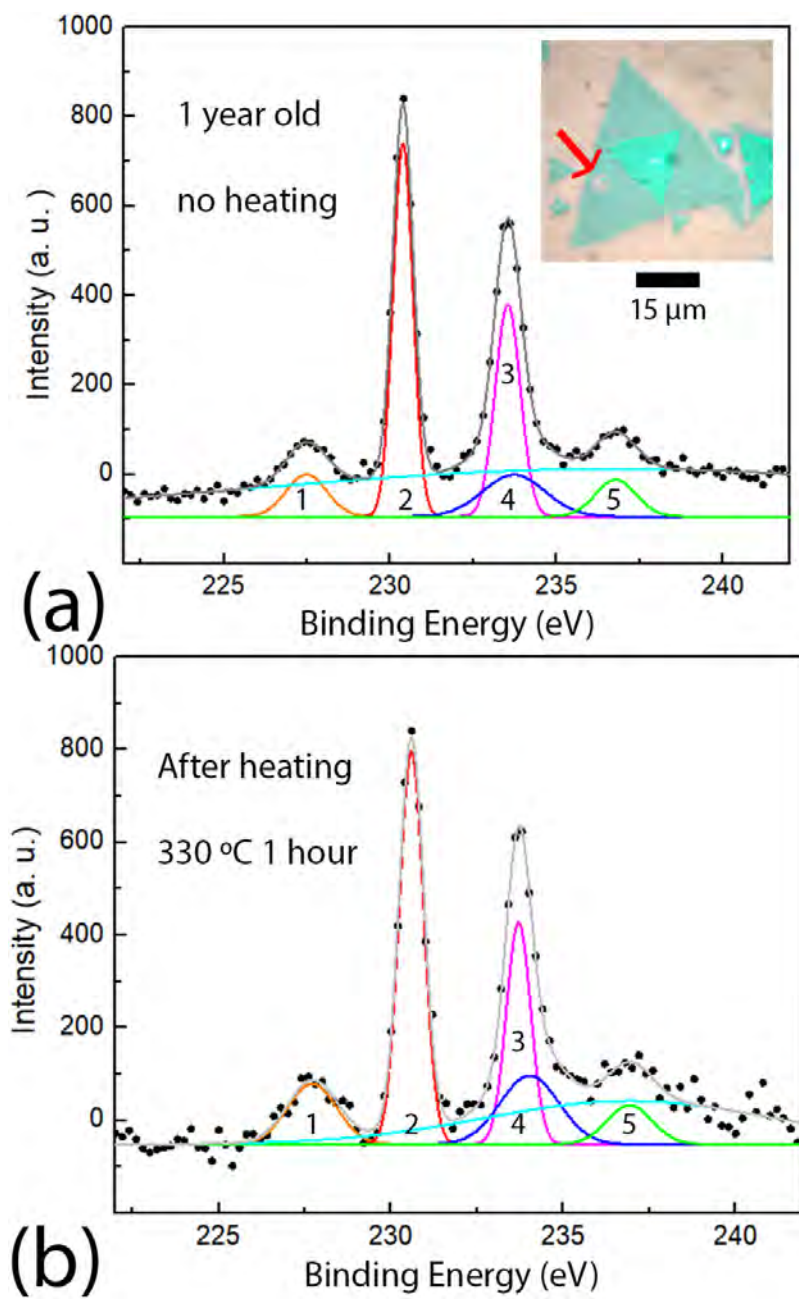
FIGURE 6.12. (a) XPS spectrum acquired over a $200 \times 200 \ \mu m^2$ area of a 1-year old CVD grown MoS_2 film. The solid circles are data points, and the solid gray curve is a fit using the 5 Lorentzian curves indicated 1–5. The inset shows a sample in the center of the acquisition area. (b) XPS spectrum after heating at 330 °C for 1 h.

$3d_{5/2}$, and (5) Mo^{6+} $3d_{3/2}$ peaks. The curves were normalized so that they have the same intensity of the Mo^{4+} $3d_{5/2}$ peak. The insets in Figures 6.12 and 6.13 show optical images of samples near the center of the XPS acquisition area. Figure 6.12 (a) shows the spectrum of an unheated 1-year old sample. The inset shows a small area of reduced optical contrast, as indicated by the red arrow. The deconvolved spectrum shows Mo^{6+} peaks, attributed to MoO_3, indicating that MoS_2 monolayers oxidize under ambient conditions, in agreement with [2]. We then heated the sample at 330 °C for 1 h. As shown in Figure 6.12 (b), the XPS spectrum taken over the same area immediately after heating has larger Mo^{6+} oxide peaks, indicating more oxidation has occurred during heating. Figure 6.13 shows the XPS spectrum of the sample shown in Figures 6.3 (g) and (h) that was preheated at 330 °C and then exposed to air for 12.5 weeks. The deconvolved spectrum shows significantly larger Mo^{6+} peaks, as compared to the freshly heated sample in Figure 6.12 (b).

We also did XPS of samples that were heated at 260 °C and 285 °C in air and then exposed to ambient air for 3 weeks. As shown in Figure 6.14, the sample heated at 285 °C showed higher Mo^{6+} peaks that correspond to MoO_3. This agrees with our proposed mechanism that rapid degradation is due to the formation of MoO_3. Compared to heating at 285 °C, heating at 260 °C makes the monolayers less prone to develop MoO_3 after 3 weeks of ambient air exposure, which makes the degradation slower and less noticeable. From all the above results, we conclude the following. Water vapor in the air is necessary for the rapid degradation to occur. Since the fractal dimension of the dendrites is close to that of DLA, the mechanism for rapid degradation may involve surface diffusion of reactants such as H_2O molecules. Areas having dendrites show increased defects according to Raman spectroscopy, and samples with a high concentration of dendrites show increased Mo^{6+} peaks corresponding to MoO_3 oxidation. Based on these observations, we propose a mechanism for degradation based on a mechanism recently proposed by Afanasiev et al. [26] for the oxidation of nanodispersed MoS_2 particles in ambient air at RT. These authors found that exposure for a year results in significant degradation and liquefication of the particles. They proposed that, after several minutes to hours of exposure, the edges of the particles become
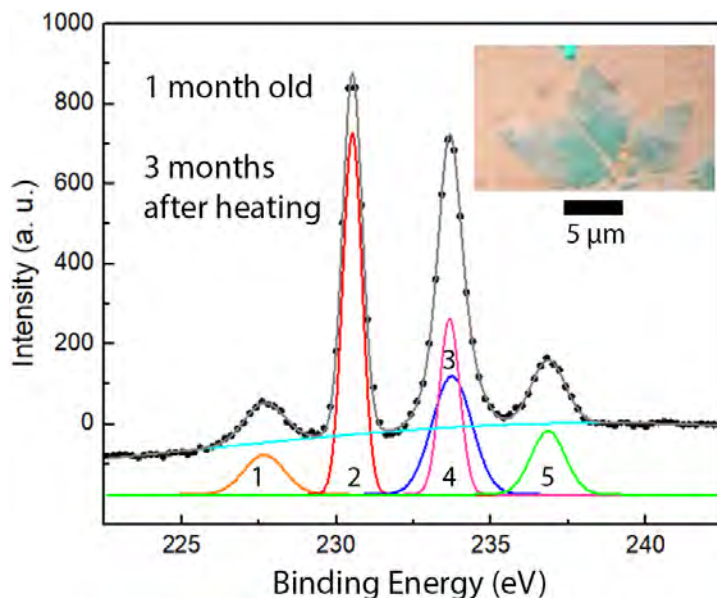
FIGURE 6.13. XPS spectra acquired over a $200 \times 200 \ \mu m^2$ area of the CVD grown MoS_2 film shown in Figure 6.3 (g) that was exposed to ambient air for 12.5 weeks. The solid circles are data points, and the solid gray curve is a fit using the 5 Lorentzian curves indicated 1–5. The inset shows a sample in the center of the acquisition area.

oxidized and bound to hydroxyl groups. The adsorbed H_2O then produces chemical reactions that dissolve the oxides. They concluded that the liquefied oxides cannot protect the edges from further oxidation, resulting in a self-propelled degradation process. In our case, we propose that the edges of the dendrites are oxidized. Water molecules diffusing on the surface reach the dendrites and produce reactions that dissolve the oxides. The liquid and dried products form the raised dendritic structures we observe. Zhang et al. [27] have reported needlelike protrusions in AFM images of the MoS_2 surface after submerging thick MoS_2 samples in water, which they attributed to $MoO_3 \cdot H_2O$ crystals. These protrusions are reported to be about 1.5 nm in height, similar in height to the dendrites we observe. In our case, $MoO_3 \cdot H_2O$ would originate from the surface H_2O molecules rather than from being underwater.

Another mechanism that has been reported to produce raised structures on MoS_2
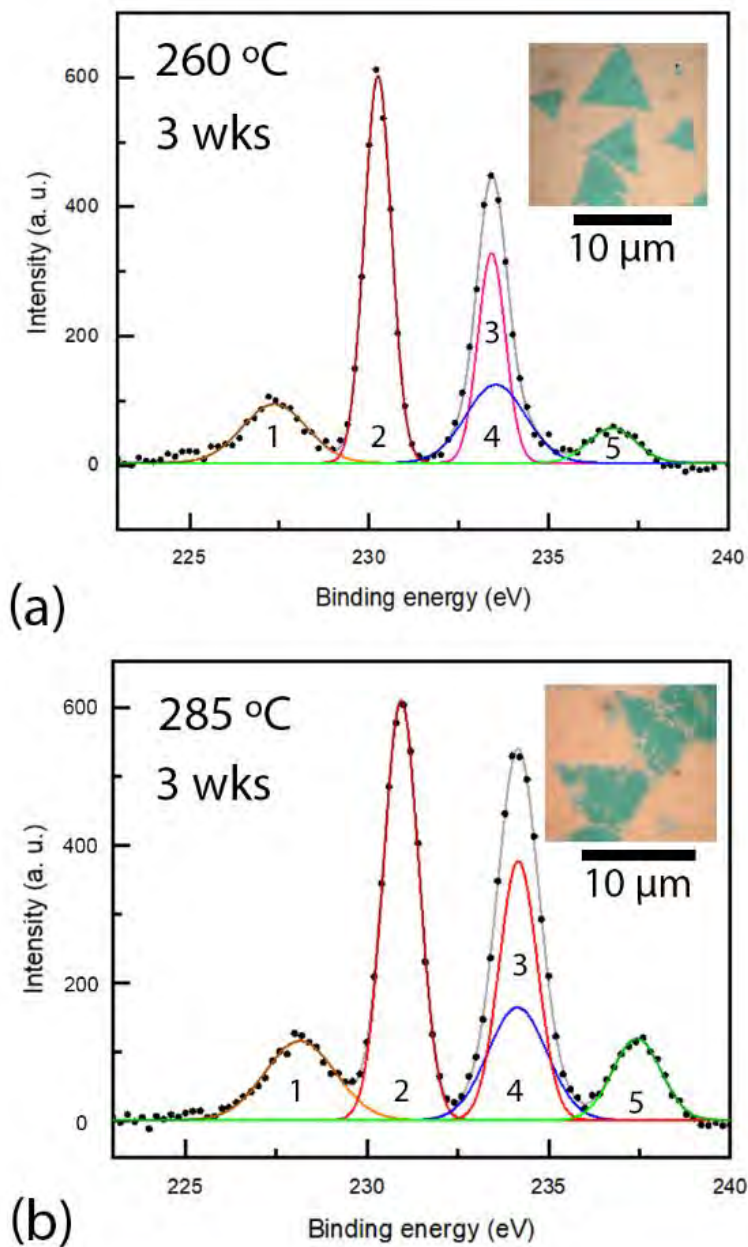
FIGURE 6.14. XPS spectra after background subtraction of samples exposed to ambient air for 3 weeks after heating in air for 2 h at (a) 260 °C and (b) 285 °C. As discussed in the text, the peak labels correspond to (1) S 2s, (2) Mo^{4+} $3d_{5/2}$, (3) Mo^{4+} $3d_{3/2}$, (4) Mo^{6+} $3d_{5/2}$, and (5) Mo^{6+} $3d_{3/2}$. The Mo^{6+} peaks correspond to MoO_3. The sample heated at 285 °C shows higher oxide peaks. The inset shows a sample in the center of the acquisition area.

monolayers is the intercalation of H_2O in the MoS_2–SiO_2 interface. Rauf et al. [24] have reported that MoS_2 exfoliated on mica, in the presence of about 11% relative humidity and absence of O_2, experiences a wetting effect in which H_2O intercalates in the MoS_2-mica interface from the edges of the flake within an hour. Their reported AFM images show an elevated labyrinth formation resembling the dendritic structures we observe. However, the labyrinths are reported to have a height of 1–3 Å, whereas the dendrites we observe have a height on the order of 2 nm. In addition, they observe the intercalation process within an hour, whereas we observe the degradation happening on the order of weeks. Rauf et al. [24] also reported the wetting effect initiating at the edges of the flake. Although we observe dendrites originating from the edges in some cases, as in Figures 6.3 and 6.6, we also observe them originating on the basal plane, as in Figures 6.1 and 6.9. In addition, the Raman maps show a decrease in the MoS_2 peak and increase in the Si peak in the dendritic areas. We conclude that our dendrites are due to degradation and not intercalated H_2O.

We explain the rapid degradation of preheated samples as follows. The DLA process is slow in the beginning but speeds up as more dendrites grow and there are more sites to which diffusing molecules can stick. The XPS results show an increase in MoO_3 after heating. We propose that heating introduces more oxidation sites to which the H_2O molecules can diffuse, so that the degradation process proceeds faster. Because the relative humidity of air at 330 °C is very low, it is likely that there is little H_2O on the surface during heating. This explains why we do not see large areas of reduced optical contrast associated with the presence of dendrites immediately after heating. However, when the sample is then left in air, H_2O can easily adsorb. Moreover, the monolayer may become more hydrophilic after heating. It has been reported that freshly exfoliated MoS_2 [28] and CVD grown WS_2 [29] monolayers are more hydrophilic than aged ones due to the absence of contaminants. Heating may clean the monolayer making it more hydrophilic. This mechanism could also explain why putting the sample in a dry box slows down the rapid degradation. If the sample were immediately placed in a dry box after heating, the surface would not adsorb any H_2O. MoO_3 has been reported to volatize at RT [30]. This evaporation of oxides may restore the sample to a less oxidized

state, so after the sample is brought to ambient air the degradation starts slowly from a less oxidized state rather than from an advanced oxidized state. The above explanation that the increased oxidation leads to rapid degradation is supported by our experiment (not shown) in which we heated a CVD grown MoS_2 monolayer at 330 °C in an atmosphere of He and flow rate of 140 sccm and then left the sample out in ambient air. In this case, there would be no additional oxidation due to heating. After 2.5 weeks, no dendrites were observed both optically and using AFM. We conclude that thermal annealing [15] or the use of other inert gasses such as Ar while heating will not produce rapid degradation [16]. We also exposed samples that were preheated at 330 °C for 2 h to ambient air in a dark enclosure and observed no degradation, like the results reported for long-term air exposure of unheated samples in a dark enclosure [4]. Therefore, the photo-induced process appears to also be necessary in our degradation process.

6.6. Conclusions

We observe a rapid degradation of CVD grown MoS_2 monolayers on SiO_2 under ambient air that occurs after about 2 weeks and is initiated by preheating the sample in air at temperatures as low as 285 °C. This result indicates that extra steps must be taken to passivate monolayer MoS_2 after exposure to a heated environment. We conclude that the vehicle for degradation is the growth of dendrites by diffusion limited aggregation. For a given monolayer, we found that dendrites originate only at the edges, or only the basal plane, or both the edges and the basal plane. We propose the following mechanism for the rapid degradation. Heating the sample in air forms more MoO_3 sites on the surface that makes the monolayer more hydrophilic. After the sample is placed in ambient air, H_2O molecules adsorb on the surface, where they diffuse to MoO_3 sites. According to a recently reported mechanism for the degradation of MoS_2 nanoparticles in ambient air, the adsorbed H_2O produces reactions that liquefy the oxides, allowing further oxidation of the sample to occur. We propose the reaction products take form of protrusions about 2 nm in height that result in the raised dendritic structures we observe. Leaving samples in a dry box for 2 weeks after heating prevents the rapid degradation from occurring in ambient air during

the month that the sample was observed. We propose that leaving a preheated sample in a dry box prevents H_2O from adsorbing and allows MoO_3 to volatize, thereby decreasing the amount of oxidation and slowing the degradation in ambient air. It appears that monolayer MoS_2 has the potential of being air stable if H_2O is prevented from diffusing on the surface. Future work could explore methods of minimizing H_2O adsorption and diffusion.

6.7. References

[1] Wang Q H, Kalantar-ZadehK, KisA, Coleman JN and Strano M S 2012 Electronics and optoelectronics of two-dimensional transition metal dichalcogenides Nat. Nanotechnol. 7699

[2] Gao J, Li B, Tan J, Chow P, Lu T M and Koratkar N 2016 Aging of transition metal dichalcogenide monolayers ACS Nano 10 2628–35

[3] Şar H, Özden A, Demiroğlu İ, Sevik C, Perkgoz N K and Ay F 2019 Long-term stability control of CVD-grown monolayer MoS_2. Phys. Status Solidi 13 1800687

[4] Kotsakidis J C, Zhang Q, de PargaA LV, Currie M, Helmerson K, Gaskill D K and Fuhrer M S 2019 Oxidation of monolayer MoS_2 in ambient is a photoinduced process Nano Lett. 19 5205–15

[5] Budania P, Baine P, Montgomery J, McGeough C, Cafolla T, Modreanu M, McNeill D, Mitchell N, Hughes G and Hurley P 2017 Long-term stability of mechanically exfoliated MoS_2 flakes MRS Commun. 7 813–8

[6] Martincová J, Otyepka M and Lazar P 2017 Is single layer MoS_2 stable in the air? Chem. Eur. J. 23 13233–9

[7] Wu J, Li H, Yin Z, Li H, Liu J, Cao X, Zhang Q and Zhang H 2013 Layer thinning and etching of mechanically exfoliated MoS_2 nanosheets by thermal annealing in air Small 9 3314–9

[8] Zhou H et al. 2013 Thickness-dependent patterning of MoS_2 sheets with well-oriented triangular pits by heating in air Nano Res. 6 703–11

[9] Park J, Kim M S, Cha E, Kim J and Choi W 2017 Synthesis of uniform single layer MoS_2 for tunable photoluminescence Sci. Rep. 7 16121

[10] Castellanos-Gomez A, Barkelid M, Goossens A M, Calado V E, van der Zant H S and Steele G A 2012 Laser-thinning of MoS_2: on demand generation of a single-layer semiconductor Nano Lett. 12 3187–92

[11] Rao R, Islam A E, Campbell P M, Vogel E M and Maruyama B 2017 In situ thermal oxidation kinetics in few layer MoS_2. 2D Mater. 4 025058

[12] Rong Y, He K, Pacios M, Robertson A W, Bhaskaran H and Warner J H 2015 Controlled preferential oxidation of grain boundaries in monolayer tungsten disulfide for direct optical imaging ACS Nano 9 3695–703

[13] Kim Y, Huang J L and Lieber C M 1991 Characterization of nanometer scale wear and oxidation of transition metal dichalcogenide lubricants by atomic force microscopy Appl. Phys. Lett. 59 3404–6

[14] Lu J, Carvalho A, Chan X K, Liu H, Liu B, Tok E S, Loh K P, Castro Neto A H and Sow C H 2015 Atomic healing of defects in transition metal dichalcogenides Nano Lett. 15 3524–32

[15] Zhao H Q, Mao X, Zhou D, Feng S, Shi X, Ma Y, Wei X and Mao Y 2016 Bandgap modulation of MoS_2 monolayer by thermal annealing and quick cooling Nanoscale 8 18995–9003

[16] Nie C, Yu L, Wei X, Shen J, Lu W, Chen W, Feng S and Shi H 2017 Ultrafast growth of large-area monolayer MoS_2 film via gold foil assistant CVD for a highly sensitive photodetector Nanotechnology 28 275203

[17] Jiang Y, Yuankun L, Cui J and Philipose U 2018 Effects of strategically placed water droplets on monolayer growth of molybdenum disulfide J. Nanomater. 2018 6192532

[18] Oh H M, Han G H, Kim H and Jeong M S 2016 Influence of residual promoter to photoluminescence of CVD grown MoS_2 Curr. Appl. Phys. 16 1223–8

[19] Kim H, Kim W, Orsquo;Brien M, McEvoy N, Yim C, Marcia M, Hauke F, Hirsch A, Kim G T and Duesberg G S 2018 Optimized single-layer MoS_2 field-effect transistors by noncovalent functionalisation Nanoscale 10 17557–66

[20] Yamamoto M, Einstein T L, Fuhrer M S and Cullen W G 2013 Anisotropic etching of atomically thin MoS_2. J. Phys. Chem. C 117 25643–9

[21] Liebovitch L S and Toth T 1989 A fast algorithm to determine fractal dimensions by box counting Phys. Lett. A 141 386–90

[22] Fractalyse Analysis Software 2017

[23] WittenTA Jr and Sander LM 1981 Diffusion-limited aggregation, a kinetic critical phenomenonPhys. Rev. Lett. 471400

[24] Rauf A, Schilo A, Severin N, Sokolov I M and Rabe J P 2018 Non-monotonous wetting of graphene–mica and MoS_2 -mica interfaces with a molecular layer of water Langmuir 34 15228–37

[25] Kim H J, Kim D, Jung S, Bae M H, Yun Y J, Yi S N, Yu J S, Kim J H and Ha D H 2018 Changes in the Raman spectra of monolayer MoS_2 upon thermal annealing J. Raman Spectrosc. 49 1938–44

[26] Afanasiev P and Lorentz C 2019 Oxidation of nanodispersed MoS_2 in ambient air: the products and the mechanistic steps J. Phys. Chem. C 123 7486–94

[27] Zhang X, Jia F, Yang B and Song S 2017 Oxidation of molybdenum disulfide sheet in water under in situ atomic force microscopy observation J. Phys. Chem. C 121 9938–43

[28] Kozbial A, Gong X, Liu H and Li L 2015 Understanding the intrinsic water wettability of molybdenum disulfide (MoS_2) Langmuir 31 8429–35

[29] Chow P K et al. 2015 Wetting of mono and few-layered MoS_2 and MoS_2 films supported on Si/SiO_2 substrates ACS Nano 9 3023–31.

[30] Spychalski W L, Pisarek M and Szoszkiewicz R 2017 Microscale insight into oxidation of single MoS_2 crystals in air J. Phys. Chem. C 121 26027–33

[31] Förster, T., 1967. Mechanisms of energy transfer. Comprehensive biochemistry 22, 61-80.

[32] Lanzillo, N.A., Glen Birdwell, A., Amani, M., Crowne, F.J., Shah, P.B., Najmaei, S., Liu, Z., Ajayan, P.M., Lou, J., Dubey, M. and Nayak, S.K., 2013. Temperature-

dependent phonon shifts in monolayer MoS_2. Applied Physics Letters, 103(9), 093102.

[33] Kang, K.; Xie, S.; Huang, L.; Han, Y.; Huang, P. Y.; Mak, K. F.; Kim, C.-J.; Muller, D.; Park, J. High-Mobility Three-Atom-Thick Semiconducting Films with Wafer-Scale Homogeneity. Nature 2015, 520, 656660.

[34] Kim, H.; Ovchinnikov, D.; Deiana, D.; Unuchek, D.; Kis, A. Suppressing Nucleation in Metal-Organic Chemical Vapor Deposition of MoS_2 Monolayers by Alkali Metal Halides. Nano Lett. 2017, 17, 50565063.

CHAPTER 7

LONG-TERM STABILITY OF BILAYER MoS$_2$ IN AMBIENT AIR

7.1. Background

Bilayer (BL) and thicker-layered transition metal dichalcogenides (TMDs) have been shown to have advantages over monolayer (ML) TMDs in device applications due to multilayer TMDs having higher electrical conductivities. The higher conductivity is due to a higher density of states (DOS) and more effective screening of charged impurities in the substrate. Multilayer TMDs have excellent combination of on/off current ratio and on-state current [35]. Monolayer TMDs, on the other hand, although possessing greater on/off current ratios, have a relatively small on-state current. To our knowledge, there have not been any studies on the air stability of these properties of multilayer TMD devices. In this dissertation, we investigate the stability of bilayer and thicker-layered TMD, which could catalyze research on realizing new heterostructure devices that are more efficient, stable, and reliable for commercial applications. We found that bilayer and thicker-layered MoS$_2$ are stable in ambient air. This is remarkable given that water vapor, oxygen and light were present. One possible explanation for the stability is that the indirect band gap of bilayer and thicker-layered MoS$_2$ quenches the Förster resonance energy transfer (FRET) mechanism. That is, the photoexcited carriers in the conduction band of the bilayer and thicker-layered MoS$_2$ samples decay by phonon relaxation, instead of emission of a virtual photon. Other possible explanations are that the interlayer coupling between layers may reduce their reactivity. The proposed FRET process involves energy transfer from photoexcited excitons to O$_2$ molecules resulting in the production of singlet O$_2$, denoted spectroscopically by $^1\Delta_g$, which is a highly reactive oxygen species (ROS) capable of degrading TMDs. The steps in a FRET process involve photoexcitation of a photosensitizer to the singlet S_1 state, quenching of the S_1 state to the triplet T_1 state by O$_2$ molecules in the $3\,\Sigma_g^-$ triplet ground state, and quenching of the T_1 state by other O$_2$ molecules in the state. As a by-product, O$_2$ in the $^1\Delta_g$ singlet state is produced. These steps involve direct transitions across the band gap and thus proceed at

a faster rate in a direct band gap semiconductor such as ML TMDs.

7.2. Abstract

We report that chemical vapor deposition (CVD) grown bilayer and thicker-layered MoS_2 are structurally and optically stable under ambient conditions, in comparison to CVD-grown monolayer MoS_2 and other transition metal dichalcogenides (TMDs) that have been reported to degrade under the same conditions, hindering their many potential applications. We present atomic force microscopy (AFM), and Raman and photoluminescence (PL) spectroscopy measurements of as grown and preheated multilayer MoS_2 after exposure to ambient conditions for periods of up to 2 years. The AFM images show that, under ambient conditions, as-grown and preheated bilayer and thicker-layered MoS_2 films do not exhibit the growth of dendrites that is characteristic of monolayer degradation. Dendrites are observed to stop at the monolayer-bilayer boundary. Raman and PL spectra of the aged bilayer and thicker-layered films are comparable to those of as-grown films. The greater stability of bilayers and thicker layers supports a previously reported mechanism for monolayer degradation involving Förster resonance energy transfer. Our results show that bilayer and thicker-layered TMDs are promising materials for applications requiring ambient stability.

7.3. Introduction

Two-dimensional (2D) materials have attracted considerable interest due to their unique properties that have potential applications in a wide variety of areas. However, most of the discovered 2D materials quickly degrade under ambient conditions [1], significantly impeding their use in practical devices. For example, monolayer (ML) MoS_2 is a transition metal dichalcogenide (TMD) that may have unique applications due to its direct bandgap and large spin-orbit coupling [2]. However, previous reports have shown that chemical vapor deposition (CVD)-grown ML MoS_2 and other ML TMDs degrade under ambient conditions within a year [3–7]. Despite the variety of degradation prevention techniques such as encapsulation with hexagonal boron nitride [8] and polymers [9], and placement in an environment with a desiccant [3] or in a vacuum [5], these techniques are not feasible for large-scale ap-

plications. To our knowledge, the stability of bilayer (BL) and thicker-layered MoS_2 under ambient conditions has not been extensively studied. In this paper, we report on the stability of as-grown and preheated BL and thicker-layered MoS_2. The samples are grown using CVD on SiO_2 substrates and studied using atomic force microscopy (AFM), and Raman and photoluminescence (PL) spectroscopies. Samples are preheated to accelerate the degradation process to study it in a practical short time span. We find that BL and thicker-layered samples are remarkably stable under ambient conditions.

Bilayer and thicker-layered MoS_2 films, although possessing an indirect bandgap, have attracted considerable interest because of useful electronic properties not possessed by MoS_2 MLs. These properties give BLs and thicker layers certain advantages over MLs in the fabrication of electronic and photonic devices. For example, they have high electrical conductivity as compared to MLs due to their high density of states and effective screening of impurities in the substrate. Multilayer TMD transistors have been shown to have an excellent combination of high on/off current ratio and on-state current [10]. On the other hand, ML TMDs have a relatively small on-state current despite possessing greater on/off current ratios. In addition, BL device yield is typically much higher than ML device yield, due to the greater mechanical stiffness of BLs [11, 12]. Finally, BL and thicker-layered TMDs offer control over properties such as spin-orbit coupling [13], interlayer coupling [14], and band gap [15]. This ability to precisely tune the physical and electronic properties of atomically thin TMDs have potential applications in novel lateral heterostructures [15–17]. Also, varying the twist angle between layers in BLs can lead to new and potentially useful properties such as unconventional superconductivity at small twist angles [18], twist dependent valley and band alignment [19], and moiré pattern excitons [20].

The ambient degradation of CVD-grown ML MoS_2 was first reported by Gao et al. [3]. They observed that ML MoS_2 and WS_2 grown on SiO_2 substrates developed extensive cracking, morphological changes, and quenching of photoluminescence (PL) after exposure to an ambient environment at room temperature (RT) for a period of about a year. The degradation was attributed to oxidation along the grain boundaries and the adsorption of
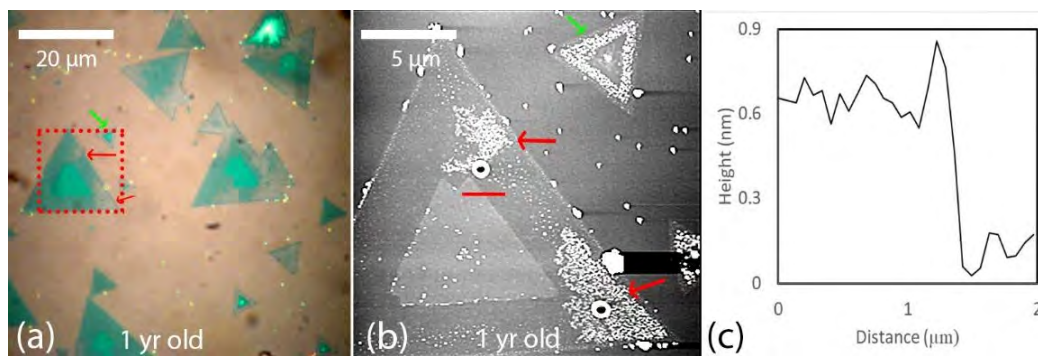
FIGURE 7.1. (a) Optical image of an MoS_2 monolayer and bilayer after about 1 year of exposure to ambient conditions. The arrows indicate areas of light optical contrast on the monolayer that are degraded. (b) AFM image of the boxed region in (a). (c) AFM height profile along the line in (b). The height of the inner MoS_2 island is about 0.6 nm corresponding to a bilayer.

organic contaminants on the films. It was found that water vapor in the air was necessary for degradation to occur since samples did not degrade in a dry box. In addition, there have been reports of MoS_2 degradation at RT and high humidities [5, 21]. For instance, Budania et al. [5] reported that mechanically exfoliated thin multilayer MoS_2 on SiO_2 developed speckles in air at a relative humidity (RH) of 60% over a period of about a year [5], which was attributed to the high concentration of water molecules in the air. Sar et al. [7] studied the degradation process of CVD-grown ML MoS_2 grown using two different sample positions and found that face-down grown samples developed cracks and degraded significantly as compared to horizontally grown samples. It was concluded that the degradation process was a result of sulfur vacancy defects and film tensile stress that were affected by the growth conditions. In addition, Kotsakidis et al. [4] reported that the degradation of ML MoS_2 and other TMDs in air was a photoinduced process involving excitation across the band gap, since degradation was not observed when samples under ambient conditions were kept in a dark environment or excited at photon energies below the trion exciton binding energy [4]. It was proposed that the degradation mechanism involved photo-oxidation, likely Förster resonance energy transfer (FRET) and/or photocatalysis.

In addition, we have recently reported a rapid ambient degradation of CVD-grown ML MoS_2 that occurs over a period of weeks instead of a year after the MLs are preheated in air at temperatures in the range 285 - 330 °C [6]. Both rapid degradation and natural degradation (in which samples are not preheated) were observed to involve the formation of dendritic structures, and thus it was proposed that rapid and natural degradation involve a similar mechanism [6]. The rapid degradation of preheated samples was attributed to an increase in oxidized sites due to the preheating. Finally, Qiu et al. [22] reported the degradation of the electrical properties of exfoliated BL MoS_2 field effect transistors from exposure to ambient air. The authors showed that after vacuum annealing at 77 °C the electrical properties of as-fabricated devices significantly improved; five minutes after re-exposure to an oxygen environment, the electrical properties degraded. The degradation was found to be reversible upon annealing and attributed to the physisorption of oxygen and water. The effects of long-term exposure on the stability of the MoS_2 was not reported. We note that the degradation of ML TMDs involves morphological changes that occur over a long time and are not reversible. Thus, it is of vital importance to investigate if BL and thicker-layer MoS_2 is susceptible to degradation.

7.4. Results and Discussion

Figure 7.1 (a) shows an optical image of an MoS_2 BL sample with an AA stacking sequence that was kept under ambient conditions for approximately one year after growth. In this paper, ambient conditions refer to air at RT and a RH of about 43%, and room lighting of about 1000 Lux that is typical of a lab. The image in Figure 7.1 (a) shows various BL MoS_2 islands with ML terraces. Figure 7.1 (b) is an AFM image of the boxed region in Figure 7.1 (a). Figure 7.1 (c) shows an AFM height profile along the line in Figure 7.1 (b) showing a step height of about 0.6 nm consistent with that of a BL [23]. As indicated by the red arrows in Figure 7.1 (a), the ML terrace shows areas of light optical contrast that have been previously reported to be due to degradation [3]. Figure 7.1 (b) shows that the areas of light contrast contain dendrites. We note that the dendrites grow over the ML but are not present in the BL region. Also, it is noted that the small multilayer island on the top

126
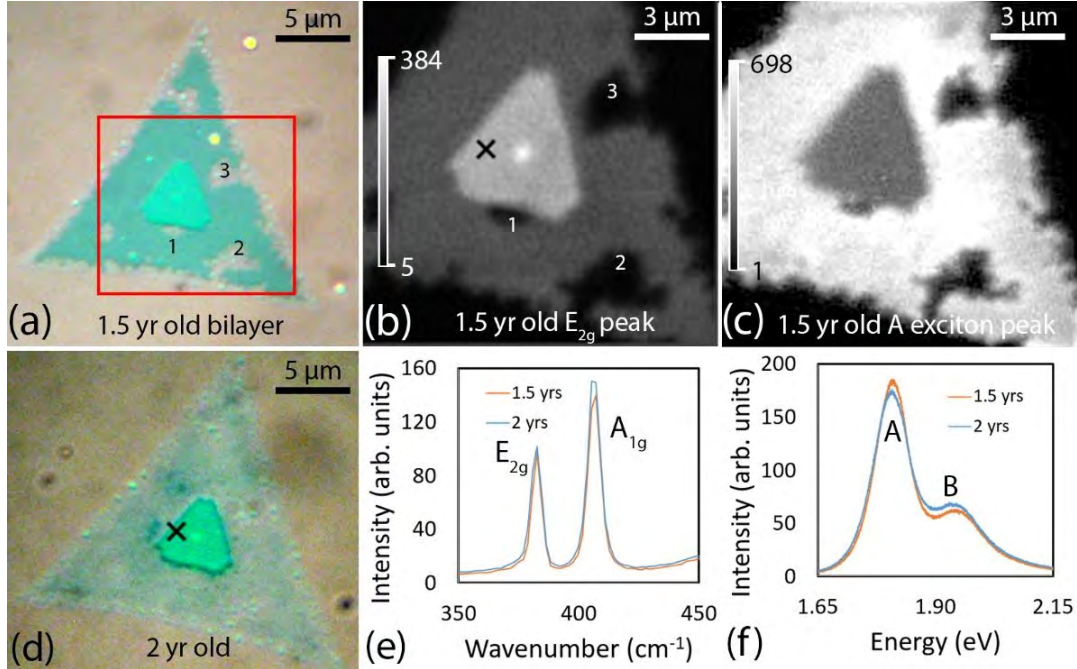
FIGURE 7.2. (a) Optical image of an MoS_2 monolayer with an AA-stacked bilayer after about 1.5 years of exposure to ambient conditions. The light optically contrasted areas on the monolayer, indicated by the numbers 1-3, show degradation. (b) and (c) Raman and photoluminescence maps of the area enclosed by the box in (a), showing the relative heights of the E_{2g} and the A exciton peaks, respectively. (d) Optical image of the sample shown in (a) after 2.0 years of exposure to ambient conditions. The monolayer has almost completely degraded. (e) Raman spectra taken at the location of the cross in (b) and (d) after 1.5 and 2.0 years of exposure to ambient conditions. (f) Photoluminescence spectra taken at the location of the cross in (b) and (d) after 1.5 and 2.0 years of exposure to ambient conditions.

right-hand-side, indicated by the green arrow, has dendrites consuming the entire ML, but there are no such dendrites in the multilayer region of the island. This effect is widespread across the substrate. Almost all MLs on the 1.5-year-old substrate showed dendritic growths while BLs were unaffected, as shown in Figure 7.7. The degradation is irreversible, as shown in Figure 7.8 in which we vacuum annealed a sample at 500 °C for 2 h but the dendrites

remained.

We also performed Raman and PL mapping of BL MoS$_2$ samples that had been under ambient conditions for approximately 1.5 years. We did not perform Raman or PL mapping immediately after growth to avoid effects of laser irradiation, which has been reported to degrade ML WS$_2$ [4]. Figure 7.2 (a) shows an optical image of such a sample. The same regions of light optical contrast, which are attributed to degradation, are observed around the edges, and growing into the ML. Various degraded areas in the ML are marked with numbers to assist in locating the areas in other figures. We note that there is an area of the ML that is adjacent to the BL, indicated by the number 1, that is degraded, but the adjacent BL appears unaffected. Figure 7.2 (b) shows a Raman map of the same sample depicting the relative height of the E$_{2g}$ peak at 382 cm^{-1}. The dark and light regions correspond to low and high peak heights, respectively. The E$_{2g}$ peak height from areas of the ML that have a light optical contrast in Figure 7.2 (a) is lower than that from areas of the ML that have a normal optical contrast. This effect has been previously attributed to the light-contrast areas being degraded [3]. However, the E$_{2g}$ and A$_{1g}$ peak height in the BL region appear uniform with no observable areas of reduced height that could indicate degradation. Figures 7.9 (a)-(f) show maps of the fitted peak height, position, and width of the E$_{2g}$ and A$_{1g}$ Raman peaks. This conclusion is further supported by the PL map of the A exciton peak centered at around 1.80 eV, shown in Figure 7.2 (c), which shows a spatially uniform height across the BL. The BL region exhibits a less intense PL as compared to the ML, as expected, due to BLs having an indirect band gap [3]. On the other hand, degraded ML regions exhibit decreased heights in the exciton peaks, consistent with previous reports [3]. In addition to an intensity decrease, we find that the A exciton peak of degraded MLs also shifts to higher energy by about 0.5 eV, as shown in Figure 7.10.

To determine if the Raman and PL spectra significantly change after additional exposure, we collected data on the same sample after an additional 0.5 years in ambient conditions for a total exposure of 2.0 years. Figure 7.2 (d) shows an optical image of the sample after 2.0 years showing that the ML has completely degraded but the BL still contains no observ-

able regions of degradation. Figure 7.2 (e) shows representative Raman spectra of the BL taken at the location of the cross in Figure 7.2 (b) after 1.5 and 2.0 years. Figure 7.2 (e) shows representative PL spectra of the BL taken at the location of the cross in Figure 7.2 (b) after 1.5 and 2.0 years. The height of the PL spectra is normalized to their Si Raman peak at about 520 cm^{-1}. The fitted positions and full-width-at-half maxima (FWHM) of the Raman E_{2g} and A_{1g} peaks for both the 1.5 and 2.0-year-old samples are 382 cm^{-1}, 406 cm^{-1}, 4.9 cm^{-1} and 6.5 cm^{-1}, respectively. The B and A exciton peaks for the 1.5-year-old sample are centered at, 1.95 eV and 1.80 eV, respectively, and the B and A exciton peaks for the 2-year-old sample are centered at 1.94 eV and 1.80 eV, respectively. The PL heights are also very comparable to each other. Our results for aged BLs are similar to previously published results on as-grown BLs: the center of the E_{2g} peak and A_{1g} peak of as-grown BLs have been reported to be around 381-382 cm^{-1} and 404-405 cm^{-1}, respectively [24], and the FWHM has been reported to be around 4.8-5.8 cm^{-1} for the E_{2g} peak and 5.8-6.7 cm^{-1} for the A_{1g} peak [25]. We conclude that the Raman and PL spectra of the BL has not undergone significant change during this time. To study the stability of BLs and thicker layers in a practical time span of less than a year, we put samples through the accelerated degradation process [6]. Figures 7.3 (a) and (b) show optical and AFM images, respectively, of an MoS$_2$ multilayer grown a month prior consisting of more than 4 layers forming a pyramidal structure. Figure 7.3 (c) shows an AFM height profile along the line in Figure 7.3 (b). The height of the second MoS$_2$ layer is about 0.6 nm, which agrees with the value for the ML-to-BL height difference [23]. In addition, the height of the third MoS$_2$ layer is also about 0.6 nm. This multilayer structure has the advantage of allowing a comparison of degradation, under the same conditions, as a function of number of layers.

To investigate how BLs and thicker layers degrade given direct edge exposure to the SiO$_2$ substrate, we introduced a scratch on the left-hand side of the sample using the AFM cantilever. Figures 7.3 (d) and (e) show optical and AFM images, respectively, of the sample after the AFM cantilever was used to create the scratch, which is indicated by the arrow in Figure 7.3 (d). Figure 7.3 (f) shows an optical image of the MoS$_2$ structure immediately
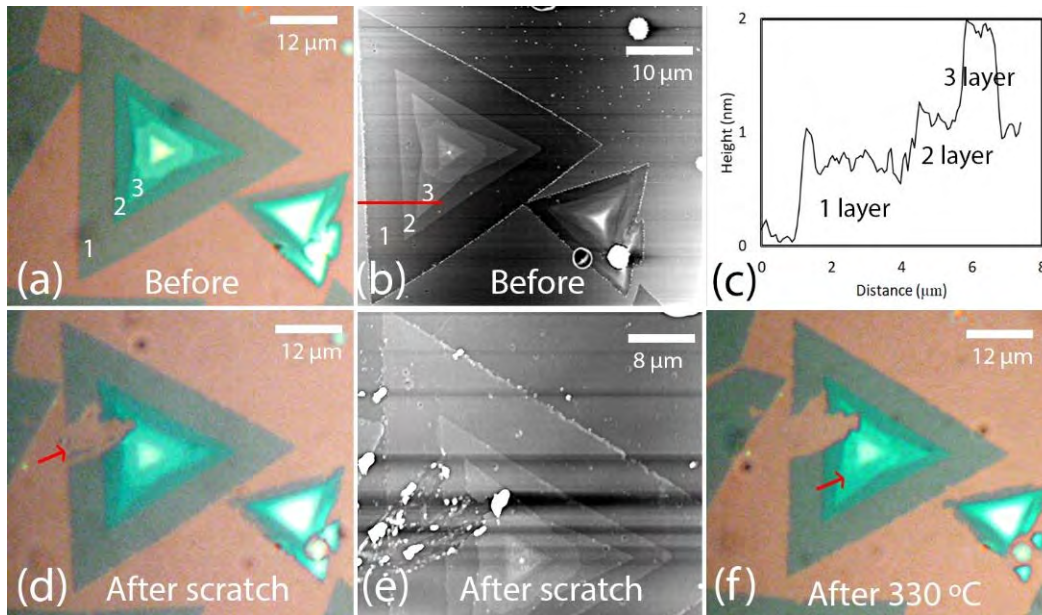
FIGURE 7.3. (a) and (b) Optical and AFM images, respectively, of an MoS_2 multilayer sample grown a month prior. The numbers 1, 2 and 3 denote monolayer, bilayer and trilayer, respectively. (c) AFM height profile along the red line in (b). The height of the second MoS_2 island is about 0.6 nm, and the height of the third MoS_2 island is about 0.6 nm, corresponding to a bilayer and trilayer, respectively. (d) and (e) Optical and AFM images, respectively, of the same sample after the AFM tip was used to create a scratch indicated by the arrow in (d). (f) Optical image of the MoS_2 sample after heating in air at 330 °C for 2 h. Etch pits are visible on the fourth layer, as indicated by the arrow.

after preheating in air at 330 °C for 2 h. While the basal plane of the BL does not appear to have been significantly affected by the preheating, the fourth layer appears to show etch pits, as indicated by the arrow in Figure 7.3 (f). This is consistent with previous reports that have shown that thick-layer MoS_2 starts to develop etch pits at lower temperatures than thin-layer MoS_2 [26]. This behavior is in contrast with that of graphene in which the ML develops etch pits at lower temperatures than thicker layers [27].

After preheating, the MoS_2 sample was left under ambient conditions. Figures 7.4

130

FIGURE 7.4. (a)-(c) Optical and AFM images of the MoS_2 multilayer sample shown in Figure 7.3 after 2.5 weeks of exposure to ambient conditions. Dendrites have started to develop on the monolayer, but not on the bilayer and thicker layers. The arrow in (c) indicates the fourth layer that has developed etch pits. (d-f) Optical and AFM images of the sample after 9 weeks of exposure to ambient conditions. (g-i) Optical and AFM images of the sample after 15 weeks of exposure to ambient conditions.

(a) and (b) show optical and AFM images, respectively, of the sample after 2.5 weeks of exposure to ambient conditions. There are regions of light optical contrast developing on the edges of the ML that correspond to raised dendritic regions in the AFM image. These observations are consistent with our previous report on the rapid degradation of MoS_2 MLs after preheating [6]. We note that dendrites are growing from the scratch edge into the ML,

131

and have covered the entire width of the edge of the ML. However, despite the BL and thicker layers being exposed to both the substrate and the dendrites on the ML, there are no visible dendritic growths on the BL or thicker layers. Figure 7.4 (c) shows a high-resolution AFM image of the sample confirming the existence of etch pits on the fourth layer, as indicated by the red arrow, which was inferred from the optical image shown in Figure 7.3 (e). There are also less noticeable etch pits on layers thicker than four. Figures 7.4 (d) and (e) show optical and AFM images, respectively, of the sample after 9 weeks under ambient conditions. Figure 7.4 (f) shows a high-resolution AFM image showing that the etch pits have not changed, whereas the dendrites on the ML have grown across the entire width of the ML and have stopped at the ML-BL boundary. Figures 7.4 (g) and (h) show optical and AFM images, respectively, of the sample after 15 weeks of exposure to ambient conditions. Figure 7.4 (i) shows a high-resolution AFM image after 15 weeks showing that the dendrites have spread over the ML but stopped at the BL. In addition, the fourth layer containing etch pits has not significantly changed in the last 2.5 weeks after heating. The structural stability of preheated BLs and thicker layers was observed in the hundreds of samples and substrates that we studied, examples of which are shown in Figure 7.11.

We also studied the sample using Raman and PL spectroscopies. Figure 7.5 (a) shows an AFM image of the sample after 42.5 weeks of exposure to ambient conditions. Figures 7.5 (b) and (c) show maps of the E_{2g} and the A exciton peaks, respectively, after 42.5 weeks of exposure to ambient conditions. The same numbers in Figures 7.5 (a-c) indicate the same sample regions. As was the case in the sample shown in Figure 7.2, the ML regions with dendrites have very weak E_{2g} and A exciton peaks. The ML region indicated by the number 1 has not yet degraded. This region also has a very large PL response, as shown in Figure 7.5 (c). The E_{2g} and A exciton heights appear very uniform across the BL and thicker layers, except for several large circular regions of lower height, as indicated by the arrow in Figure 7.5 (b). The circular regions also appear in the AFM image after 42.5 weeks, as indicated by the arrow in Figure 7.5 (a). These circular regions are first observed in AFM images after 18 weeks of exposure, as shown in Figure 7.12. These circular regions were not observed in the
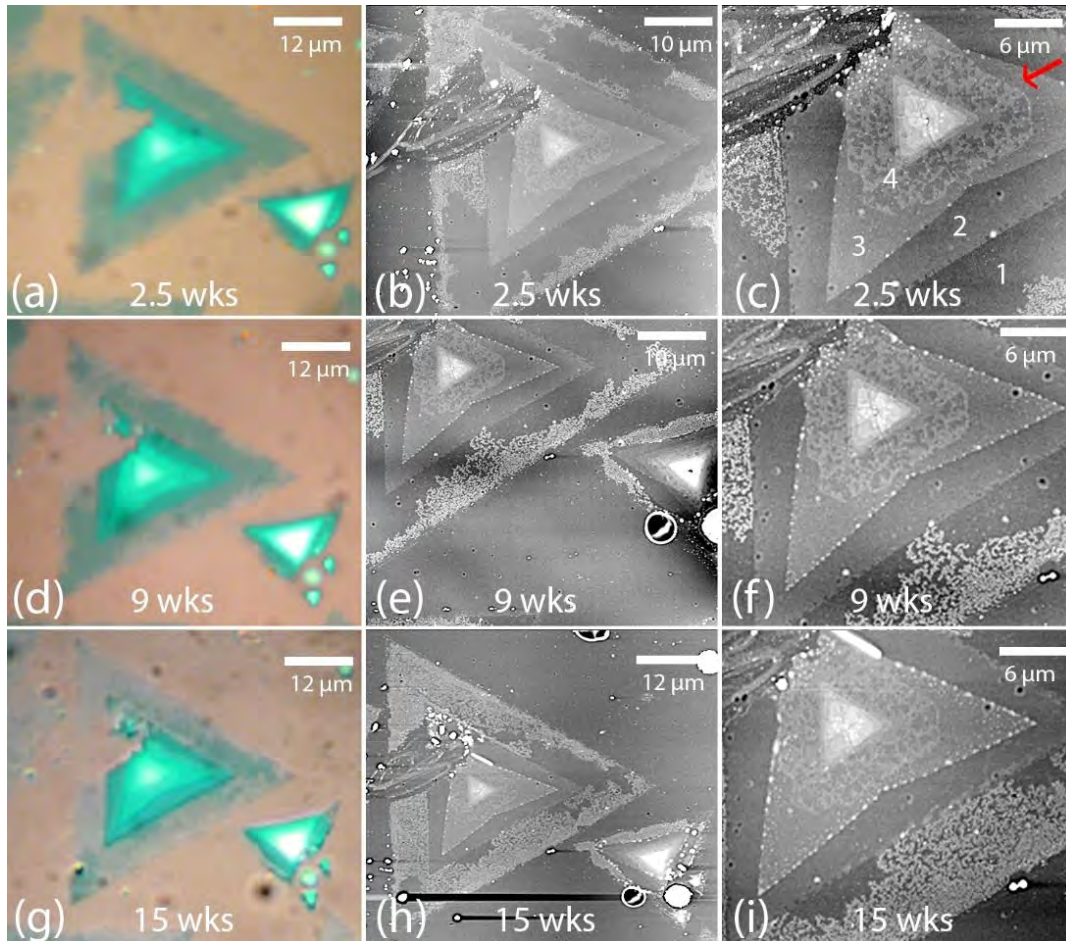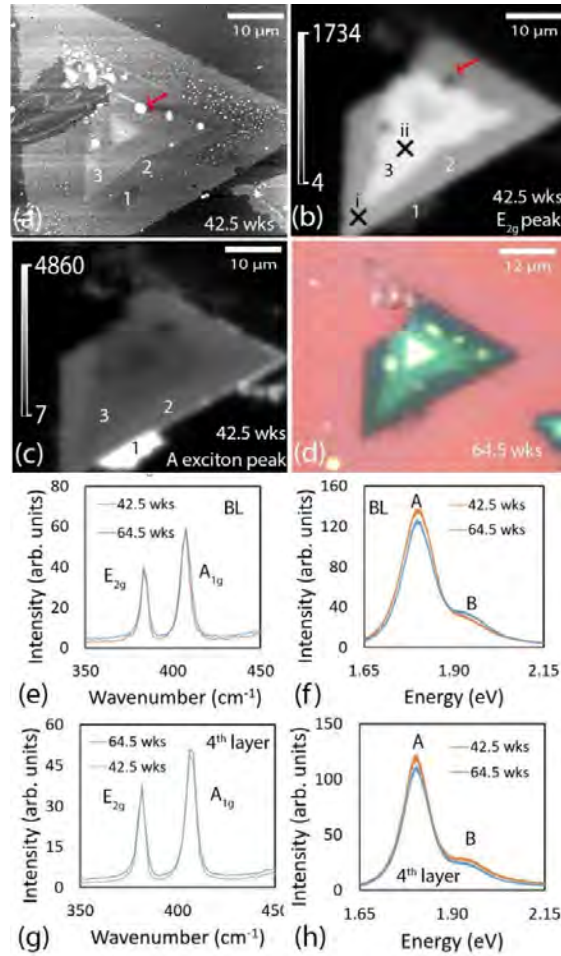
FIGURE 7.5. (a) AFM image of the multilayer sample shown in Figure 7.4 after 42.5 weeks of exposure to ambient conditions. The numbers 1, 2 and 3 indicate monolayer, bilayer and trilayer regions, respectively. (b) and (c) Raman and photoluminescence maps of the sample showing the relative heights of the E_{2g} and the A exciton peaks, respectively. (d) Optical image of the sample after 64.5 weeks of exposure to ambient conditions. (e) and (f) Raman and photoluminescence spectra, respectively, of the bilayer taken at the location of the cross labeled "i" in (b) after 42.5 and 64.5 weeks of exposure to ambient conditions. (g) and (h) Raman and photoluminescence spectra, respectively, of the fourth layer taken at the location of the cross labeled "ii" in (b) after 42.5 and 64.5 weeks of exposure to ambient conditions.

133
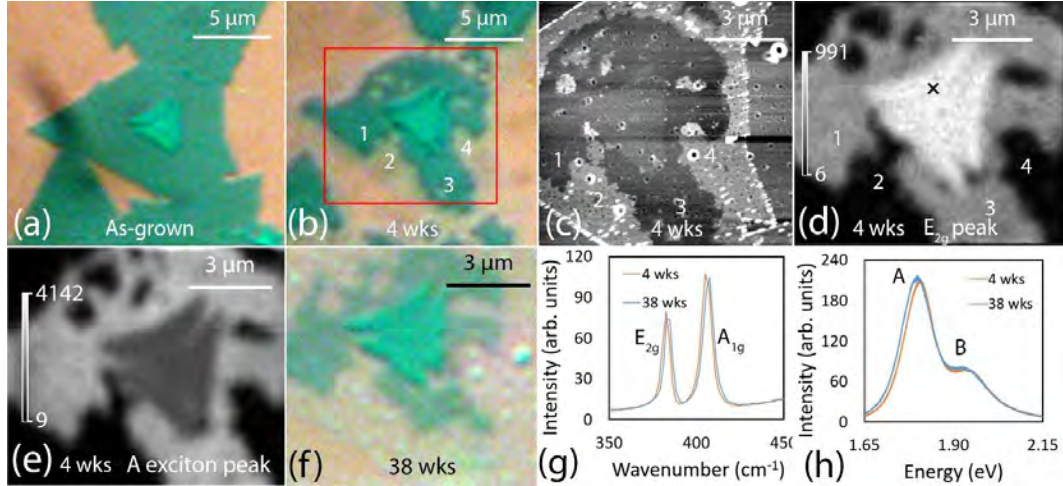
FIGURE 7.6. (a) Optical image of an MoS_2 bilayer 1 week after growth. (b) and (c) Optical and AFM images, respectively, of the sample after it was preheated in air at 330 °C for 2 h and then left under ambient conditions for 4 weeks. The AFM image is of the boxed region in (b). (d) and (e) Raman and photoluminescence maps of the sample, showing the relative heights of the E_{2g} and the A exciton peaks, respectively. (f) Optical image of the sample after 38 weeks of exposure to ambient conditions. (g) and (h) Raman and photoluminescence spectra, respectively, of the bilayer taken at the location of the cross in (d) after 4 and 38 weeks of exposure to ambient conditions.

AFM images in Figures 7.4 (h) and (i) that were taken after 15 weeks of exposure. We note from the AFM images that the size of these circular regions does not change significantly between 18 and 42.5 weeks. The appearance of these regions in less than 3 weeks and their unchanging size lead us to conclude that they are not caused by degradation, but rather by contaminants, either from ambient exposure or from deposition of material by the AFM tip. As shown in Figure 7.13, maps of fitted peak heights, positions, and widths of the E_{2g} and A_{1g} peaks show that in the circular regions the E_{2g} position shifts to lower wavenumbers by as much as 1.1 cm^{-1} and the FWHM increases by as much as 2.3 cm^{-1}, while the A_{1g} peak position and width remains like the surrounding layers. It has been reported that strain causes the E_{2g} peak position to decrease and its FWHM to increase, while not significantly

134

affecting the position or width of the A_{1g} peak [28]. The contaminants may be applying strain to the MoS_2, causing shifts, and broadening in the E_{2g} peak.

To determine if the Raman and PL spectra significantly change after continued exposure to ambient conditions, we took spectra after an additional 22 weeks of exposure for a total exposure of 64.5 weeks. Figure 7.5 (d) shows an optical image after 64.5 weeks of exposure. Figures 7.5 (e) and 7.5 (f) show Raman and PL spectra, respectively of the BL region taken at the location of the cross labeled by the letter "i" in Figure 7.5 (b) after 42.5 and 64.5 weeks of exposure. The fitted E_{2g} and A_{1g} peaks of both the 42.5-week and 64.5-week exposed samples are centered at about 382 cm^{-1} and 405 cm^{-1}, respectively, and have a FWHM of 5.2 cm^{-1} and 6.7 cm^{-1}, respectively. In addition, the B and A exciton peaks of both the 42.5 and 64.5-week-old sample are centered at around 1.94 eV and 1.80 eV, respectively. Figures 7.5 (g) and (h) show Raman and PL spectra, respectively of the fourth-layer region taken at the location of the cross labeled by the letters "ii" in Figure 7.5 (b) after 42.5 and 64.5 weeks of exposure. The fourth layer has the E_{2g} and A_{1g} peaks, and the B and A exciton peaks at about 381 cm^{-1}, 407 cm^{-1}, 1.90 eV, and 1.78 eV, respectively. These values agree with those reported in the literature for as-grown samples [24, 25]. These results provide an overview of the various effects that occur due to preheating MoS_2 based on the thickness of the sample. Monolayers degrade under ambient conditions, while BLs and thicker layers degrade significantly less with thicker layers more prone to develop etch pits during preheating.

We also studied preheated BLs with a negligible thicker multilayer on top. The objective was to determine if the thicker layers above the BL in the multilayer sample in Figure 7.5 contributed to its stability. Figure 7.6 (a) shows an optical image of the as-grown sample. The sample was then preheated at 285 °C for 2 h and exposed to ambient conditions. Figures 7.6 (b) and (c) show optical and AFM images, respectively, of the sample after 4 weeks of exposure. Dendrites have started growing on the ML and have stopped at the BL. Figures 7.6 (d) and (e) show height maps of the E_{2g} and A exciton peaks, respectively. Degraded regions on the ML have lower Raman and PL heights, but the BL remains very

uniform in height, even though this BL sample contains grain boundaries. Figure 7.14 shows fitted peak maps of the E_{2g} and A_{1g} peaks, showing very uniform position, width, and height over the BL. To study the effects of continued exposure to ambient conditions, we collected spectra after an additional 34 weeks of exposure. Figure 7.6 (f) shows an optical image of the sample after a total of 38 weeks in ambient conditions. Figure 7.6 (g) shows Raman spectra collected at the location of the black cross in Figure 7.6 (d) after 4 weeks and 38 weeks of air exposure. The fitted positions of the E_{2g} and A_{1g} peak at both 4 weeks and 38 weeks are 382 cm^{-1} and 405 cm^{-1}, respectively. The fitted FWHM of the E_{2g} and A_{1g} peak at both 4 weeks and 38 weeks are about 5.1 cm^{-1} and 7.0 cm^{-1}, respectively. Figure 7.6 (h) shows PL spectra collected at the same black cross, normalized to the Si Raman peak at 520 cm^{-1}. The peak positions of the B and A excitons of both the 4 week and 38-week exposed sample are 1.93 eV and 1.80 eV, respectively. The peaks also have very comparable heights. These values are consistent with those in the literature for as-grown samples [24, 25].

A mechanism for ML degradation proposed by Kotsakidis et al. [4] involves a FRET process in which photoexcited trions in the singlet state, S_1, act as photosensitizers that excite molecular O_2 to the singlet state, denoted in spectroscopic notation by $^1\Delta_g$. Singlet O_2 is a strong reactive oxygen species due to its electronic configuration and degrades the MoS$_2$. The steps in a typical FRET process are photoexcitation of a photosensitizer to the singlet state, S_1, followed by quenching of the S_1 state to the triplet state, T_1, by O_2 molecules in the triplet ground state, $3\,\Sigma_g^-$. The T_1 state is then quenched by $3\,\Sigma_g^-$ O_2 molecules. As a result of these processes, the $3\,\Sigma_g^-$ O_2 molecules are excited to the $^1\Delta_g$ state. A FRET process proceeds at a high rate in a direct band gap semiconductor such as ML MoS$_2$ in which radiative transitions occur at a high rate [4]. Such a mechanism was also proposed by Ding et al. [29] to explain the production of $^1\Delta_g$ O_2 in TMD quantum dots in solution that were exposed to visible light. These authors found a significant increase in the production of $^1\Delta_g$ O_2 with an increase in defects such as sulfur vacancies. This was attributed to the defects modifying the bandgap, resulting in an increase in the photosensitizing rate. An increase in $^1\Delta_g$ O_2 production at defects is consistent with the observation that ML degradation in

ambient air starts preferentially along defect sites, such as grain boundaries and edges [3, 4, 6]. The FRET mechanism is consistent with our observation that BL and thicker-layer MoS_2 films do not degrade since these materials have indirect band gaps and consequently low radiative transition rates. The other type of mechanism proposed by Kotsakidis et al. [4] to explain ML degradation is a photocatalytic process in which photoexcited electrons and holes catalyze a hydrogen evolution reaction (HER) with adsorbed H_2O and $3O_2$ molecules, similar to the HER reaction in TiO_2. This reaction produces various reactive oxygen species that can degrade the ML [4]. Such photocatalytic reactions are likely to occur at a faster rate in an indirect band gap semiconductor than in a direct band gap semiconductor because photoexcited electrons and holes in indirect band gap semiconductors have longer lifetimes due to the absence of direct radiative transitions. For example, in TiO_2 the anatase phase is significantly more photocatalytic than the rutile and brookite phases. It has recently been computationally shown that a main reason for this is that the anatase phase has long electron and hole lifetimes because of its indirect bandgap, while the rutile and brookite phases have direct band gaps [30]. Since we do not observe degradation in BL and multi-layer MoS_2 samples, we conclude that photocatalytic processes that may occur on the surfaces of these materials do not cause significant degradation, and consequently are not likely to cause significant degradation of MLs since in MLs such photocatalytic processes would occur at a lower rate.

Our results that BL and thicker-layer MoS_2 are significantly more stable than MLs is different from the results of Budania et al. [5] who reported that exfoliated multilayer MoS_2 flakes decompose when left in ambient air at RT and 60% RH. These authors found that the decomposition of multilayers involves the formation of speckles on the surface. Unlike the irreversible degradation of MLs, they found that the speckles reduce in size and number after vacuum annealing the samples at 200 °C for 2 h. We conjecture that the speckles are caused by thick water films produced by condensation due to the high humidity environment. Under water, multilayer MoS_2 has been reported to decompose by a different mechanism involving the dissolution of oxides in water. The removal of the oxides leaves the surface susceptible

to continued oxidation [31–33]. For example, Zhang et al. [32] studied the oxidation of thick MoS_2 sheets placed in water for up to 12 h and observed etching of the basal plane that was attributed to dissolution of oxides. Also, Parzinger et al. [33] attributed the photocorrosion of exfoliated ML and trilayer MoS_2 in water to dissolution of oxides. We propose that in ambient air at humidities of about 43%, water films that dissolve oxides do not form on the multilayer surface, and the oxidized sites protect the surface from further oxidation. In MLs, degradation occurs by reaction with singlet oxygen produced by the FRET mechanism.

7.5. Conclusions

CVD-grown BL and thicker-layer MoS_2 films do not significantly degrade under ambient conditions at RT, 43% RH and incident room light intensity of 1000 Lux for the period tested of up to 2 years for non-preheated films and 64.5 weeks for preheated films. The structural and optical properties of aged BL and thicker-layer films were like as-grown films as determined by AFM, and Raman and PL spectroscopies. This contrasts with MLs that almost completely degrade during this time. These results support a previously reported mechanism in which ML TMD degradation is due to a FRET mechanism, since such a mechanism would occur at a higher rate in a direct band gap semiconductor than in an indirect band gap semiconductor. These results also show that photocatalytic processes do not play a significant role in ML degradation, since such processes would occur at a higher rate in an indirect band gap semiconductor. We expect that other TMDs in which the ML has a direct band gap and the BL and thicker layers have indirect band gaps will also have this property. Our results should motivate research into BL and thicker-layer TMDs since these materials are likely to be significantly more stable under ambient conditions.

7.6. Materials and Methods

The MoS_2 samples were grown using CVD on 300 nm thick SiO_2 layers on Si using the same procedure we have previously reported [34]. The SiO_2/Si substrate and crucibles containing S and MoO_3 were placed in a tube furnace. The tube furnace was then flushed at RT with ultrahigh purity Ar at a flow rate of 500 sccm for 10 min. Growth was carried

out by ramping the temperature of the tube furnace at 25 °C/min up to 800 °C with an Ar flow rate of 100 sccm. The temperature was kept at 800 °C for 20 min, after which the tube furnace was turned off and allowed to cool to RT. We used a NaCl precursor during the growth, which has been reported to contribute to the formation of multilayer MoS_2 [13]. We have previously reported that the NaCl precursor does not contribute to ML degradation [6]. The samples were preheated in a different tube furnace in air at atmospheric pressure. Raman and PL spectroscopy maps were obtained using a Renishaw inVia Raman Microscope with a 532 nm laser and Renishaw Centrus CCD detector, laser power of 0.5 mW, spot size of 764 nm, grating of 1800 lines/mm, and a spectral resolution of 1.75 cm^{-1}. The maps were acquired with a stage step size of 0.1 μm and integration time of 0.1 s per point. The AFM system used was an Ambios Q-scope.

7.7. Supporting Information

7.7.1. Optical Image of Bilayer Stability without Sample Preheating

We observe the stability of bilayers (BLs) in all our naturally aged samples, regardless of location on the substrate, growth batch, or time left in air up to 2 years. Figure 7.7 shows representative optical images of a 1.5-year-old CVD-grown MoS_2 film on an SiO_2 substrate. In Figure 7.7 (a), the arrows indicate MoS_2 islands where the monolayer (ML) has developed regions of light optical contrast, indicating degradation [6], but the BL appears optically uniform, suggesting that it has not degraded. Figure 7.7 (b) is a high magnification optical image of the boxed region in Figure 7.7 (a) showing an AB-stacked BL that has not degraded. Figures 7.7 (c) shows an optical image of a different area of the same SiO_2 substrate. The arrows indicate MoS_2 islands where the ML has developed regions of light optical contrast, but the BL appears optically uniform. Figure 7.7 (d) is a high-magnification optical image of the boxed region in Figure 7.7 (c) showing an AA-stacked BL that has not degraded.
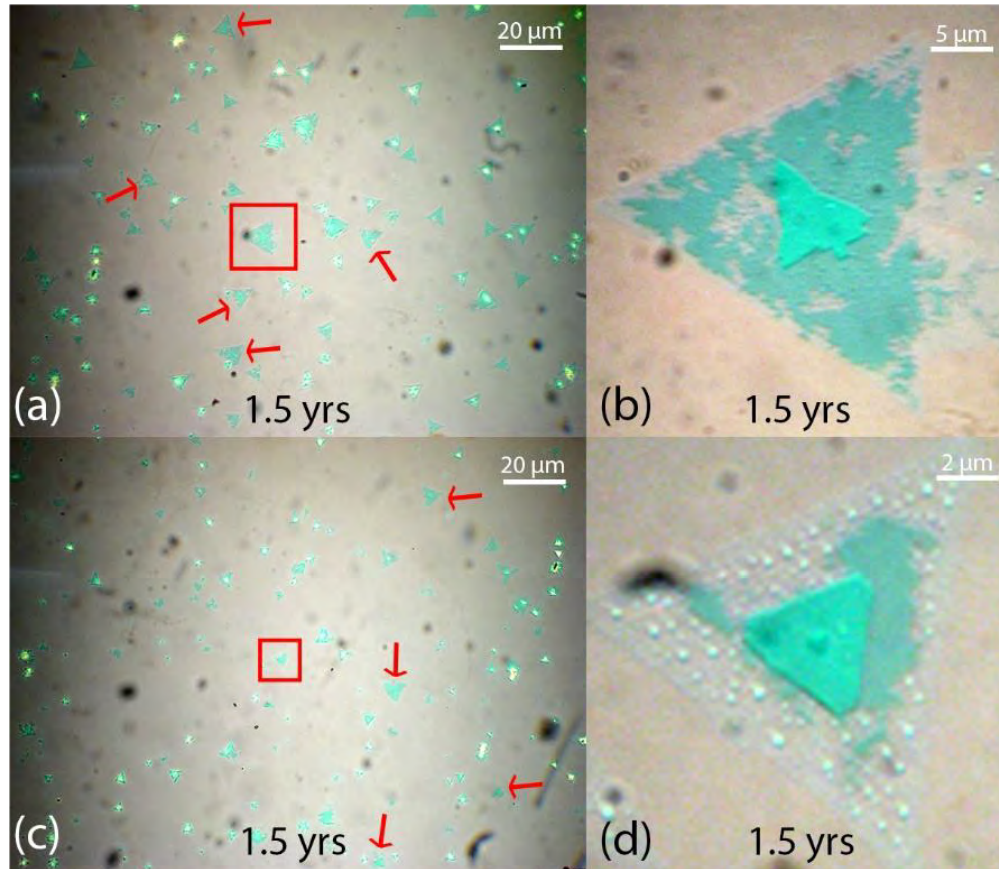
FIGURE 7.7. (a) Low-magnification optical image of an MoS$_2$ sample that has been left under ambient conditions for 1.5 years. The red arrows point at specific examples where the degradation is proceeding over the monolayer, but the bilayer remains stable. (b) High-magnification optical image of the boxed area in (a) showing an AB-stacked bilayer. (c) Wide-area optical image of a different sample region in which arrows indicate examples of degradation. (d) High-magnification optical image of the boxed area in (c) showing an AA-stacked bilayer.

7.7.2. Irreversibility of Degradation

The formation of dendrites in ML MoS$_2$ was found to be irreversible with respect to heating in vacuum. Figures 7.8 (a) and (b) show optical and AFM images, respectively, of a CVD-grown MoS$_2$ sample that has been preheated in air at 290 °C for 2 h and then left in ambient conditions for 4 weeks. The arrows in Figures 7.8 (b) show regions of elevated
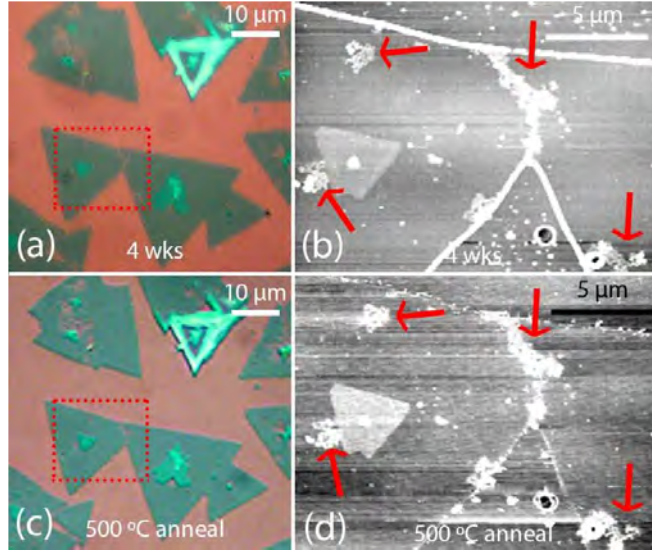
FIGURE 7.8. (a) Optical image of an MoS$_2$ sample preheated at 290 °C for 2 h in air and then left under ambient conditions for 4 weeks. (b) AFM image of the boxed area in (a). Dendrites are visible, as indicated by the arrows. (c) Optical image of the sample after vacuum annealing at 10^{-5} Torr and 500 °C for 2 h. (d) AFM image of the boxed area in (c). The dendrites are still visible, as shown by the arrows, indicating that the degradation has not been removed.

dendrites, indicating degradation [3, 6]. The sample was then annealed in a vacuum at about 10^{-5} Torr at a temperature of 500 °C for 2 h. Figures 7.8 (c) and (d) show optical and AFM images, respectively, of the sample immediately after the vacuum anneal. The arrows in Figures 7.8 (d) indicate the same regions of elevated dendrites as in Figures 7.8 (b), showing that the degradation remained.

7.7.3. 1.5-year-old Non-Preheated Sample: Fitted Raman Height, Position, and Width Maps, and PL Map

We used the Renishaw Wire software (Renishaw WiRE 5.2 software, Renishaw) to generate maps of the fitted peak heights, positions, and FWHMs of the Raman E$_{2g}$ and A$_{1g}$ peaks. Such maps are useful in determining slight variations in peak position and FWHM. For example, sample strain has been shown to produce a shift in position and broadening of

141

the E_{2g} peak without a corresponding shift and broadening in the A_{1g} peak [36]. Figure 7.9 shows fitted peak maps of the BL sample shown in Figure 7.2 of the paper after 1.5 years of exposure to ambient conditions. Figures 7.9 (a-c) show maps of the fitted height, position, and FWHM of the E_{2g} peak, respectively, and Figures 7.9 (d-f) show maps of the fitted height, position, and FWHM of the A_{1g} peak, respectively. All the fitted peak maps were generated from the spectra collected during the run for the map shown in Figure 7.2. Figures 7.9 (a) and (d) show that the BL has a large E_{2g} and A_{1g} peak height, as expected, and the heights are relatively uniform throughout the BL. On the other hand, the ML regions contain areas of significantly decreased height, which represents degradation. Labels 1-3 in (a)-(f) serve as a visual guide to indicate the same degraded regions. We note that the position and width of the E_{2g} and A_{1g} peaks are also uniform on the BL. On the ML, they exhibit slight shifts towards higher wavenumbers and broadening when closer to the degraded regions. The E_{2g} shows a more significant peak shift and broadening compared to the A_{1g} peak, as has been previously reported for ML degradation [6]. Figures 7.10 (a) shows the PL height map copied from Figure 7.2 (c) of the paper for convenience. Figure 7.10 (b) shows orange and blue PL spectra collected at the orange and blue crosses, respectively, shown in Figure 7.10 (a). The orange cross is in a region where the ML has not significantly degraded, and the blue cross is in a region where the ML has significantly degraded. In Figure 7.10 (b), the A exciton height is decreased by a factor of about 4, and shifts to higher energy by about 0.5 eV, consistent with previous reports [36]. We observe a decrease in the A exciton height by up to a factor of 20 in degraded areas.

7.7.4. Optical Image of Bilayer Stability with Sample Preheating

Figure 7.11 shows representative optical images of MoS_2 samples that were preheated in air at 330 °C for 2h, showing that BLs are also stable in ambient conditions after preheating. Preheating accelerates ML degradation [6]. Figure 7.11 (a) shows an optical image of the sample taken immediately after preheating. The BLs indicated by numbers 1 and 3 are AB stacked, and the BL indicated by the number 2 is AA stacked. Figure 7.11 (b) shows a high-magnification optical image of the boxed region in (a). Figure 7.11 (c) and (d) show
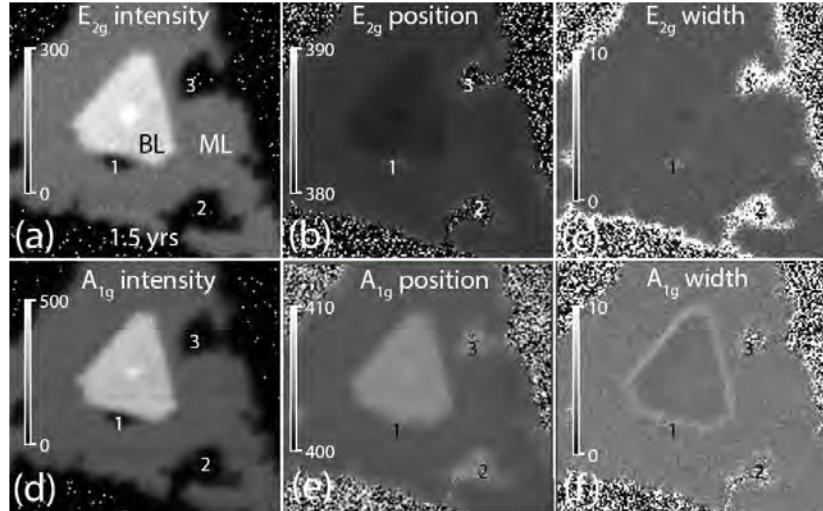
FIGURE 7.9. Fitted peak maps of the 1.5-yr-old sample from Figure 7.2 in the paper. The numbers 1, 2 and 3 indicate regions of degradation on the monolayer. (a-c) Peak height, position, and FWHM maps, respectively, of the E_{2g} peak. (d-f) Peak height, position, and FWHM maps, respectively, of the A_{1g} peak.

optical images of the same sample areas as in (a) and (b), respectively, after the sample was left under ambient conditions for 9 weeks. We have examined hundreds of preheated samples and not observed BL degradation.

7.7.5. Multilayer Sample: Optical and AFM Images After 18 Weeks, and Fitted Raman Height, Position, and Width Maps After 42.5 Weeks.

Figures 7.12 (a) and (b) show optical and AFM images, respectively, of the multilayer MoS_2 sample shown in Figures 7.4 and 7.5 of the paper after 18 weeks of exposure to ambient conditions. The red arrow indicates the bright circular region that was also observed after 42.5 weeks of exposure in Figure 7.5 (a) of the paper. The bright circular region has remained almost unchanged in shape and size between 18 weeks and 42.5 weeks. We note that we do not observe this region after 15 weeks, as shown in Figures 7.4 (g) and (h) of the paper. This region appeared over a period of at most 3 weeks and then did not significantly change. We conclude it is not a product of degradation and may be contamination deposited on the

143

FIGURE 7.10. (a) Raman height map of the A exciton peak of the 1.5-yr-old sample, copied from Figure 7.2 in the paper. (b) PL spectr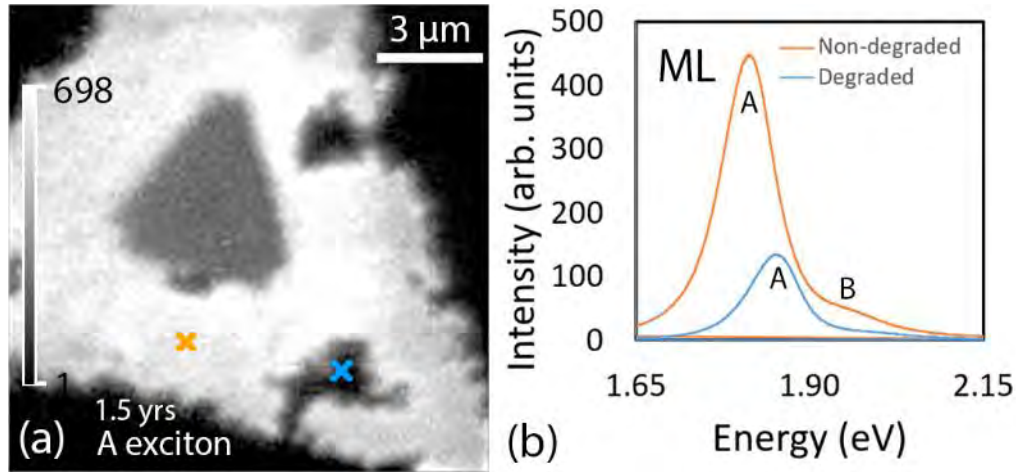a taken at the locations indicated by the blue and orange crosses in (a). The blue and orange curves were taken at the locations indicated by the blue and orange crosses, respectively.

sample. Figure 7.11 shows fitted peak maps preheated multilayer sample shown in Figure 7.5 of the paper after 42.5 weeks of exposure to ambient conditions. The fitted maps were generated from the spectra collected during the run for the map shown in Figure 7.5 (b) of the paper. Figure 7.13 (a-c) show maps of the fitted height, position, and width of the E_{2g} peak, respectively, and Figures 7.13 (d-f) show maps of the fitted height, position, and width of the A_{1g} peak, respectively. The E_{2g} and A_{1g} peaks of the BL and thicker layers have uniform heights, positions, and widths with the exception of areas indicated by the arrows in Figure 7.13, which correspond to the large circular regions observed in the AFM image shown in Figure 7.5 (a) of the paper. These circular regions exhibit lower E_{2g} and A_{1g} heights. We note that in the circular regions, Figure 7.13 (b) shows that the E_{2g} peak shifts to lower wavenumbers by as much as 1.1 cm^{-1}, while Figure 7.13 (e) shows that the position of the A_{1g} peak does not noticeably shift from that of the surrounding areas.

In addition, Figure 7.13 (c) shows that the width of the E_{2g} peak in the circular regions increases by as much as 2.3 cm^{-1}, while Figure 7.13 (f) shows that the width of

144
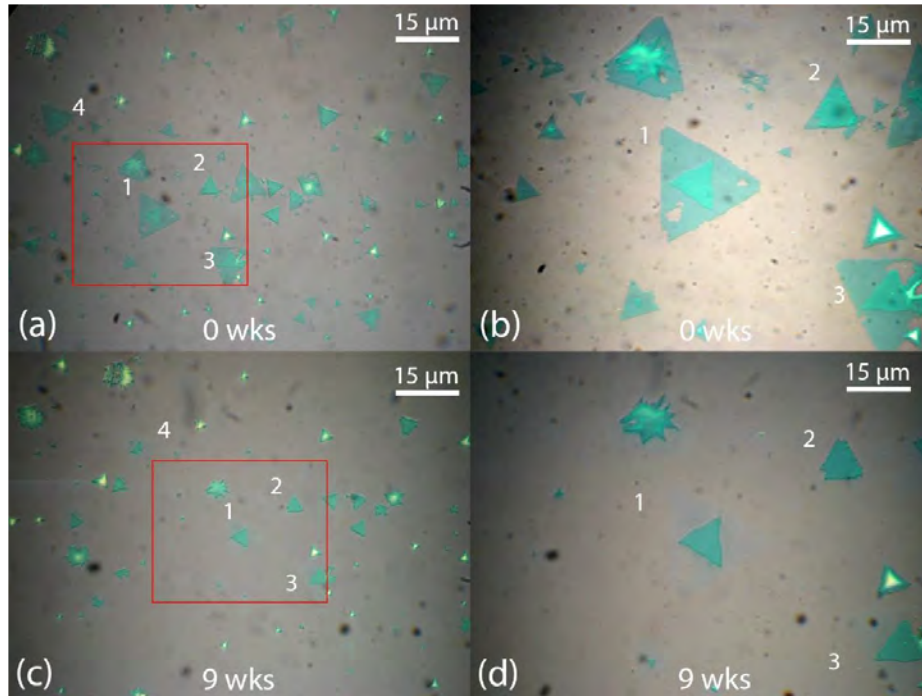
FIGURE 7.11. (a) Optical images of an MoS$_2$ sample immediately after heating in air at 330 °C for 2 h. The numbers 1, 2 and 3 indicate AB, AA and AB-stacked bilayers, respectively. (b) High-magnification optical image of the boxed area in (a). (c) Optical image of the same area in (a) after 9 weeks of exposure to ambient conditions. (d) High-magnification optical image of the boxed area in (c). The monolayers have completely degraded whereas the bilayers remain visible with no sign of degradation

the A$_{1g}$ peak does not change significantly. Sample strain has been shown to result in blue shifting and broadening of the E$_{2g}$ peak with no significant change in the position and width of the A$_{1g}$ peak [36]. Since both the E$_{2g}$ and A$_{1g}$ peaks exhibit decreased height, we believe that a contaminant may have been deposited on the sample, which is blocking the E$_{2g}$ and A$_{1g}$ height signals and applying strain to the underlying MoS$_2$ lattice.

7.7.6. 4-Week-Old Preheated Sample: Fitted Raman Height, Position, and Width Maps.

Figure 7.14 shows fitted peak maps of the preheated BL sample shown in Figure 7.6 (b) of the paper that was exposed to ambient conditions for 4 weeks. The fitted maps were
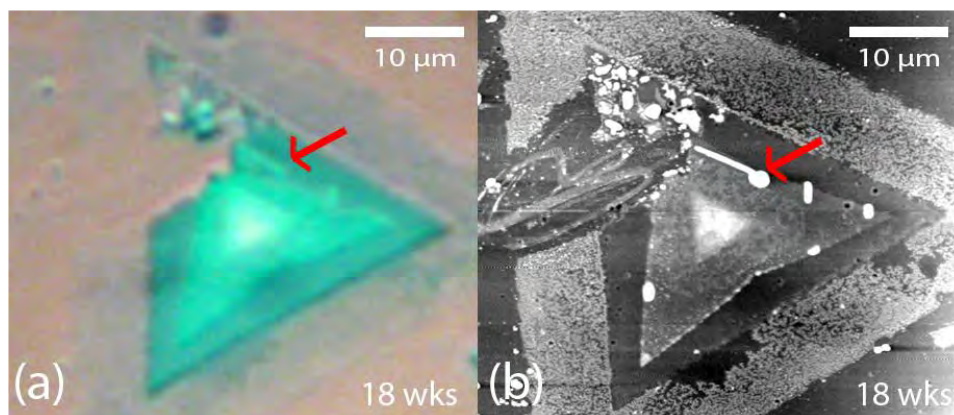
FIGURE 7.12. (a) and (b) Optical and AFM images, respectively, of the MoS$_2$ sample shown in Figure 7.4 of the paper after 18 weeks of exposure to ambient conditions. The arrows indicate the location of bright circular regions seen in Figure 7.5 (a).
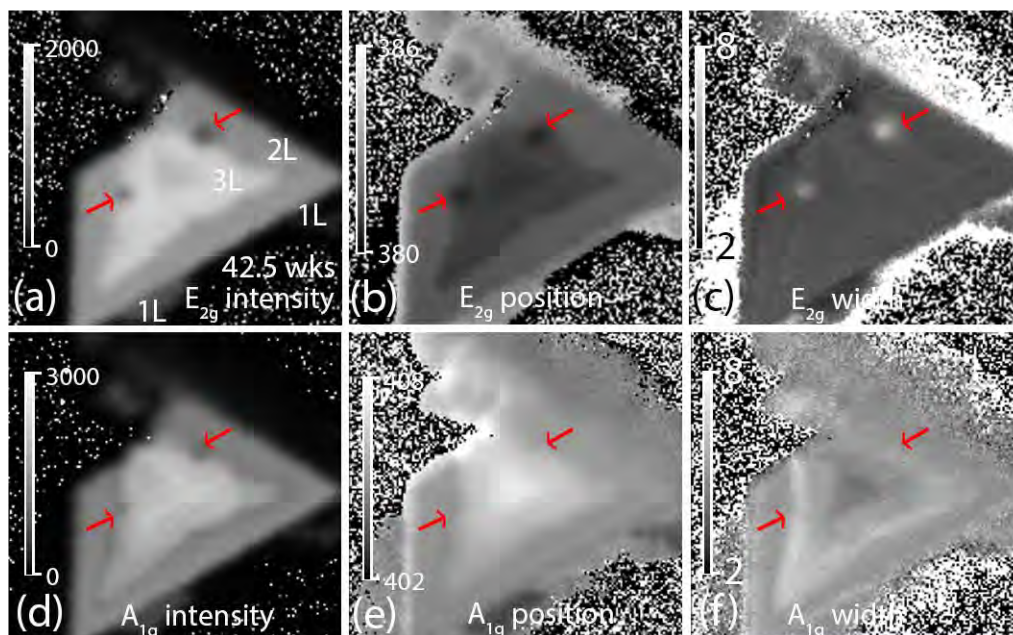
FIGURE 7.13. Fitted peak maps of the multilayer sample shown in Figure 7.5 (a) after 42.5 weeks of exposure to ambient conditions. (a-c) Peak height, position, and FWHM maps, respectively, of the E$_{2g}$ peak. (d-f) Peak height, position, and FWHM maps, respectively, of the A$_{1g}$ peak.

146
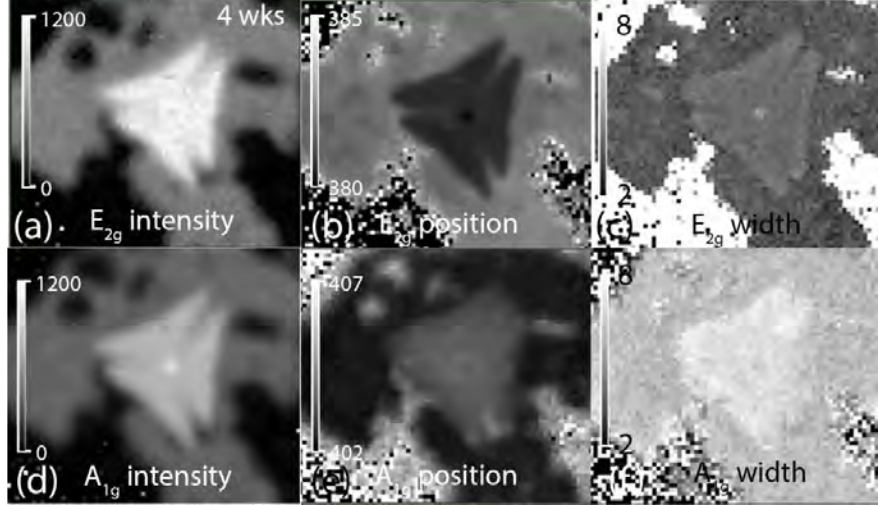
FIGURE 7.14. Fitted peak maps of the sample shown in Figure 7.6 (b) of the paper after 4 weeks of exposure to ambient conditions. (a-c) Peak height, position, and FWHM maps, respectively, of the E_{2g} peak. (d-f) Peak height, position, and FWHM maps, respectively, of the A_{1g} peak.

generated from the spectra collected during the run for the map shown in Figure 7.6. Figures 7.14 (a-c) show maps of the fitted height, position, and FWHM of the E_{2g} peak, respectively, and Figures 7.14 (d-f) show maps of the fitted height, position, and FWHM of the A_{1g} peak, respectively. Both the E_{2g} and A_{1g} peaks of degraded ML regions show lower heights, shifts to higher wavenumbers, and broadening of the widths. The BL regions appear uniform.

7.8. Acknowledgement

7.9. References

[1] Cao, Y.; Mishchenko, A.; Yu, G. L.; Khestanova, E.; Rooney, A. P.; Prestat, E.; Kretinin, A. V.; Blake, P.; Shalom, M. B.; Woods, C.; et al. Quality Heterostructures from Two-Dimensional Crystals Unstable in Air by Their Assembly in Inert

147

Atmosphere. Nano Letters, 2015, 15, 4914–4921.

[2] Wang, Q. H.; Kalantar-Zadeh, K.; Kis, A.; Coleman, J. N.; Strano, M. S. Electronics and Optoelectronics of Two-Dimensional Transition Metal Dichalcogenides. Nature Nanotechnology, 2012, 7, 699–712.

[3] Gao, J.; Li, B.; Tan, J.; Chow, P.; Lu, T.-M.; Koratkar, N. Aging of Transition Metal Dichalcogenide Monolayers. ACS Nano, 2016, 10, 2628–2635.

[4] Kotsakidis, J. C.; Zhang, Q.; de Parga, A. L. V.; Currie, M.; Helmerson, K.; Kurt Gaskill, D.; Fuhrer, M. S. Oxidation of Monolayer WS2 in Ambient Is a Photoinduced Process. Nano Letters, 2019, 19, 5205–5215.

[5] Budania, P.; Baine, P.; Montgomery, J.; McGeough, C.; Cafolla, T.; Modreanu, M.; McNeill, D.; Mitchell, N.; Hughes, G.; Hurley, P. Long-Term Stability of Mechanically Exfoliated MoS_2 Flakes. MRS Communications, 2017, 7, 813–818.

[6] Yao, K., Femi-Oyetoro, J.D., Yao, S., Jiang, Y., El Bouanani, L., Jones, D.C., Ecton, P.A., Philipose, U., El Bouanani, M., Rout, B., Neogi, A., and Perez, J.M., 2019.. Rapid Ambient Degradation of Monolayer MoS_2 after Heating in Air. 2D Materials, 2019, 7, 015024.

[7] Şar, H.; Özden, A.; Demiroğlu, İ.; Sevik, C.; Perkgoz, N. K.; Ay, F. Long-Term Stability Control of CVD-Grown Monolayer MoS 2. physica status solidi (RRL) – Rapid Research Letters, 2019, 13, 1800687.

[8] Birowska, M.; Urban, J.; Baranowski, M.; Maude, D. K.; Plochocka, P.; Szwacki, N. G. The Impact of Hexagonal Boron Nitride Encapsulation on the Structural and Vibrational Properties of Few Layer Black Phosphorus. Nanotechnology, 2019, 30, 195201.

[9] Chamlagain, B.; Li, Q.; Ghimire, N. J.; Chuang, H.-J.; Perera, M. M.; Tu, H.; Xu, Y.; Pan, M.; Xaio, D.; Yan, J.; et al. Mobility Improvement and Temperature Dependence in MoSe2 Field-Effect Transistors on Parylene-C Substrate. ACS Nano, 2014, 8, 5079–5088.

[10] Wang, H.; Yu, L.; Lee, Y.-H.; Shi, Y.; Hsu, A.; Chin, M. L.; Li, L.-J.; Dubey, M.;

Kong, J.; Palacios, T. Integrated Circuits Based on Bilayer MoS_2 Transistors. Nano Letters, 2012, 12, 4674–4680.

[11] Bertolazzi, S.; Brivio, J.; Kis, A. Stretching and Breaking of Ultrathin MoS_2. ACS Nano, 2011, 5, 9703–9709.

[12] Wang, W.; Klots, A.; Prasai, D.; Yang, Y.; Bolotin, K. I.; Valentine, J. Hot Electron-Based NearInfrared Photodetection Using Bilayer MoS_2. Nano Lett. 2015, 15, 7440–7444.

[13] Shinde, S. M.; Dhakal, K. P.; Chen, X.; Yun, W. S.; Lee, J.; Kim, H.; Ahn, J.-H. StackingControllable Interlayer Coupling and Symmetric Configuration of Multilayered MoS_2. NPG Asia Materials, 2018, 10, e468–e468.

[14] Liu, K.; Zhang, L.; Cao, T.; Jin, C.; Qiu, D.; Zhou, Q.; Zettl, A.; Yang, P.; Louie, S. G.; Wang, F. Evolution of Interlayer Coupling in Twisted Molybdenum Disulfide Bilayers. Nature Communications, 2014, 5, 1-6.

[15] Ramasubramaniam, A.; Naveh, D.; Towe, E. Tunable Band Gaps in Bilayer Transition-Metal Dichalcogenides. Physical Review B, 2011, 84, 205325.

[16] Sun, M.; Xie, D.; Sun, Y.; Li, W.; Teng, C.; Xu, J. Lateral Multilayer/monolayer MoS_2 Heterojunction for High Performance Photodetector Applications. Scientific Reports, 2017, 7, 1-7.

[17] Sahoo, P. K.; Memaran, S.; Nugera, F. A.; Xin, Y.; Díaz Márquez, T.; Lu, Z.; Zheng, W.; Zhigadlo, N. D.; Smirnov, D.; Balicas, L.; et al. Bilayer Lateral Heterostructures of Transition-Metal Dichalcogenides and Their Optoelectronic Response. ACS Nano, 2019, 13, 12372–12384.

[18] Cao, Y.; Fatemi, V.; Fang, S.; Watanabe, K.; Taniguchi, T.; Kaxiras, E.; Jarillo-Herrero, P. Unconventional Superconductivity in Magic-Angle Graphene Superlattices. Nature, 2018, 556, 43–50.

[19] Yeh, P.-C.; Jin, W.; Zaki, N.; Kunstmann, J.; Chenet, D.; Arefe, G.; Sadowski, J. T.; Dadap, J. I.; Sutter, P.; Hone, J.; et al. Direct Measurement of the Tunable Electronic Structure of Bilayer MoS_2 by Interlayer Twist. Nano Letters, 2016, 16,

953–959.

[20] Lin, M.-L.; Tan, Q.-H.; Wu, J.-B.; Chen, X.-S.; Wang, J.-H.; Pan, Y.-H.; Zhang, X.; Cong, X.; Zhang, J.; Ji, W.; et al. Moiré Phonons in Twisted Bilayer MoS_2. ACS Nano, 2018, 12, 8770–8780.

[21] Yao, K.; Banerjee, D.; Femi-Oyetoro, J. D.; Hathaway, E.; Jiang, Y.; Squires, B.; Jones, D. C.; Neogi, A.; Cui, J.; Philipose, U.; et al. Growth of Monolayer MoS_2 on Hydrophobic Substrates as a Novel and Feasible Method to Prevent the Ambient Degradation of Monolayer MoS_2. MRS Advances, 2020, 1–9.

[22] Electrical Characterization of Back-Gated Bi-Layer MoS_2 Field-Effect Transistors and the Effect of Ambient on Their Performances. Applied Physics Letters, 2012, 100, 123104.

[23] Lanzillo, N. A.; Glen Birdwell, A.; Amani, M.; Crowne, F. J.; Shah, P. B.; Najmaei, S.; Liu, Z.; Ajayan, P. M.; Lou, J.; Dubey, M.; et al. Temperature-Dependent Phonon Shifts in Monolayer MoS_2. Applied Physics Letters, 2013, 103, 093102.

[24] Xia, J.; Yan, J.; Shen, Z. X. Transition Metal Dichalcogenides: Structural, Optical and Electronic Property Tuning via Thickness and Stacking. FlatChem, 2017, 4, 1–19.

[25] Zhang, X.; Qiao, X.-F.; Shi, W.; Wu, J.-B.; Jiang, D.-S.; Tan, P.-H. Phonon and Raman Scattering of Two-Dimensional Transition Metal Dichalcogenides from Monolayer, Multilayer to Bulk Material. Chem. Soc. Rev. 2015, 44, 2757–2785.

[26] Zhou, H.; Yu, F.; Liu, Y.; Zou, X.; Cong, C.; Qiu, C.; Yu, T.; Yan, Z.; Shen, X.; Sun, L.; et al. Thickness-Dependent Patterning of MoS_2 Sheets with Well-Oriented Triangular Pits by Heating in Air. Nano Research, 2013, 6, 703–711.

[27] Liu, L.; Ryu, S.; Tomasik, M. R.; Stolyarova, E.; Jung, N.; Hybertsen, M. S.; Steigerwald, M. L.; Brus, L. E.; Flynn, G. W. Graphene Oxidation: Thickness-Dependent Etching and Strong Chemical Doping. Nano Lett. 2008, 8, 1965–1970.

[28] Rice, C.; Young, R. J.; Zan, R.; Bangert, U.; Wolverson, D.; Georgiou, T.; Jalil, R.; Novoselov, K. S. Raman-Scattering Measurements and First-Principles Calculations

of Strain-Induced Phonon Shifts in Monolayer MoS_2. Physical Review B, 2013, 87, 081307.

[29] Ding, X.; Peng, F.; Zhou, J.; Gong, W.; Slaven, G.; Loh, K. P.; Lim, C. T.; Leong, D. T. Defect Engineered Bioactive Transition Metals Dichalcogenides Quantum Dots. Nat. Commun. 2019, 10, 41.

[30] Zhang, J.; Zhou, P.; Liu, J.; Yu, J. New Understanding of the Difference of Photocatalytic Activity among Anatase, Rutile and Brookite TiO_2. Phys. Chem. Chem. Phys. 2014, 16, 20382–20386.

[31] Afanasiev, P.; Lorentz, C. Oxidation of Nanodispersed MoS_2 in Ambient Air: The Products and the Mechanistic Steps. The Journal of Physical Chemistry C, 2019, 123, 7486–7494.

[32] Zhang, X.; Jia, F.; Yang, B.; Song, S. Oxidation of Molybdenum Disulfide Sheet in Water under in Situ Atomic Force Microscopy Observation. The Journal of Physical Chemistry C, 2017, 121, 9938– 9943.

[33] Parzinger, E.; Miller, B.; Blaschke, B.; Garrido, J. A.; Ager, J. W.; Holleitner, A.; Wurstbauer, U. Photocatalytic Stability of Single- and Few-Layer MoS_2. ACS Nano, 2015, 9, 11302–11309.

[34] Jiang, Y.; Lin, Y.; Cui, J.; Philipose, U. Effects of Strategically Placed Water Droplets on Monolayer Growth of Molybdenum.

[35] Wang, H., Yu, L., Lee, Y.H., Shi, Y., Hsu, A., Chin, M.L., Li, L.J., Dubey, M., Kong, J. and Palacios, T., 2012. Integrated circuits based on bilayer MoS_2 transistors. Nano letters, 12(9), pp.4674-4680.

[36] Rice, C.; Young, R. J.; Zan, R.; Bangert, U.; Wolverson, D.; Georgiou, T.; Jalil, R.; Novoselov, K. S. Raman-Scattering Measurements and First-Principles Calculations of Strain-Induced Phonon Shifts in Monolayer MoS_2. Physical Review B, 2013, 87.

CHAPTER 8

CONCLUSIONS AND FUTURE WORK

8.1. Conclusions

This dissertation gives an extensive study on the low-energy electron irradiation effects and etching of graphene [1, 2]. In addition, the mechanisms for the degradation and stability of MoS_2 were investigated [3, 4]. To our knowledge, the properties of substrates have not been fully explored. We believe that the outcomes in this dissertation will trigger the urge to widely study the effect of etching graphene on the precision, resolution, and linewidth. In addition, although many 2D materials have been found, most degrade in air. The demonstration of a stability mechanism using bilayer and thicker layer transition metal dichalchogenides (TMDs), in this dissertation, would have a significant impact in this area. Finally, this research would also impact the field of twisted TMD bilayers that has recently attracted considerable interest. Knowledge of their air stability would spur additional interest in this area. The following sections explore propositions for future work.

8.2. New Techniques in Nanoscale Focused Electron Beam Cutting of 2D Materials

We propose to improve the precision, resolution, and line width at the nanoscale in the cutting and etching of 2D materials obtainable using focused electron beam (FEB) techniques. This will be accomplished by investigating in detail the effects of substrate charging on the precision, resolution and linewidth of etching obtained using FEB. This proposal is to develop improved FEB methods of patterning 2D materials. These materials have unique properties that have been the object of much research world-wide. Implementing these materials into useful devices remains a main objective in many research groups. Techniques that could be implemented at many research laboratories such as FEB would significantly speed up the development of useful devices. Many research laboratories have access to an scanning electron microscope (SEM) or e-beam lithography system. That cannot be said for other methods such as helium ion microscopy for example. With simple modifications to an existing SEM based e-beam lithography system involving the addition of a nozzle for gas
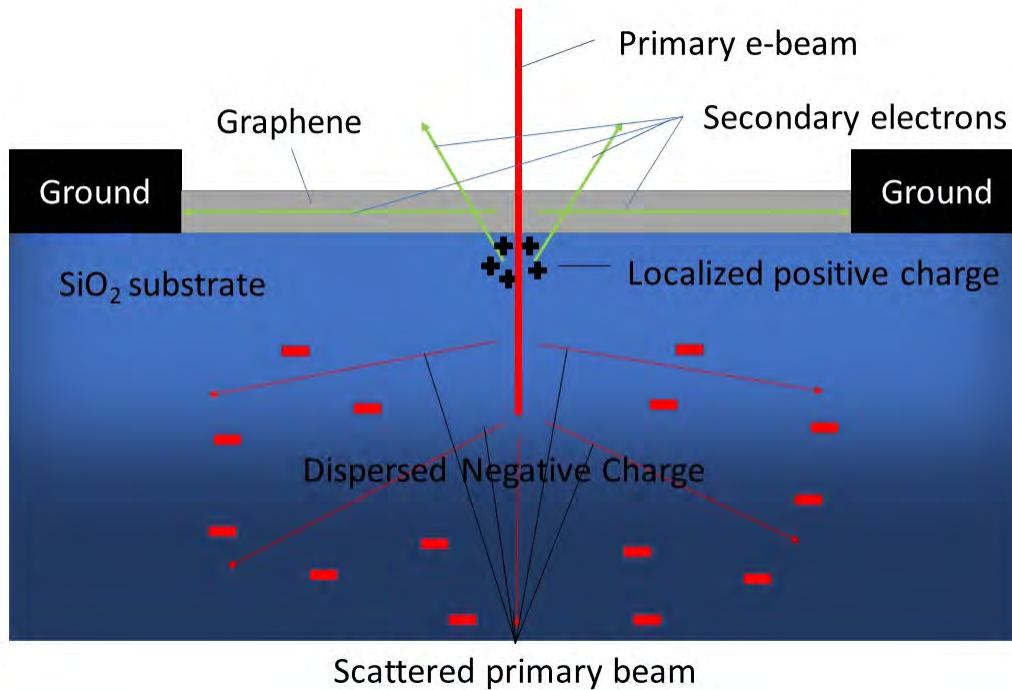
152

FIGURE 8.1. Illustration of the sample setup. The graphene sample is grounded, and thus any accumulated charge in the graphene will go to ground. At electron energies < 10 keV, the secondary electron emission will produce a localized positive charge at the surface of the SiO_2 near the location of the beam. There will also be a more widely dispersed negative charge deeper in the SiO_2 due to the primary beam being scattered.

delivery, it can be converted to an FEB system that can pattern 2D materials without the use of a resist. Successful ways of increasing the precision, resolution and linewidth of FEB etching techniques would therefore have a broad impact.

To our knowledge, the properties of the substrate that we propose to optimize have not been widely studied and little is known about their effect on precision, resolution, and linewidth. We plan to explore a variety of 2D materials such as graphene and TMDs, and gases such as oxygen, water vapor. Simulations of primary beam electron trajectories in SiO_2 were carried out to determine the effect on dielectric thickness on primary beam charge trapped in the dielectric. The simulations were run using the Monte Carlo simulation
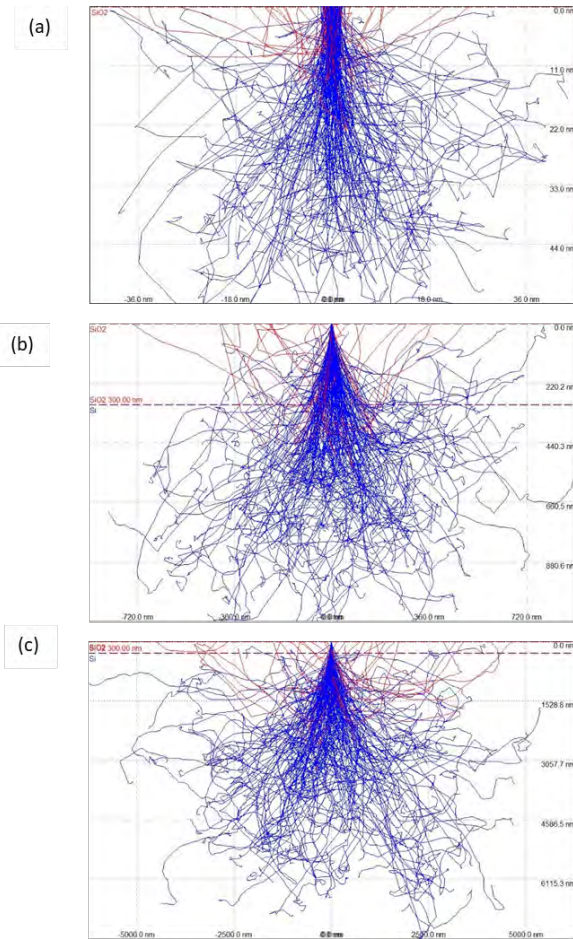
FIGURE 8.2. Simulations of electron trajectories for (a) 1.5 keV, (b) 10 keV and (c) 30 keV electrons.

software CASINO version 2.42 [6].

In all the simulations the e-beam diameter was 3 nm, the dielectric was SiO_2, and the substrate was Si. Figures 8.2 (a)-(c) show a simulation of the experiment in Figure 8.1 using an e-beam energy of 1.5, 10 and 30 keV, respectively, and an oxide thickness of 300 nm. The SiO_2/Si interface is indicated by the dashed purple horizontal line. At 1.5 keV, all the electrons are stopped within about 54 nm of the SiO_2. At 10 keV, significantly more electrons are stopped in the conducting Si substrate, and at 30 keV almost all the electrons are stopped in the conducting Si substrate. In Ref. [5], the acceleration voltage was 3 keV to produce a large SEM image contrast between the graphene sample and the substrate. Figure 8.3 (a) shows a simulation of the electron trajectories for 3 keV and 300 nm Si. As
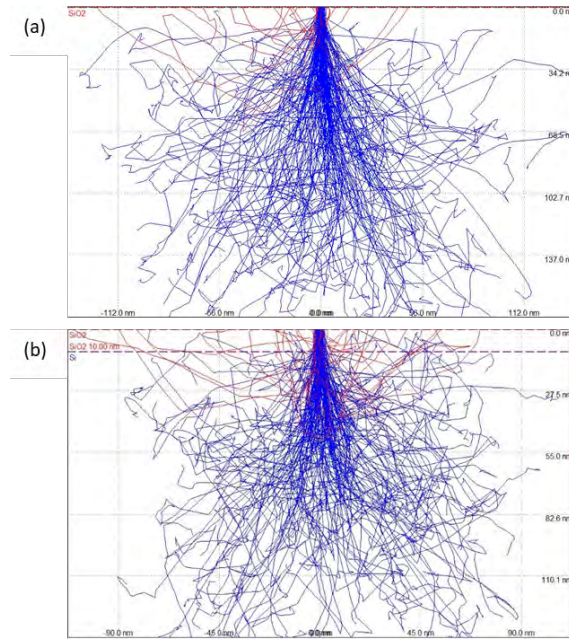
154

FIGURE 8.3. Simulations of electron trajectories for 3 keV electrons for an SiO$_2$ layer having a thickness of (a) 300 nm and (b) 10 nm.

can be seen in the figure, most of the electrons stop within 100 nm of the SiO$_2$. Figure 8.3 (b) shows a simulation for 3 keV with a 10 nm thick SiO$_2$ substrate instead. As can be seen in the figure, almost all the electrons stop in the conducting Si substrate. The Si used in our experiment is conducting and therefore the electrons will then be transferred to ground. Thus, we hypothesize there would be less negative charging of the substrate and therefore less damage to the graphene outside the intended etch area. There would also be less beam deflection effects due to the lack of negative charging. As a result, the precision, resolution, and linewidth of the etched patterns would be improved.

This method of lithography with an emphasis on dielectric thickness and substrate conductivity could also be applied to other 2D materials, such as MoS$_2$. It has been found that bulk pristine MoS$_2$ samples exposed to O$_2$ gas at 200 °C develop MoO$_x$ on the topmost layer without any effect to the underlying layers [7]. The MoO$_x$, when annealed at 500 °C, becomes volatile and is released into the vacuum chamber, and thus the top layer is completely removed. The authors of Ref. [7] ascribe the etching as mainly due to neutral reactive oxygen species, although that's because neutrals have longer lifetimes than ions. In

our case, the lifetime of ions is not a factor because they are continuously produced close to the sample by the e-beam. We hypothesize that the reactive oxygen species can be duplicated in our experiment with the oxygen gas and electron beam independent of the temperature. As a result, the same principle that we propose for precisely patterning graphene can be further explored by applying it to MoS_2 on a thin SiO_2 substrate. We propose that when an electron beam irradiates the sample, the SiO_2 underneath the MoS_2 that is exposed to the e-beam will become positively charged. This will cause negatively charged reactive oxygen species dissociated by the primary electron beam to be accelerated to the MoS_2, forming MoO_x. Thus, the same process can be used to pattern the MoS_2 by then annealing the sample at 500 °C.

8.3. Multilayer Encapsulation of TMDs

We propose to investigate the effectiveness of bilayer and TMD encapsulation of reactive Van der Waals materials (RVdWMs), which could catalyze research on realizing new heterostructure devices that are more efficient, stable, and reliable for commercial applications. We have recently found that bilayer and thicker-layered MoS_2 films are stable in air, and we hypothesize that bilayer and thicker-layered TMD encapsulants will effectively passivate RVdWMs. The demonstration of an effective encapsulation technique using TMDs would have a significant impact in this area because of the many novel electronic and optoelectronic devices that could be realized. In our TMD/RVdWM heterostructures, the RVdWM will be entirely encapsulated by the TMD, which is a semiconductor, as illustrated in Figure 8.4. In contrast, the most used encapsulants of RVdWMs such as hexagonal boron nitride (hBN), graphene and thin polymer films are insulating or conducting. The semiconducting property of TMDs will allow for the straightforward and scalable production of air-stable TMD/RVdWM devices with significantly fewer intermediary steps like encapsulation with hBN or thin polymer films that could also adversely affect the electrical and optical properties of the TMD/TVdWM device. Fabrication of MoS_2 back-gated transistors would become trivial since there would be no need for hBN encapsulation. To test the effectiveness of TMD encapsulation, we will first study the mechanism of degradation of TMDs
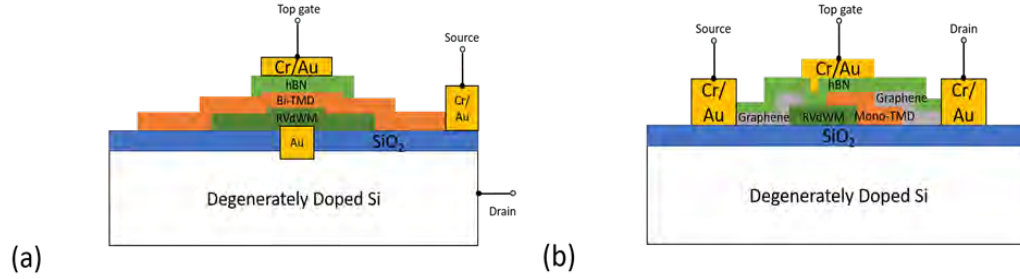
FIGURE 8.4. Encapsulated 3-terminal device to probe the electrical character-
istics of a TMD/RVdWM heterostructure based on (a) Our proposed electrical
contact structure and (b) published methods [8].

in air. Specifically, we will test the effects of interlayer coupling (bilayer twisting) on the
stability of TMD bilayers, which will give us insights on the optimal method to encapsulate
RVdWMs. In addition, we will study the air stability of the electronic and optoelectronic
properties of these devices. These studies will be carried out using a novel method to ac-
celerate the degradation that we have recently reported, which will allow us to study the
progression of degradation in weeks instead of years. We will use techniques such as atomic
force microscopy (AFM), Raman spectroscopy and X-ray photoelectron spectroscopy (XPS)
to characterize the degradation.

We will then synthesize TMD/RVdWM heterostructures using a combination of chem-
ical vapor deposition (CVD) and mechanical exfoliation and transfer techniques. Finally,
we will study their electronic and optoelectronic properties using transport measurements.
Since the RVdWM will be entirely encapsulated by the TMD, the electrical contact to the
RVdWM will be made using a simple interconnect platform where the encapsulated material
is electrically contacted from the bottom. Such a method of encapsulation has not been
reported previously, to our knowledge, and can potentially open a new field of research in
the applications of TMD/RVdWM heterostructures.

8.4. References

[1] Femi-Oyetoro, J.D., Yao, K., Roccapriore, K., Ecton, P.A., Tang, R., Jones, J.D.,
Verbeck, G. and Perez, J.M., 2019. Effects of high-dosage focused electron-beam

irradiation at energies 30 keV on graphene on SiO$_2$. Applied Surface Science, 469, pp.325-330.

[2] Femi-Oyetoro, J.D., Yao, K., Tang, R., Ecton, P., Roccapriore, K., Mhlanga, A., Verbeck, G., Weathers, D.L. and Perez, J.M., 2019. Mechanism for etching of exfoliated graphene on substrates by low-energy electron irradiation from helium plasma electron sources. Journal of Vacuum Science Technology A: Vacuum, Surfaces, and Films, 37(2), p.021401.

[3] Yao, K., Femi-Oyetoro, J.D., Yao, S., Jiang, Y., El Bouanani, L., Jones, D.C., Ecton, P.A., Philipose, U., El Bouanani, M., Rout, B., Neogi, A., and Perez, J.M., 2019. Rapid ambient degradation of monolayer MoS$_2$ after heating in air. 2D Materials, 7(1), p.015024.

[4] Femi-Oyetoro, J., Yao, K., Hathaway, E., Jiang, Y., Ojo, I., Squires, B., Neogi, A., Cui, J., Philipose, U., Gadiyaram, N.K., Zhou, W., and Perez, J., 2020. Long-term Stability of Bilayer MoS$_2$ in Ambient Air. arXiv preprint arXiv:2010.06770.

[5] Thiele, C., Felten, A., Echtermeyer, T.J., Ferrari, A.C., Casiraghi, C., Löhneysen, H.V. and Krupke, R., 2013. Electron-beam-induced direct etching of graphene. Carbon, 64, pp.84-91

[6] Drouin, D., Couture, A.R., Joly, D., Tastet, X., Aimez, V. and Gauvin, R., 2007. CASINO V2. 42—a fast and easy-to-use modeling tool for scanning electron microscopy and microanalysis users. Scanning: The Journal of Scanning Microscopies, 29(3), pp.92-101.

[7] Zhu, H., Qin, X., Cheng, L., Azcatl, A., Kim, J. and Wallace, R.M., 2016. Remote plasma oxidation and atomic layer etching of MoS$_2$. ACS applied materials interfaces, 8(29), pp.19119-19126.

[8] Lee, G.H., Cui, X., Kim, Y.D., Arefe, G., Zhang, X., Lee, C.H., Ye, F., Watanabe, K., Taniguchi, T., Kim, P. and Hone, J., 2015. Highly stable, dual-gated MoS$_2$ transistors encapsulated by hexagonal boron nitride with gate-controllable contact, resistance, and threshold voltage. ACS nano, 9(7), pp.7019-7026.